DENSITY, MICROSTRUCTURE, AND STRAIN RATE-DEPENDANT BEHAVIOUR OF POLYMERIC FOAMS

by

Kapil Bharadwaj Bhagavathula

A thesis submitted in partial fulfillment of the requirements for the degree of

Doctor of Philosophy

Department of Mechanical Engineering
UNIVERSITY OF ALBERTA

Abstract

This thesis investigates the experimental mechanical behavior of polymeric foams, specifically studying the effects of microstructural features (pore size and wall thickness), foam density, and strain-rate-dependency on their stress-strain, lateral-axial strain, and failure. This thesis explores different polymeric foam materials that are used as liner materials in combat helmets, which are used in impact applications: 1. Polyurethane foams with varying densities from PORON, and 2. Advanced shear-thickening foam materials from D3O. Materials are primarily characterized before testing using scanning electron microscopy, and micro X-ray tomography to determine microstructural features (e.g., pore size). Experiments used to probe the mechanical response and failure behaviors include quasistatic testing, intermediate strain-rate experiments, and split-Hopkinson pressure bar dynamic testing. The deformation and failure behaviors are captured using ultra-high-speed imaging, which also allows for determination of 2D strain fields via multiple image-based techniques that are presented in the thesis (e.g., Digital Image Correlation). With these characterization and experimental measurements, contributions are made to phenomenological and scaling models, and mechanical response and damage evolution during rate dependent loading is demonstrated as a non-linear and non-monotonic behavior. The modelling provides a way to capture the combined effects of density, microstructure, and strain-rate. Long-term, we hope to bridge how new knowledge generated in the thesis on failure in foams can be leveraged to improve design and performance of polymer foams through partnership with end-users in the Canadian Department of National Defence and the US Army Research Laboratory.

Preface

I, Kapil Bharadwaj Bhagavathula, declare that this thesis titled, 'Density, Microstructure, and Strain Rate-Dependent Behaviour of Polymeric Foams' and the work presented in it are my own. Furthermore, permission is hereby granted to the University of Alberta Libraries to reproduce single copies of this thesis and to lend or sell such copies for private, scholarly or scientific research purposes only. Where the thesis is converted to, or otherwise made available in digital form, the University of Alberta will advise potential users of the thesis of these terms.

Chapter 2 of this thesis has been published as **Kapil Bharadwaj B**; Azar, A; Dennison, CR; Satapathy, S; Ouellet, S and Hogan, JD. *High Rate Compressive Behaviour of a Dilatant Polymeric Foam*, Journal of Dynamic Behavior of Materials (2018). I was responsible for conceiving the ideas and experimental design of the study; Performed experiments/data collection; Data analysis and interpretation; Primary author (drafted the manuscript); Azar, A; Dennison, CR; Satapathy, S; and Ouellet, S provided revisions to scientific content of manuscript; and Hogan, JD, my supervisor was the Principal investigator and provided revisions to scientific content, and stylistic/grammatical suggestions of manuscript.

Chapter 3 of this thesis has been published as **Kapil Bharadwaj B**; Parcon, JS; Azar, A; Dennison, CR; Satapathy, S; Ouellet, S and Hogan, JD. *Quasistatic response of a shear-thickening foam: Microstructure evolution and infrared thermography*, Journal of Cellular Plastics (2020). I was responsible for conceiving the ideas and experimental design of the study; Performed experiments/data collection; Data analysis and interpretation; Primary author (drafted the manuscript); Azar, A; Parcon, JS; Dennison, CR; Satapathy, S; and Ouellet, S provided revisions to scientific content of manuscript; and Hogan, JD, my supervisor was the Principal investigator and provided revisions to scientific content, and stylistic/grammatical suggestions of manuscript.

Chapter 4 of this thesis has been accepted to be published as **Kapil Bharadwaj B**; Meredith, C; Satapathy, S; Ouellet, S; Romanyk, D; and Hogan, JD. *Density, microstructure and strain-rate effects on response of polyurethane foams*, Experimental Mechanics (2021). I was responsible for conceiving the ideas and experimental design of the study; Performed experiments/data collection; Data analysis and interpretation; Primary author (drafted the manuscript); Meredith, C performed intermediate rate experiments, partially wrote the methods section, and provided revisions to scientific content of manuscript; Satapathy, S; Ouellet, S provided revisions to scientific content of

manuscript; Romanyk, D provided access to crucial research equipment, and revisions to scientific content of manuscript; and Hogan, JD, my supervisor was the Principal investigator and provided revisions to scientific content, and stylistic/grammatical suggestions of manuscript.

Chapter 5 of this thesis is under review as **Kapil Bharadwaj B**; Meredith, C; Satapathy, S; Ouellet, S; Romanyk, D; and Hogan, JD. *Phenomenological modelling of rate dependant compressive response of polyurethane foams*, International Journal of Impact Engineering (2021). I was responsible for conceiving the ideas and experimental design of the study; Performed experiments/data collection; Data analysis and interpretation; Primary author (drafted the manuscript); Meredith, C performed intermediate rate experiments, partially wrote the methods section, and provided revisions to scientific content of manuscript; Satapathy, S; Ouellet, S provided revisions to scientific content of manuscript; Romanyk, D provided access to crucial research equipment, and revisions to scientific content of manuscript; and Hogan, JD, my supervisor was the Principal investigator and provided revisions to scientific content, and stylistic/grammatical suggestions of manuscript.

Signed: Kapil Bharadwaj Bhagavathula

Date: 22 July 2021

"The important thing is to never stop questioning."

- Albert Einstein

Acknowledgements

With immense pleasure, I express my deepest and heartfelt gratitude to my supervisor Dr. James Hogan for his guidance and valuable support throughout the duration of my PhD work. I am indebted to him for providing the freedom and flexibility for carrying out my research work. His unflinching support during difficult phases will always remain a cradle of inspiration for me in my professional life. The chapters of life which I experienced while working with him will remain an indelible part of my life and will be assimilated in my personality.

I would like to thank Dr. Dan Romanyk, and Dr. Chris Dennison from the University of Alberta for their excellent discussions on material behaviour and supporting me to conduct experiments. Some of the experimental work in this thesis has been carried out at the Engineering workshop at the Department of Mechanical Engineering, University of Alberta, and the assistance of the laboratory staff is deeply acknowledged, and particularly I wish to thank Bernie Faulkner and Mitul Patel for their guidance.

In the preparation of the intermediate strain rate experimental data, Dr. Christopher Meredith from Army Research Laboratory, USA is highly appreciated. I thank him along with Dr. Sikhanda Sathapathy and Dr.Thomas Plaisted from Army Research Laboratory, USA, and Simon Ouellet from Defence Research Development Canada for the wonderful technical discussions over the course of multiple project collaborations.

I would take this chance to thank my colleagues at Mechanical Engineering department, Haoyang Li, Brendan Koch, Calvin Lo, Austin Azar, Kevin Adantya, and Chenwei Shao for sharing their knowledge and helping during my experimental work at the Center for Design of Advanced Materials (CDAM). I appreciate the countless discussions about various engineering problems and unrelated subjects. I would also like to thank undergraduate students from Mechanical Engineering department, James An, Kavya Weerasinghe, Kirsti Ann Bell, and John Samuel Parcon. I would also like to give a heartfelt, special thanks to team Parikshit, Manipal University who inspired me to pursue higher studies. I would also like to thank all the unnamed colleagues and friends in Edmonton for all their support. I wish all of you, the very best of luck for your future endeavours.

Finally, I would also like to give a special gratitude to my parents Padmavathi and Krishna Murthy for their unconditional love and constant moral support in all my endeavors, and my sister Samhitha for always standing by my side and believing her big brother. I consider myself the luckiest person to have such a supportive family, standing behind me with their love and support.

Kapil

Contents

List of Tables

List of Figures

Abbreviations

DIC	Digital image correlation
FPS	Frames per second
SEM	Scanning electron microscopy
SHPB	Split-Hopkinson pressure bar
XCT	X-Ray computed tomography
EDX	Energy-dispersive X-ray spectroscopy
ECDF	Empirical cumulative distribution function
FTIR	Fourier transform infrared spectroscopy
TBI	Traumatic brain injury
IR	Infrared
LD	Low density
MD	Medium density
HD	High density
PPE	Personal protection equipment

Symbols

t	Time	s
V	Volume	m^3
A_0	Specimen cross-sectional area	m^2
A_B	Transmitted bar area	m^2
ρ_f	Foam density	kg/m^3
ρ_b	Base polymer density	kg/m^3
ρ_r	Relative density	kg/m^3
ϕ	Porosity	m^3/m^3
E_f	Foam elastic modulus	MPa
E_b	Base polymer elastic modulus	MPa
E_0	Characteristic modulus	MPa
E_{Al}	Aluminum Young's modulus	MPa
σ	Stress	Pa
σ^*_{el}	Elastic collapse stress	Pa
σ^*_{pl}	Plastic collapse stress	Pa
ϵ	Strain	m^3/m^3
ϵ_{xx}	Lateral strain	m^3/m^3
ϵ_{yy}	Axial strain	m^3/m^3
$\dot{\epsilon}$	Strain rate	s^{-1}
$\dot{\epsilon_0}$	Reference strain rate	s^{-1}
D_i	Pore size	μm
T_i	Wall thickness	μm

Chapter 1

Introduction

1.1 Motivation

The ability to absorb energy using polymeric foam materials is an aspect that has a varied range of engineering applications such as in automotive [1, 2], aerospace [1–3], military [3, 4], packaging [5], and as thermal-acoustic insulating materials [6]. Polymeric foams have low densities ($< 400\ kg/m^3$) and their energy absorbing capabilities are used to mitigate energy transfer between objects during impact events [7–9]. These energy absorbing properties make them an ideal choice for usage as protection materials, such as in personal protection equipment (PPE) like helmet liner materials [4, 7], knee pads [7], and as structural materials in shock mitigating applications [6]. The main function of the foam material in protection applications, such as inner liners in combat helmets and comfort layers in body armor, is to absorb part of the impact/ballistic energy and to reduce the amount of load transmitted to the human body.

To make efforts toward improving foams used in helmet liners, there exist a number of studies on compressive [7, 10, 11], tensile [11, 12], and shear [12] behavior of polymeric foams. In impact applications, the polymeric foams are often subjected to severe loading conditions involving time-varying stress states [7–9] and strain rates [7, 10, 13, 14]. In addition, the varied range of microstructural features of polymeric foams (pore size, pore shape, wall thickness) also contribute to its behavior in impact applications [15]. Accordingly, numerous parameters influencing the mechanical response have been identified and studied by previous researchers for polymeric foams, such as cell structure (open or closed cells) [7, 10], loading stress states [7–12, 16] and strain rates [7, 9, 10, 14], foam density [10, 17], microstructural features [3, 7, 10, 18, 19], solid polymer content [4, 12, 20, 21], and foam type (e.g., polyurethane (PU) [15, 22, 23], polystyrene (PS) [7, 18, 23, 24],

and polyethylene (PE) foams)[15, 23]. More recently, a new type of foam called 'dilatant' or 'shear-thickening' polymeric foam is being introduced, which behave like a rigid material when subjected to high stress and deformation rates [25–27]. In some cases, these types of foams are being sold commercially as a replacement for conventional foams in, for example, helmet liners, despite limited available published data on their overall performance. Many of these aspects on the mechanical response of polymeric foams are explored in this thesis.

1.2 Background and Literature Review

1.2.1 Polymeric Foam Mechanics

Compressive stress-strain responses of foams show three fundamental modes of deformation. This thesis focuses mainly on uniaxial compressive behavior and thus is discussed in further depth here, and it is to be noted that the mechanical behaviour of foams in tension manifest differently as discussed in Chapter 3. Figure 1.1 shows the fundamental modes of deformation for foams in compression, as characterized by the stress-strain response. The first deformation mode is defined as *linear elasticity* where deformation is controlled by pore wall bending in open-cell foams [23] and, in the case of closed celled foams, by stretching of the pore walls [28]. The elastic modulus E is measured as the slope of the *linear elastic region* of stress-strain response. In this region, the compressive stress is directly proportional to strain and deformation is recoverable. The next mode of deformation is the *plateau* which is associated with collapse of the cells. The plateau region is determined by elastic buckling of the cell walls and the stress is near constant or increases slowly with respect to strain. This stress level is referenced to as the elastic collapse (or) pore collapse stress. The third and final mode of deformation is referred to as *densification*. Here, the cells start to completely collapse, opposing pore walls touch and further strain crushes out the porosity and the material starts to behave like the solid itself, giving the region of rapidly increasing stress.

1.2.2 Polymeric Foam Chemistry and Manufacturing

Polymeric foam manufacturing generally consists a minimum of two phases, a solid polymer matrix (base material) and a gaseous phase (blowing agent) that is dispersed in the matrix [29]. Other solid phases may also be present in the matrix in the form of additive particles [30]. Different types of polymeric foams may be manufactured such as expanded rubbers, cellular elastomers, and sponges. These foams can be either thermoplastics or thermosets. A thermoplastic is a polymer material that becomes moldable at

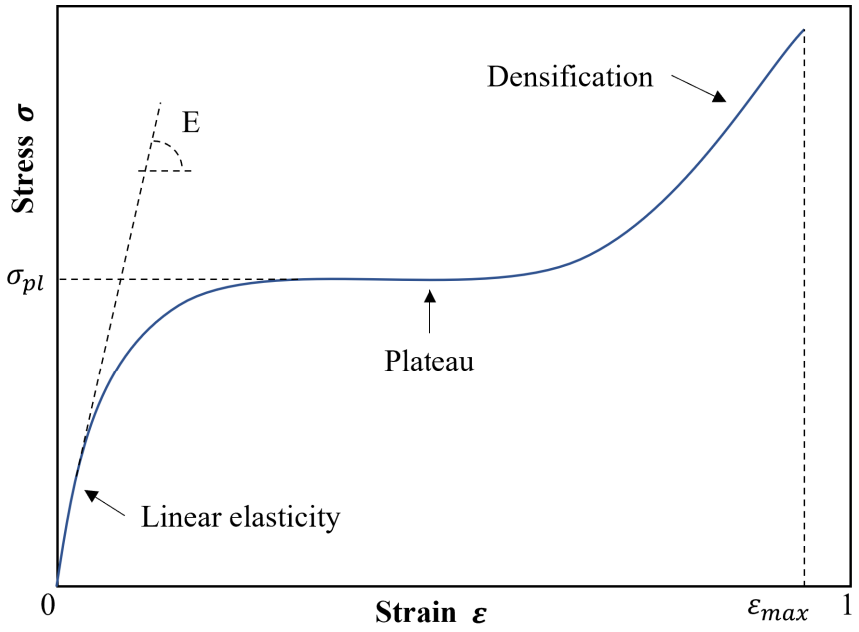

FIGURE 1.1: Fundamental characteristic compressive stress-strain curve for flexible polyurethane-based polymeric foam materials.

a certain elevated temperature called the glass transition temperature (T_g) and solidifies upon cooling. The glass transition temperature is the temperature at which gradual and reversible transition in amorphous materials from a relatively brittle "glassy" state into a viscous or rubbery state occurs [31]. The glass transition temperature is slightly higher than the melting temperature, which is the temperature at which thermoplastic polymers can be moulded. Thermoset materials generally exist in liquid form and are cured through a chemical reaction into a permanent solid.

Various methods of foam manufacturing can be adopted and desirable properties can be achieved for the foam to suit different applications. Typical processing methods include mechanical foaming processes like foam extrusion molding, foam injection molding, spraying, lamination, precipitation, rotational casting, composites, and frothing [32]. The polymeric foams may be manufactured in any shape or form such as boards, blocks, sheets, slabs, tubing, molded shapes, etc. This thesis focuses on foams derived from polyurethanes. Polyurethanes are a type of polymer that contain a urethane linkage(-NH-CO-O-). Polyurethanes are manufactured by reacting isocyanates with compounds that have atleast two active hydrogen atoms, such as polyols, that contain hydroxyl-groups, in the presence of a catalyst [33]. There exist many compounds that contain active hydrogens and therefore, the number of polyurethanes that can be synthesized is large.

The molecular weight (MW) of the polyols used in polyurethane synthesis varies between

300 - 10000 daltons, in the region of low MW polymers called oligomers, and the number of hydroxyl (-OH) groups/molecule of oligo-polyol in the range of 2-8 OH groups/mol [29, 33]. A polyol of high MW of 2000-10000 daltons with a low functionality with 2-3 hydroxyl groups/mol synthesises an elastic polyurethane structure, whereas a low MW oligo-polyol of around 300-1000 daltons, with a high functionality of around 3-8 hydroxyl groups/mol leads to a rigid crosslinked polyurethane [33]. The specific properties of the polyurethane can be tailored to a specific need by combining the appropriate compounds.

1.2.3 Shear Thickening Foams

An advanced technology based on shear thickening fluids was invented in 1999 by the British engineer Richard Palmer and is commercialized by the Company D3O [34]. It includes a foam with an elastomeric polyurethane matrix in which a borated silicone shear thickening fluid is distributed. The resulting foam material is flexible when strained at quasistatic strain rate but hardens under dynamic strain rates [35]. In this material, the apparent shear viscosity of the borated silicone shear thickening fluid (non-Newtonian fluid) increases with increasing shear rate. The shear-thickening viscosity is attributed to polymer viscoelasticity. One way to produce a shear thickening fluid is to disperse very small particles (e.g. SiO_2 nanoparticles) into a base polymer liquid like silicone or polyethylene glycol. During mechanical loading, the polymer molecular structure repeatedly stretches and recoils to adjust to the flow field. If the flow velocity of the polymer molecules is too high, they do not have sufficient time to relax and adjust to the flow, and the resultant excessive elastic strain leads to a high apparent viscosity in the material, represented as shear-thickening behavior. This unique feature of the shear thickening fluid-based technology has been leveraged to develop PPE equipment such as helmet liner pads, and limb protector pads.

1.3 Thesis Objectives

The objective of this thesis is to develop a better understanding of the mechanical behavior of polymeric foam materials utilizing experimental mechanics approaches. Long-term, we hope to bridge how this understanding can be leveraged to improve design and performance of polymer foams through partnership with end-users in the Canadian Department of National Defence and the US Army. This better understanding is achieved through mechanical testing and microstructure characterization of polymeric foams, specifically studying the effects of microstructural features (pore size and wall thickness), foam density, and strain-rate-dependency on the mechanical response of polymeric foams, manifested as stress-strain, lateral-axial strain, and failure responses. Strain measurements

in these experiments are obtained using ultra-high-speed video images and associated analysis techniques (e.g., Digital image correlation, image processing), which are used to measure both axial and lateral strains under large deformations. These strain measurements are then used for model development and validation. The results from testing and characterization techniques are used to inform two types of models to predict material behavior - a simple phenomenological model, and a scaling model. Such material models often require a number of material constants to describe a process of physical phenomena that include complicated deformation mechanisms [36–39]. In this thesis, material parameter estimation for model development is informed by uniaxial compression experiments at various strain rates, and for different foam types and densities.

This thesis specifically looks at the behavior of two commercially available polymeric foams used in protection applications:

1. A polyurethane-based, open-cell elastomeric foam that is available in three different relative densities obtained from Poron XRD considered as a baseline material for this thesis.
2. An advanced semi open/closed-cell shear-thickening foam manufactured by D3O. The variants under investigation are D3O LITE D and D3O Liner, which are advertised as non-Newtonian shear-thickening foam materials.

1.4 Thesis Goals

The objectives of this thesis are accomplished by completing the following research goals:

- Obtain the critical microstructure parameters of both the baseline material and the advanced shear-thickening foam (e.g., pore size, pore shape, and wall thickness) via scanning electron microscopy (SEM) and micro-computed X-Ray tomography techniques (XCT). These parameters are considered as inputs to models and for comparing across other materials.
- Establish experimental mechanics approaches to study polymeric foam behaviour, including:
    1. Use of an ultra-high speed camera coupled with a modified version of the split-Hopkinson pressure bar apparatus for dynamic compression of polymeric foam materials for deformation visualization and strain measurements.

2. Digital Image Correlation for measuring deformation and strain during uniaxial quasistatic compression and tension (using Instron E3000 machine), intermediate strain rate compression (using Drop tower apparatus), and dynamic compression (using a modified version of the split Hopkinson pressure bar apparatus) loading conditions. These results are used as inputs in terms of stress-strain curves and deformation evolution in the models proposed in this thesis.

- Material characterization of pristine samples to inform on chemical constituents using Fourier transform infrared spectroscopy (FTIR) and Energy-dispersive X-ray spectroscopy (EDX).

- Infrared imaging to inform the thermo-mechanical response of the foam materials subject to uniaxial compression and tension. All measured foam properties are compared between the different foam materials for better understanding.

- Develop phenomenological relationships between material parameters such as density, relative density, porosity, elastic modulus, collapse stress and energy absorption, and extending existing phenomenological relationships to predict mechanical strength parameters.

- Implement a microstructure and strain-rate-dependent phenomenological model for predicting the stress-strain responses of porous polymeric foams under quasistatic, intermediate, and dynamic uniaxial compression loading.

1.5 Key Contributions

The outcomes of this thesis will be important to:

i. Offer propitious avenues for qualitative and quantitative understanding of mechanical behavior of porous polymeric foams, and serving as a foundation for further material design and optimization.

ii. Provide insights into the factors that influence the behavior of polymeric foams under strain rate dependent loading by connecting failure mechanisms to the microstructural features.

iii. Development and validation of phenomenological and scaling law models describing the density, microstructure and strain-rate effects in porous polymeric foam materials.

iv. Provide an understanding on the behavior of shear-thickening foam materials by studying mechanical response, accomplished through experimentation and material characterization. In addition, different experiments are performed as a part of the thesis, where there is lack of experimental data in the literature. These techniques include intermediate strain-rate compression experiment and Infrared thermography approaches. Together, the use of multiple material and mechanical characterization techniques allows for the shear-thickening phenomenon to be better understood.

v. The models, experimental data, and microstructural information, can be used as to guide design and manufacturing by end-users. This is outside of the scope of work in this thesis, but could be pursued by others, including partners.

1.6 Thesis Structure

This thesis is structured based off of research published as journal articles presented as individual chapters. Individual author contributions are listed on the title pages of chapters $2-5$. Variable notations may differ across chapters. The chapters are presented in the following order:

- Chapter 1: "Introduction". Discusses the background and motivation for study of polymeric foams, sets out the objectives of the thesis, and outlines the overall contributions to the field done by the thesis.

- Chapter 2: "High rate compressive behaviour of a dilatant polymeric foam". Published in the *Journal of Dynamic Behavior of Materials*, as **Kapil Bharadwaj Bhagavathula**, Austin Azar, Simon Ouellet, Sikhanda Satapathy, Christopher R Dennison, and James David Hogan, 2018. In this chapter, the strain-rate dependent behavior of a dilatant polymeric foam is studied, focusing on developing characterization and testing methodologies needed to better understand the links between microstructure and failure. These links are studied for a commercially-available shear-thickening foam, named D3O LITE D. Prior to testing, the pore sizes ($82 \pm 26\mu m$), ligament thickness between pores ($5 - 12\ \mu m$), and porosity ($83 \pm 5\%$) were quantified using Scanning Electron Microscope images. Samples were then tested in compression under quasi-static conditions for a strain rate of $0.04\ s^{-1}$ using an MTS testing apparatus, and in dynamic conditions using a split Hopkinson pressure bar apparatus for strain rates of 5280 to 5720 s^{-1}. For both rates, strains upwards of 85% were achieved and this allowed us to examine a variety of material failure behaviors, including elastic collapse, localization, pore

collapse, densification and post pore collapse hardening. In this material, the elastic collapse stress for quasi-static and dynamic compression conditions was found to be 120 ± 40 kPa and 243 ± 47 kPa, respectively, and elastic modulus were noted of 2.4 ± 0.7 MPa and 3.8 ± 1.2 MPa, respectively. Following the elastic collapse, some unique specimen-scale localization features were observed during the dynamic experiments. These features are unique to dynamic compression and were not observed for the quasi-static case, demonstrating a distinct high-rate behavior for this material, possibly linked to its "shear thickening" label. After densification, complete pore collapse followed by post pore collapse hardening were observed for both strain rates. These results represent some of the first studies on shear-thickening foams in the literature, and the testing methodologies developed in this study serve as the foundation for additional experimental studies across a broader range of foam materials.

- Chapter 3: "Quasistatic response of a shear-thickening foam: Microstructure evolution and Infrared thermography". Published in the *Journal of Cellular Plastics*, as **Kapil Bharadwaj Bhagavathula**, John Samuel Parcon, Austin Azar, Simon Ouellet, Sikhanda Satapathy, Christopher R Dennison, and James David Hogan, 2020. In this chapter, the thermo-mechanical response of a dilatant polymeric foam in quasistatic tension and compression is studied, focusing on the links between microstructure, mechanical response, and associated temperature rises in these materials during loading and failure. These links are studied for a commercially-available shear-thickening foam, named D3O LITE D. Samples were tested under quasi-static conditions for a strain rate of $0.1s^{-1}$ in tension and compression. Micro X-ray computed tomography (XCT) was used to study the evolution of microstructure (pore size and wall thickness) as a function of strain and this was achieved by developing MATLAB-based programs to analyze these microstructural features. The foam specimens were loaded until failure which allowed for the investigation of the elastic, inelastic, and failure regimes. From the XCT images, pore stretching and cell wall tearing are observed in tension, and buckling and pore collapse are observed in compression. These mechanisms are observed in-situ using an infrared thermal camera that recorded temperature profiles during testing, and these temperature measurements are linked back to stress-strain, and temperature-strain responses. For this material, the tensile yield stress was 0.57 ± 0.1 MPa and the elastic modulus was 5.47 ± 0.1 MPa respectively, at a yield strain of 0.1 ± 0.04. At the time of failure, the average temperature of the specimen was found to increase by $\sim 3\,^{\circ}\mathrm{C}$ and a local temperature increase of $\sim 8\,^{\circ}\mathrm{C}$ was observed in the failure region. In compression, the elastic collapse stress and elastic modulus were found to be 0.130 ± 0.016 MPa and 2.5 ± 0.2 MPa, respectively. The temperature

increase in compression at ~ 0.83 strain was $\sim 0.65\,^{\circ}\mathrm{C}$. These results represent some of the first mechanical properties on shear-thickening foams in the literature, and the discoveries on the linkages between the microstructure and the mechanical properties in this study are important for researchers in materials design and modelling.

- Chapter 4: "Density, microstructure and strain-rate effects on the compressive response of polyurethane foams". Accepted to be published in *Experimental Mechanics*, **Kapil Bharadwaj Bhagavathula**, Christopher Meredith, Simon Ouellet, Dan L Romanyk, and James David Hogan, 2020. In this chapter, polyurethane foams of three different densities (195 kg/m^3, 244kg/m^3, and 405 kg/m^3) obtained from PORON are examined under compression loading at quasistatic, intermediate and dynamic strain rates. Micro X-ray computed tomography is used to characterize the pristine microstructure (pore size and wall thickness). Quasistatic compression are performed using an Instron E3000 machine at strain rates of 0.001 to 0.1 s^{-1}, and intermediate strain rate compression tests at $1 - 100\ s^{-1}$ are performed using a high speed MTS machine. Dynamic compression tests are performed using a split−Hopkinson pressure bar apparatus with aluminum bars at a strain rate of $4500 \pm 1000\ s^{-1}$. The compression tests are coupled with high speed cameras to calculate strain using digital image correlation, and to visualize deformation. The elastic modulus and collapse stress are found to be dependent on foam density, microstructure, and strain rate. Phenomenological relationships between the elastic modulus, collapse stress, strain rate, and foam density are established, and the implications for material behavior are discussed. The analytical equations developed in this study serve as a good starting point for impactful modeling of such materials [17, 40] that predict the effect of microstructure, density, and stress states on the mechanical response of polymeric foams.

- Chapter 5: "Density, strain rate and strain effects on mechanical property evolution in polymeric foams". Submitted to *International journal of Impact Engineering* as **Kapil Bharadwaj Bhagavathula**, Christopher Meredith, Simon Ouellet, Dan L Romanyk, and James David Hogan, 2021. In this chapter, a comprehensive experimental study of the variation in Poisson's ratio and Tangent modulus of polymeric foams during rate dependant uniaxial compression is presented. Here, polyurethane foams of three different densities (195 kg/m^3, 244 kg/m^3, 405 kg/m^3) obtained from PORON were examined under uniaxial compression loading at strain rates ranging from 0.001 s^1 to 5000 s^1. All compression experiments were coupled with a high-speed camera to enable Digital Image Correlation to measure and visualize deformation strains. These measurements enable us to study deformation evolution characteristics (e.g., Tangent modulus and Poisson's ratio) and provide

qualitative description of deformation and failure in these materials. A non-linear evolution of Poisson's ratio is observed in-situ in these materials. The compressive response is predicted through least square fitting using the Avalle model [20], and model coefficients are found to scale according to a power-law across all strain rates studied here. The Tangent modulus and Poisson's ratio, along with the stress-strain curves and scaling coefficients are compared with microstructural parameters of interest such as pore size and wall thickness to inform on deformation mechanisms in the material.

- Chapter 6: "Comparison between D3O and PORON polyurethane foams as prospective helmet liner materials". In this final chapter, results and observations are linked across each of the polymeric foam materials studied in this thesis. Here, the focus is on comparing pore structures (e.g., size, wall thickness), chemical characterizations, strain-rate dependent stress-strain responses, deformation behaviors, and some key scalar mechanical properties (e.g., Modulus and collapse stress). These enable us to gain insights into the effects of microstructural features (e.g., pore size and wall thickness), foam density, and strain rate on the mechanical response of polymeric foams. Altogether, results in this thesis demonstrate that not all polymeric foam materials follow ordered trends and can be described by the same model forms, and these are a consequence of their pore morphology, density, base mechanical properties, and strain rate-dependencies of these characteristics.

- Chapter 7: "Conclusion" summarizes the key scientific contributions and implications of this research. This chapter also highlights the list of all academic publications resulting from this thesis and outlines directions for future work.

Chapter 2

High rate compressive behaviour of a dilatant polymeric foam

Published as **Kapil Bharadwaj B**; Azar, A; Dennison, CR; Satapathy, S; Ouellet, S and Hogan, JD. *High Rate Compressive Behaviour of a Dilatant Polymeric Foam*, Journal of Dynamic Behavior of Materials. (2018)

Author	**Contributions**
Kapil Bharadwaj B	Conceived the ideas and experimental design of the study; Performed experiments/data collection; Data analysis and interpretation; Primary author (drafted the manuscript)
Azar, A	Provided revisions to scientific content of manuscript
Dennison, CR	Provided revisions to scientific content of manuscript
Satapathy, S	Provided revisions to scientific content of manuscript
Ouellet, S	Provided revisions to scientific content of manuscript
Hogan, JD	Provided revisions to scientific content of manuscript; Provided stylistic/grammatical revisions to manuscript; Principal investigator

2.1 Abstract

Polymeric foams are an essential part of personal protection equipment, such as helmets and body armor. In this work, the strain-rate dependent behavior of a dilatant polymeric foam is studied, focusing on developing characterization and testing methodologies needed to better understand the links between microstructure and failure in these materials. These links are studied for a commercially-available shear-thickening foam, named D3O LITE D. Prior to testing, the pore sizes ($82 \pm 26\mu m$), ligament thickness between

pores ($5 - 12\mu m$), and porosity ($83 \pm 5\%$) were quantified using Scanning Electron Microscope images. Samples were then tested in compression under quasi-static conditions for a strain rate of $0.04s^{-1}$ using an MTS testing apparatus, and in dynamic conditions using a split Hopkinson pressure bar apparatus for strain rates of 5280 to $5720s^{-1}$. For both rates, strains upwards of 85% were achieved and this allowed us to examine a variety of material failure behaviors, including elastic collapse, localization, pore collapse, densification and post pore collapse hardening. These mechanisms are observed in-situ during compression experiments using high-speed photography, and linked back to stress-strain responses of the materials. In this material, the elastic collapse stress for quasi-static and dynamic compression conditions was found to be 120 ± 40 kPa and 243 ± 47 kPa, respectively, and elastic modulus were noted of 2.4 ± 0.7 MPa and 3.8 ± 1.2 MPa, respectively. Following the elastic collapse, some unique specimen-scale localization features were observed during the dynamic experiments. These features are unique to dynamic compression and were not observed for the quasi-static case, demonstrating a distinct high-rate behavior for this material, possibly linked to its "shear thickening" label. After densification, complete pore collapse followed by post pore collapse hardening were observed for both strain rates. These results represent some of the first studies on shear-thickening foams in the literature, and the testing methodologies developed in this study will serve as the foundation for additional experimental and computation studies across a broader range of foam materials.

2.2 Introduction

The ability to dissipate energy using foams is an aspect that has many engineering opportunities in dynamic applications, such as Automotive Industry [41], core materials in composite sandwich constructions [42], and Personal Protective Equipment [43–45]. Typical foam materials used in these energy-absorbing applications include Expanded Polystyrene (EPS) [17, 22, 46], Expanded Polypropylene (EPP) [7, 22], and Thermal Polyurethanes (TPU) [43, 47]. These studies have focused on better understanding the effect of microstructure [7, 10, 47], density [7, 10, 22] and strain-rate [7, 10, 46, 48, 49] in tension [50] and compression [17, 41, 49–54], as well as during impact experiments using drop testing [19] and gas-gun approaches [41]. In this paper, the authors investigate the rate-dependent compressive stress-strain response and failure of a polymeric foam, and so focus on presenting the limited literature in this area (specifically for the dynamic regime). Split Hopkinson pressure bar (SHPB) is a widely recognized experimental technique used to investigate the strain-rate dependent response and stress-strain curves for a variety of soft engineering materials at high strain rates from $10^2 - 10^5 s^1$ [10, 42, 49, 51, 55, 56]. For example, Saha et al. [10] have shown that different grades of

rigid polyurethane (PUR) foams and cross-linked polyvinyl chloride (PVC) foams exhibit some form of strain rate dependency. At quasi-static strain rates, both PUR and PVC foams show an increase of 15% in yield and peak stresses with every increase in one order of magnitude of the strain rates from $0.001s^{-1}$ to $0.1s^{-1}$. At strain rates above $700s^{-1}$, they observed a two-fold increase in the yield strengths, which were twice as much when compared to the quasi-static regime. They also observed that yield strengths remained constant with increasing strain rates up to $1700s^{-1}$ and the only changes observed in the compressive response are at the peak stresses. Similarly, Ouellet et al. [49] performed studies at strain rates from $0.008s^{-1}$ to $2700s^{-1}$ and found that polystyrene foams exhibited noticeable strain rate dependency in stresses only at rates greater than $100s^{-1}$. Their paper also looked at polyethylene foams and found that these also exhibit rate dependency, but only at strains greater than 20%. In another paper, Song et al. [46] studied a different grade of polystyrene foam than Ouellet et al. [49] and found an increase of 10% in collapse stress with every increase in the order of magnitude of the strain rates from $0.001s^{-1}$ to $950s^{-1}$.

In many of these papers and other studies, the authors point to the importance of microstructure (usually in terms of density [7, 10, 18] and cell sizes [7, 10, 46]) and failure (usually through a post-test macroscopic assessment of the sample [1, 22]) on the strain-rate dependent behavior of polymeric foams. For example, Di Landro et al. [17] and Santa Maria et al. [52] suggested smaller cell sizes results in increased strength compared to larger cell sizes. They also noted an increase in the amount of energy that was absorbed (through measure of strain energy) at higher strain rates for smaller cell sizes and, consequently, higher relative densities [7, 10, 17]. In addition to increases in strength and energy absorption behaviors for smaller cell sizes, Bouix et al. [7] found that smaller cell sizes resulted in less sensitivity to increasing strain rate when compared with larger cell sizes. The importance of cell sizes on the rate dependent behavior of polymeric foams is coupled to onset and evolution of failure processes in these materials, and how these processes compete at different strain rates (e.g., work by Saha et al. [10]). Several failure mechanisms that have been studied for polymeric forms are the inertia [1], stretching and buckling of the cell walls [17], and the effects of trapped gases [7, 17]. Understanding these relationships between failure mechanisms, microstructure, and the strain-rate dependency of polymeric foams is important in order to develop improved materials in the future; this is what the authors begin to do in this paper.

Building upon these past works investigating effects of microstructure and failure on the strain-rate dependent behavior of polymeric foams, this paper investigates the high strain-rate deformation of dilatant foams that is advertised as “shear-thickening”. This material is employed in both industrial and military applications where energy absorption

qualities are desired. In this paper, the authors focus on characterizing the microstructure in terms of pore size and wall thickness and study compressive behavior of this shear-thickening foam for different strain rates. As limited work has been done in the published literature on shear thickening foam materials, this study intends to begin to establish an understanding of mechanical properties and dynamic behavior, accomplished through experimentation and characterization. The paper is comprised of the following sections: first, microstructure characterization techniques and sample preparation methods are established and described. Second, testing methods are presented, followed by the presentation of the experimental results. These results are supported by stress-strain curves and video images obtained from high-speed cameras. Finally, implications and contributions of this work are highlighted, and future directions are suggested.

2.3 Materials and Characterization

2.3.1 Material and Sample Preparation

The material investigated in this work is a semi-open/closed-cell polymer-based foam that was manufactured by D3O®. The variant under investigation is 'D3O®LITE D', which is advertised as a non-Newtonian shear-thickening material. To ensure consistency across strain-rates, a single sample size was used for both quasi-static and dynamic experiments. Common sample preparation techniques [41, 49] like the use of a hollow punch were initially adopted in this study. Other techniques for sample preparation were also pursued, including water-jet cutting and solid metal punch, but it was found that hollow punch technique results in the least amount of damage to the outer surface of the specimens. Using a special metallic hollow punch, disk samples of diameter $8 \pm 0.3mm$ were cut from an as-received sheet of uniform thickness of 4mm, with the axis of the disk oriented along the through-thickness direction of the as-received sheet of foam. Care was taken to ensure that the samples' end surfaces were parallel, and that minimum damage is induced to the edges during sample preparation. The choice of these sample size and shape resulted in constant strain-rate deformation and the best force equilibrium for the dynamic experiments, which are two criteria that are noted to be important and challenging when testing soft materials [56–59] (results presented later in Figure 6 and 8).

The physical and mechanical properties provided by the manufacturer are listed in Table 2.1 [60]. The authors note that differences in the compressive strength between this study and those provided by the manufacturer is expected because the specimen sizes used in the ASTM D3575-14D is $25.4mm$ x $25.4mm$ x $25.4mm$, whereas the test specimen in

TABLE 2.1: Manufacturer's listed properties for D3O LITE D

	D3O Lite D	**Test Method**
Density Range	200 - 220 Kg/m^3	ISO 845: 2009
Hardness	60 Asker C	DTS004
Tensile Strength	2.2 MPa	ISO 1798: 2008
Split Tear Strength	2.9 N/mm	SATRA TM65
Compressive Strength	190 kPa	ASTM D3575-14D
Flexural Modulus	5.59 MPa	DTS052
Water Absorbency	1 %	ISO 62 : method 1

our study is $8mm$ in diameter and $4mm$ in thickness (which is governed by the thickness of the as-received foam sheet). The sensitivity of material strengths to geometry and specimen-size effects are documented in the literature [7, 41], including experiences by other authors, and the authors expect that to manifest in differences in their strengths and those provided by the manufacture. Note, potential differences in composition, pore sizes and wall thicknesses may also occur as a consequence of different as-received sheet sizes.

2.3.2 Microstructure Characterization

For 2-D microstructure characterization, a Hitachi S-4800 field emission scanning electron microscope (SEM) was used. Figure 2.1 (a) shows an SEM image of D3O® LITE D at 100x magnification. From this cross-sectional view, the pores appear to be fairly circular and it is observed that the microstructure is mostly dominated by closed cells with small regions of semi-open cell features. These semi-open cells are noted with red circles in Figure 2.1 (a), while the closed cells are more obvious. The concentrated bright features that appear near the cell wall boundaries, which lay inside the pore structures, are believed to be either small chunks of unexpanded polymer that remain intact during the cooling stage of manufacture process, or some form of additives that may have been introduced during the foaming process. Pore sizes were measured using ImageJ across the 10 SEM images (728 total pores), and were found to range between 50 and 200m with an average pore size of $82 \pm 26\mu m$. Image processing techniques developed by Hogan et al. [61] were used to compute the area fraction of the pores as a measure of porosity. The average porosity of the material was found to be $83 \pm 5\%$ across the 10 images that were used this computation.

Next, shown in Figure 2.1 (b) is an SEM micrograph of the material taken at a higher magnification of 600x. Using ImageJ, the wall thickness are computed across 10 images across the cross-section and wall thickness is estimated by measuring minimum thicknesses of the walls between adjacent pores. The average wall thickness across 10 images

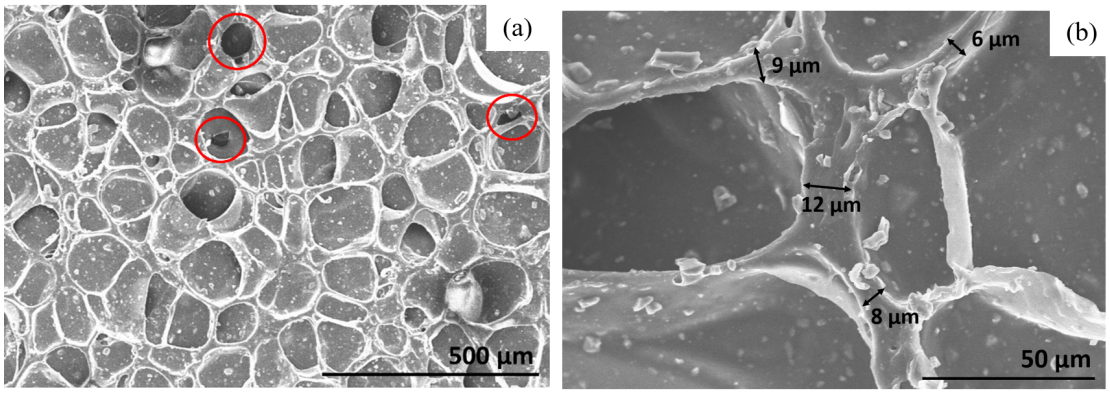

FIGURE 2.1: (a) Scanning Electron Microscope (SEM) Micrograph of D3O LITE D at 100 x magnification showing microstructure dominated by fairly circular pores of varying sizes with rare instances of semi-open pores represented by red circles. (b) SEM Micrograph at 600 x magnification showing sample wall thickness measurements. The bright features that are prominently visible in this cross-section are a result of additives/unexpanded bulk polymer. The length scales are denoted on the bottom-right corner.

(750 total measurements) is calculated to be $8.3 \pm 4.5 \mu m$, with wall thicknesses ranging between 5 and $12 \mu m$. Measurements of pore size and wall thickness are used later when describing the effect of microstructure on the rate-dependent failure this foam.

2.4 Experimental Methods

2.4.1 Quasi-static Compression

The specimens were tested at a quasi-static strain rate of $0.04 s^{-1}$ using a Material Test System (MTS) – 810 machine, a schematic of which is shown in Figure 2. This assembly included visualization capabilities with a AOS PROMON U750 – high-speed camera, which enabled us to observe macroscopic deformation features during testing. This camera has a resolution of 1280 x 1024 pixels and recorded at a framerate of 24 Frames per second (FPS), which coincided with the data acquisition rate of the MTS machine. Both camera and MTS were triggered manually at the same time, and the synchronization was verified through comparison between when the piston displacement was first observed in the camera images with the displacement data recorded by the MTS machine (no adjustments were necessary). To perform the test, the specimen is placed between a compressive grip of the MTS that consists of two $25.4 mm$ diameter steel bars (Figure **??**). These are guided and held with precise alignment. A cylindrical piston, moving at a constant displacement rate is used to compress the samples. A $10 kN$ load cell with a background noise corresponding to approximately $\pm 1 N$ recorded the time

histories of the forces, and the displacement of the piston was measured to an accuracy of $0.001mm$ using linear variable differential transformer (LVDT) displacement sensor. The actuator speed was set to $1mm/min$, corresponding to a nominal strain rate of $0.04s^{-1}$ in the sample. Since almost no data regarding material densification was available before experimentation, the tests were terminated based on two conditions: first, when near-complete densification was observed in the force-displacement curve during loading, and second, when the actuator speed was no longer constant. Strains exceeding 90% were achieved in all the quasi-static trials. The engineering stresses are calculated by dividing the applied load by the original specimen surface area, and the engineering strains are computed by dividing the specimen displacement by the original specimen height. Three trials with same loading conditions were performed to verify repeatability of the material behavior.

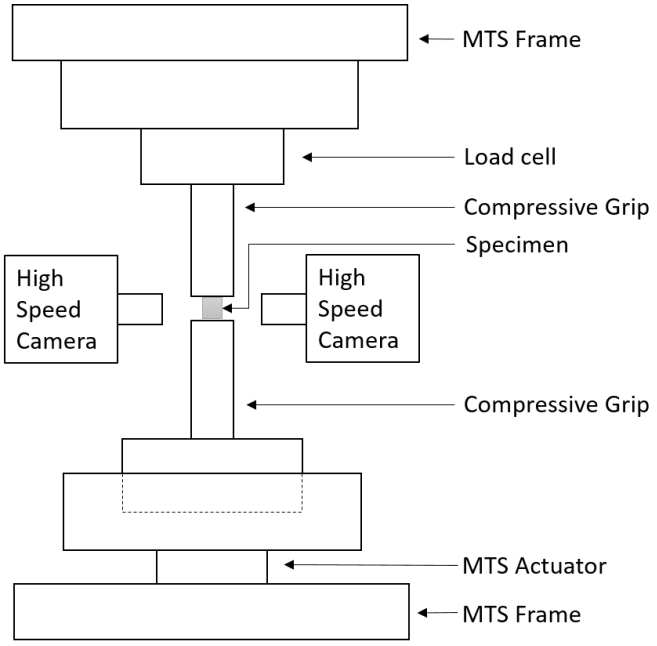

FIGURE 2.2: Schematic diagram of the MTS experimental setup combined with two high-speed cameras perpendicular to each other facing the sample to aid in Poisson's ratio measurement.

2.4.2 High Strain-rate Compression

The dynamic compression experiments were performed using a modified version of a split Hopkinson pressure bar (SHPB) apparatus [62], shown in Figure 3. The setup consists of a gas gun, a striker bar, an incident bar, a transmission bar, sensors, a data acquisition system, and an ultra high-speed camera. In this study, the bars were made of solid aluminium with a density of $2700kg/m^3$ and stiffness of $68.9GPa$, which were procured from McMaster-Carr. Polymeric bars have also been used in past studies in the

literature to study foams [63, 64], but are recognizably more challenging to manufacture. The use of aluminium pressure bars for testing soft materials has been well documented in literature [50, 53], and the authors have chosen to use them in their setup because they are more easily available and less expensive. In the dynamic tests, the polymeric foam sample is sandwiched between the incident and transmission bars, and the sample end faces were lubricated with high-pressure grease so as to reduce frictional effects and to allow for easy radial expansion during compression. This setup is consistent with others in the literature [41, 50, 63, 65].

In a SHPB experiment, a striker bar is launched from a pressurised gas gun and strikes the incident bar generating an elastic stress wave that travels through the incident bar to the sample, dynamically loading it. Due to mismatch of mechanical impedances of aluminium and the foam sample, reflected and transmitted waves are generated at the left and the right interfaces of the sample, respectively. The transmitted wave travels through the sample into the transmission bar. The incident and reflected signals are recorded by a strain gage mounted on the incident bar and the transmitted signal is captured by a strain gage mounted on the transmission bar. The strain gages used in the setup in this study are $350\Omega \pm 0.3\%$ with a gage factor of $2.130 \pm 0.5\%$ (Micro Measurements CEA-13-250UN-350 semiconductor strain gages). The gages are connected to their individual conditional amplifiers (Vishay InterTechnology 2310B) and a gain of 100 to 1000 is applied on the transmission gage because of the small magnitudes of transmitted stresses. The output from the conditional amplifier is fed to a Tektronix DPO2024B oscilloscope with 12-bit resolution recording at $500MHz$. Careful observation of transmitted gage raw voltage data in these experiments revealed a background noise approximately equal to ± 1 micro strain, which corresponds to 20% of the measured strain at the onset of yielding (~ 5 micro strain). The challenges of developing SHPB systems to measure the dynamic response of foams is widely documented [46, 49, 66, 67], and the approaches that the authors pursued are consistent with those in the literature. The lengths of projectile, incident bar and transmission bars are 500, 1000 and 910 mm respectively with a diameter of 12.7 mm. The length of the bars and the relative positioning of strain gages avoid overlapping of stress waves [55], also ensuring that longer loading durations are available in order to obtain large strains in the soft foam. To prevent a sudden impact from the striker against the incident bar and to achieve better force equilibrium and constant strain rate during testing, pulse shapers made of softer material than that of bar are to be used [46, 50]. Numerous pulse-shaping trials were performed using different combinations of materials. For example, copper discs of thicknesses of 0.1 and 1mm, and different papers ranging from 100 to 240 GSM (Grams per Square Meter) were tested individually and in multiple combinations of each other. It was found that a 160 GSM paper pulse-shaper generated the desired near-rectangular shape of the input

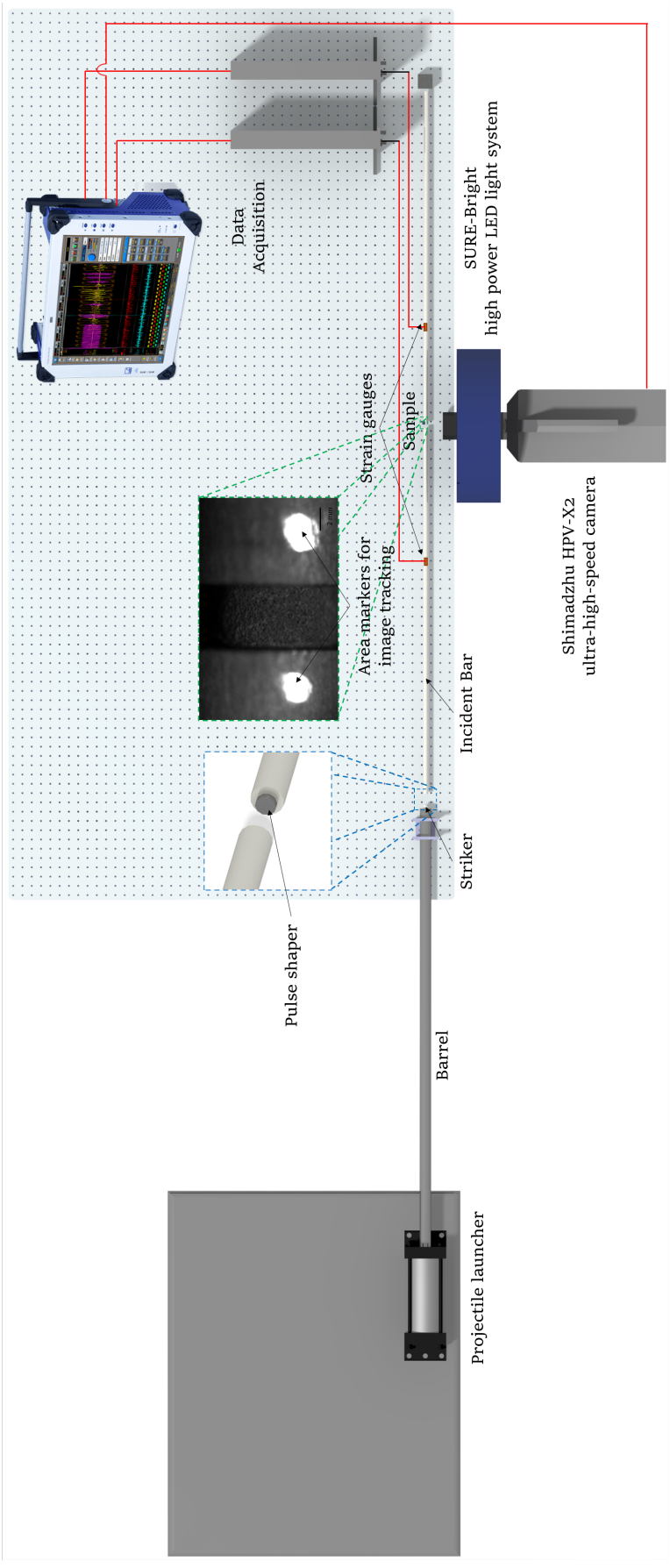

FIGURE 2.3: Schematic diagram of the Aluminium Split Hopkinson Pressure Bar experimental setup combined with Ultra-high speed camera for strain measurement and visualization of deformation features.

pulse, which would ensure constant strain rate and best force equilibrium throughout the experiment.

To compute the stress-strain responses of the material, the theory of one-dimensional wave analysis in thin rods is used:

$$\sigma(t) = \frac{A_0}{2A_s} E_0[\epsilon_i(t) + \epsilon_r(t) + \epsilon_t(t)] \tag{2.1}$$

$$\epsilon(t) = \frac{C_0}{L_s} \int_0^t [\epsilon_i(t) - \epsilon_r(t) - \epsilon_t(t)]dt \tag{2.2}$$

$$\dot{\epsilon}(t) = \frac{C_0}{L_s} [\epsilon_i(t) - \epsilon_r(t) - \epsilon_t(t)] \tag{2.3}$$

where $A_0(m^2)$ and $A_s(m2)$ are the cross-sectional areas the bars and sample; $\epsilon_i(t)$, $\epsilon_r(t)$ and $\epsilon_t(t)$ are the incident, reflected and the transmitted strain-time histories respectively; $L_s(m)$ is the thickness of the sample; $E_0(N/m^2)$ is the Young's modulus of the bars and $C_0(m/s)$ is the elastic bar wave speed which is given by

$$C_0 = \sqrt{\frac{E_0}{\rho_0}} \tag{2.4}$$

where $\rho_0(kg/m^3)$ is the density of bar. Since the sample size is small, it can be assumed that the wave propagation effects within the specimen are negligible and this yields:

$$\sigma(t) = \frac{A_0}{2A_s} E_0 \epsilon_t(t) \tag{2.5}$$

And equations (2.1) - (2.3) are simplified to

$$\epsilon_i(t) + \epsilon_r(t) = \epsilon_t(t) \tag{2.6}$$

$$\epsilon(t) = -2\frac{C_0}{L_s} \int_0^t [\epsilon_r(t)] \tag{2.7}$$

$$\dot{\epsilon}(t) = -2\frac{C_0}{L_s} [\epsilon_r(t)] \tag{2.8}$$

To validate the working of the Kolsky Bar apparatus, it is necessary that dynamic stress equilibrium be attained in the samples [31] and this is verified by equating the forces

at input bar–sample ($F_{S-I}(t)$) and sample–transmission bar ($F_{I-T}(t)$) interfaces, which are given by:

$$F_{S-I}(t) = A_0 E_0[\epsilon_i(t) + \epsilon_r(t)] \tag{2.9}$$

$$F_{I-T}(t) = A_0 E_0 \epsilon_t(t) \tag{2.10}$$

Shown in Figure 2.4 (a) is a force balance plot between forces calculated at the incident and transmitted ends of the sample. The vertical axis represents the force experienced in Newtons (N) and the horizontal axis represents time in microseconds (μs). The forces at the input bar–sample ($F_{S-I}(t)$) and sample–transmission bar ($F_{I-T}(t)$) interfaces are represented by black and brown curves, respectively. The overlapping of the curves indicate that reasonable dynamic force equilibrium is attained within the sample.

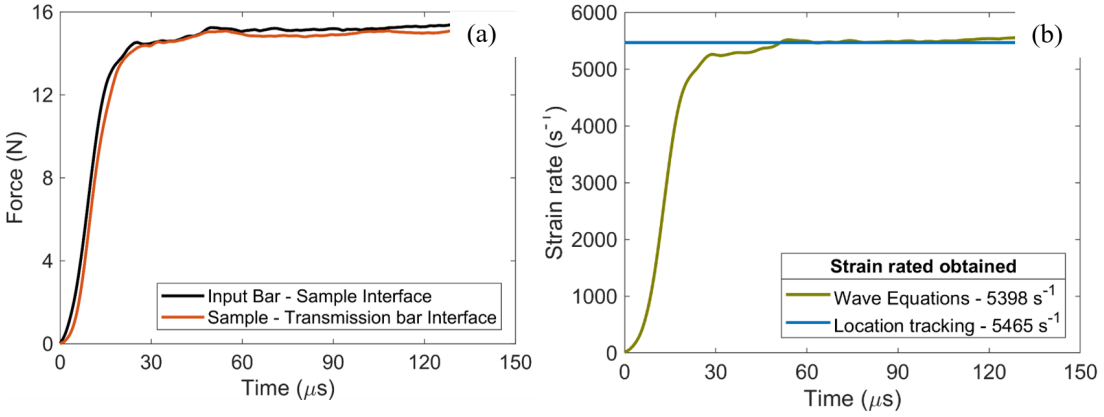

FIGURE 2.4: (a) Plot showing dynamic force balance between foam sample's end surfaces during dynamic compressing testing using Split Hopkinson Pressure Bar (Kolsky Bar). (b) Strain rate history of the sample observed during dynamic compression using wave equations, and using location tracking technique which tracks markers on Ultra-high speed camera images to calculate strain and strain rate. Both based on individual MATLAB programs.

During testing, an ultrahigh-speed camera Shimadzu HPVX-2 was used to visualize deformation features, as well as to perform strain measurements. The camera is able to capture 256 images and is triggered by a split signal from the incident strain gage. In these experiments, the camera operated at a framerate of 1 million frames per second at a resolution of 400 x 250 pixels. The camera was triggered from the incident strain gage and camera output pulses were used to correlate times between the images and the gage measurements. In the dynamic experiments, strain was measured by tracking overall displacements along edges of platens on either sides of the specimen. In each experiment, strain was tracked by tracking the displacement of two area markers on each

side of the tested specimen, one on the incident bar and the other on the transmission bar which contained between 15 to 20 points, depending on contrast and brightness of the area that was being tracked. This was done to more easily match the video images to the stress-strain curve in order to identify macroscopic deformation features that are observed in this material. Uncertainty of using the camera is approximated to lie within an error of one pixel where the initial sample size was measured to be 100 pixels in length, corresponding to a maximum strain uncertainty of 1%. A comparison of the strain rate vs. time computed for one of the experiments using the wave equations (equation (2.8)) and the rate vs. time computed from tracking the displacements from the high-speed camera are shown in Figure 2.4(b). The horizontal axis represents time in microseconds and the vertical axis represents strain rate (s^{-1}). The green curve shows the unfiltered strain rate obtained from the wave equations and the blue curve represents the strain rate history achieved using the ultrahigh speed camera. The blue curve was plotted by taking the slope of the strain vs. time, where the strain was measured using the ultra-high-speed camera. The global strain vs time was found linear throughout the entire event and so the strain rate is depicted linearly in Figure 2.4(b). The linearity is likely a result of not having enough resolution at corresponding framerates to measure minor variations in strain and strain rate. It was found that the strain rate calculated from the tracking technique lied within 3% error of the rate calculated from the wave equations for any given time after stress equilibrium has been obtained (i.e. at strains greater than 8%). Finally, three tests with same loading conditions were performed to verify repeatability of the experiments and it was found that with the same cylinder pressure, there was a variability of $\sim 5\%$ in the projectile velocity, which caused a variability in strain rates of 5284 to 5720 s^{-1}.

2.5 Experimental Results

Shown in Figure 2.5 is a plot of the quasi-static and dynamic stress-strain curves of the D3O LITE D, including multiple curves for experimental variability. The x-axis denotes the absolute strain and the y- axis depicts stress in log scale. The points 1 to 8 included on one example quasi-static and one example dynamic curve correspond to high-speed camera images that are shown and discussed later in Figure 2.6 and 2.8. The strains for which images are selected are different for the quasi-static and dynamic cases. For the quasi-static case, strains are selected at transitional points on the stress-strain curve, as well as those strains that correspond to the onset or evolution of notable deformation features in the images. Similarly for the dynamic experiments, image locations are selected to best visualize the onset and evolution of deformation features for the higher

strain rate. The results for both quasi-static and dynamic strain rates are discussed in greater detail subsequently.

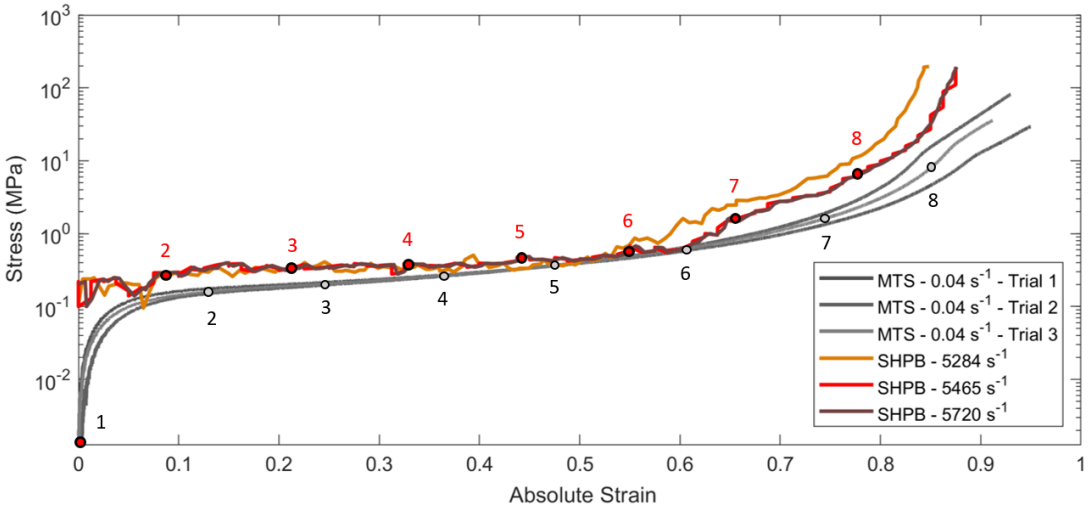

FIGURE 2.5: Stress-strain curves from quasi-static and dynamic compression experiments. Black points on the quasi-static curve are represented by high-speed camera images in Figure 6; Red points on the dynamic curve are represented by ultra-high speed camera images in Figure 2.8.

2.5.1 Quasi-static Regime

It is observed that the compressive response of the material in the quasi-static regime exhibits a typical elastomeric foam behavior with a few notable exceptions. Namely, typical foam responses have a sudden change in slope when the stress reaches elastic stress limit σ^*_{el} and its value is easily identifiable. However, in this material, it was found that there was a gradual transition from the elastic regime to the plateau regime beginning at a strain of 2% and plateauing at approximately 6% strain, which does not yield a specific value of σ^*_{el}. Therefore, average stress over the specified strain range between 4.6 to 5.2% was calculated, where an initial increase in slope is observed, and σ^*_{el} was measured to be $120 \pm 55kPa$ over this range. In the figure, the curve then starts to plateau at around 6% at a stress of about $145kPa$, indicating the start of post-elastic collapse regime. From this point, the sample continues to harden with a linearly increasing hardening rate until a strain of $\sim 60\%$ is reached within the sample. The sample then starts to densify at an increasing rate until a strain of $\sim 83\%$ at a stress of $5.05 \pm 2.1MPa$ is reached in the sample, at which point the sample starts to densify rapidly. It is also observed that there was a sudden increase followed by a gradual decrease in the hardening rate at this strain. The strain of $\sim 83\%$ coincides with the porosity of the material, and so this hardening behavior likely corresponds to near-complete pore collapse. At this point, the porosity is completely crushed out and the foam tends to behave linearly like the elastic part of the

compressive behaviour of the parent bulk polymer [10, 49]. To understand the variability in the material behavior and consistency of the mechanical properties obtained from the experiments, three stress-strain curves under the same strain-rate and loading conditions were obtained, and these are also shown in Figure 5. It can be seen that below strains of 70%, the stress-strain curves overlap within 4% error, and the variability observed after 70% strain are related to the differences in material composition, individual sample density and microstructure. For a given sample, the pore collapse strain ranges between 114 and 126kPa, while the stress variability at 90% strain can range between 28 and 44 MPa.

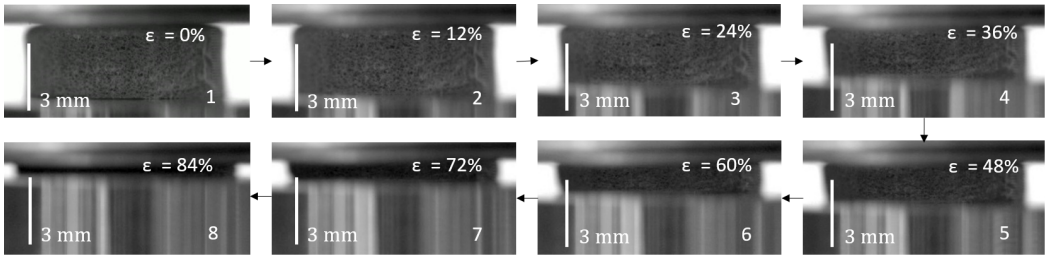

FIGURE 2.6: Time-evolved quasi-static compression failure of the D3O foam at $0.04s^{-1}$ using MTS 810 apparatus. Inter-frame strains are denoted at the top-right corner of each image and specimen length scales are denoted on the bottom-left corner of each image. Large-scale linear deformations are not observed in the quasi-static case, like the dynamic case.

To better understand the failure mechanisms that influence the stress-strain responses, images taking using a high-speed camera during quasi-static testing are presented in Figure 2.6. The image numbers correspond to the numbers shown on the quasi-static stress-strain curves in Figure 2.5. Image 1 shows the start of the experiment at 0% strain, and is shown for reference. From image 2, it is observed that from a strain of $0 - 12\%$, there is a small noticeable lateral deformation. This suggests that the Poisson's ratio may be negligible throughout the elastic regime and early plateau. This is consistent with observations by Liu et al. [63] for their polymeric foam (acquired from Airbus). As seen from images 3 through 6, very low lateral deformation is observed corresponding to a Poisson's ratios less than 0.01; no clear deformation features are visible on the material surface. In image 7, visually distinguishable deformation appears in lateral direction at a strain of $\sim 72\%$, and densification begins to occur ending the plateau regime. Finally, image 8 is taken at a strain of $\sim 84\%$, where considerable lateral expansion is observed and at strains higher than this, the sample moves out of the camera's field of focus. All of lateral deformation measurements were performed using ImageJ. Given that the specimen is cylindrical, it was assumed that transverse strain observed is uniform. The transverse strain was calculated by measuring the radial expansion of the specimen by estimating the diameter using the line function in ImageJ. These diametrical changes

were measured using the tangent equation following convention [68]. This was done at five equidistant locations across the thickness at specific strain intervals and transverse strain is averaged. Poisson's ratio was calculated by taking the ratio of transverse strain to the longitudinal strain. Throughout the range of strains, it was observed that there were no distinctive macroscopic deformation features on the imaged surface, which are contrasted with dynamic results next.

2.5.2 Dynamic Regime

Prior to discussing the stress-strain responses for the dynamic experiments in Figure 2.5, the authors first discuss the effect of filtering levels on the strain-strain curves presented in Figure 2.7. In our experiments, data from the oscilloscope was sampled at $500MHz$ (fixed oscilloscope setting), and filtering techniques were explored to better visualize the raw data and contrast it with the quasi-static experimental trends (e.g., features like the elastic collapse, densification). Some level of filtering of high strain-rate data appears to be frequently used in the published literature on foams [41, 46, 49, 50] (based on smoothness of curves), with limited discussion for filtering approaches (e.g., frequency-based filters [47]). To explore the effect of filtering, the authors use a first order Savitzky–Golay (SG) filter in Matlab, which helps increase the signal-to-noise ratio without greatly distorting the signal. The smoothing is achieved using a process called convolution, which fits segments of adjacent data points with a low-degree polynomial by the method of linear least squares. The choice of this filter allows maintaining the general trends and stress magnitudes in the data (which the authors explore here). In this exercise, the authors show the effect of different filtering levels for one of the dynamic experiments in Figure 2.7. Here, the authors selected to apply filtering levels beginning at filtering segment sizes corresponding to 0.05% strain and increasing by 0.05% strain up to 1%, which the authors believed to represent low degrees of filtering when first selected. The figure shows an unfiltered curve, and curves for filtering levels for segment sizes of 0.2% (corresponding to 180 points), 0.5% (corresponding to 450 points), and 1% (corresponding to 900 points). The black curve shows the unfiltered data, followed by the red curve which corresponds to a segment size of 0.2% strain. It can be seen that the red curve overlaps over the black curve in all ranges of strain suggesting that both magnitudes and trends are preserved at this level of filtering. Increasing the strain segment size to 0.5% strain leads to a three fold reduction in elastic collapse stress, as well localized distortion of the general trend at low strains which are represented by the light grey curve. The dark grey curve represents filtering corresponding to a strain segment size of 1% and it can be observed the overall trend is captured but stress magnitudes

are reduced drastically with increasing segment sizes. These values demonstrate the outcome of the analysis. Namely, it was observed that increasing the strain segment size to greater than 0.25% strain leads to distortions of the general trend and decreased stress magnitudes, and so a size of 0.2% strain was selected because this lied within acceptable filtering levels.

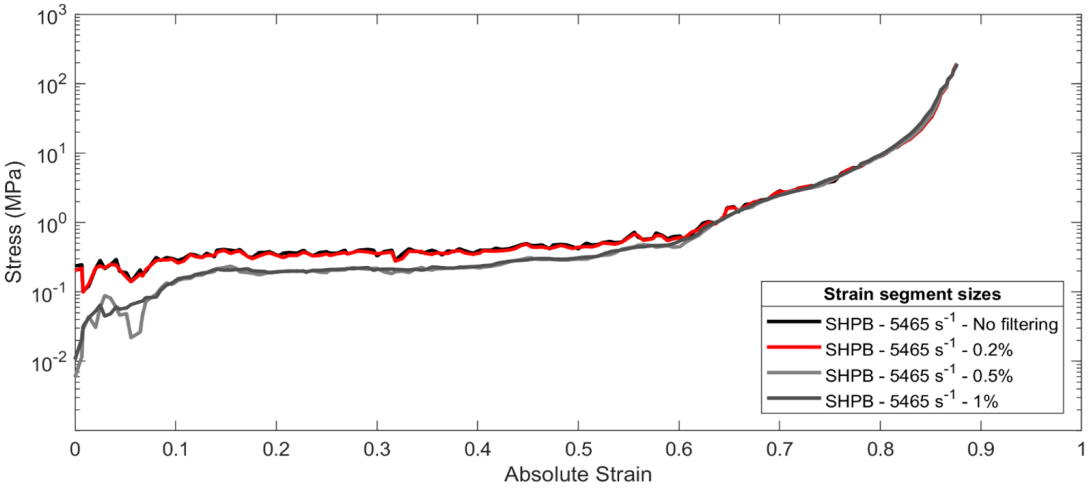

FIGURE 2.7: Plot showing effect of different filtering levels on stress magnitudes and global trends of dynamic compressive response of D3O LITE D foam. The red curve is indicative of acceptable filtering level with a strain segment size of 0.2%. The light grey and dark grey are example curves at larger segment sizes of 0.5% and 1% respectively, that show distortions from original response indicating over-filtering.

Now that filtering has been explored, the authors return to describe the stress-strain response of the foam in Figure 2.7 for strain rate of 5284 to $5720s^{-1}$. For the dynamic case, the linear-elastic regime spans up to a strain of 1% and the elastic collapse stress σ^*_{el} is calculated to be approximately equal to $243 \pm 47kPa$. In our experiments, the transition from the elastic regime to the plateau regime begins at a strain of 0.8% and plateaus at around 1.5% strain. The authors note here that the stress in the sample has not yet equilibrated (see Figure 2.4(a)), and care should be given to interpretation of these values as discussed in Song et al. [46]. In our tests, a constant strain rate and force balance is achieved in the sample at $\sim 8\%$. In the dynamic tests, the stress in the sample continues to rise between 8% (stress of $280 \pm 25kPa$) and 45% ($460 \pm 40kPa$) at a constant rate in this log-linear representation. This linear rise corresponds to an initial plateau regime. Interestingly, there is a secondary hardening regime beyond 45% strain that increases logarithmically until a strain of 81 to 83%($22.5 \pm 4.0MPa$). This pronounced hardening rate corresponds to densification of the foam sample. Again, this likely corresponds to pore collapse in the sample, albeit at a slightly less strain value than observed in the quasi-static experiments. After this point, there is an inflection in the curve at $\sim 83\%$, which is believed to correspond to complete densification. After a

strain of $\sim 81\%$ is achieved within the sample, the material hardens more rapidly than the quasi-static tests, and this likely corresponds the behavior of the parent material.

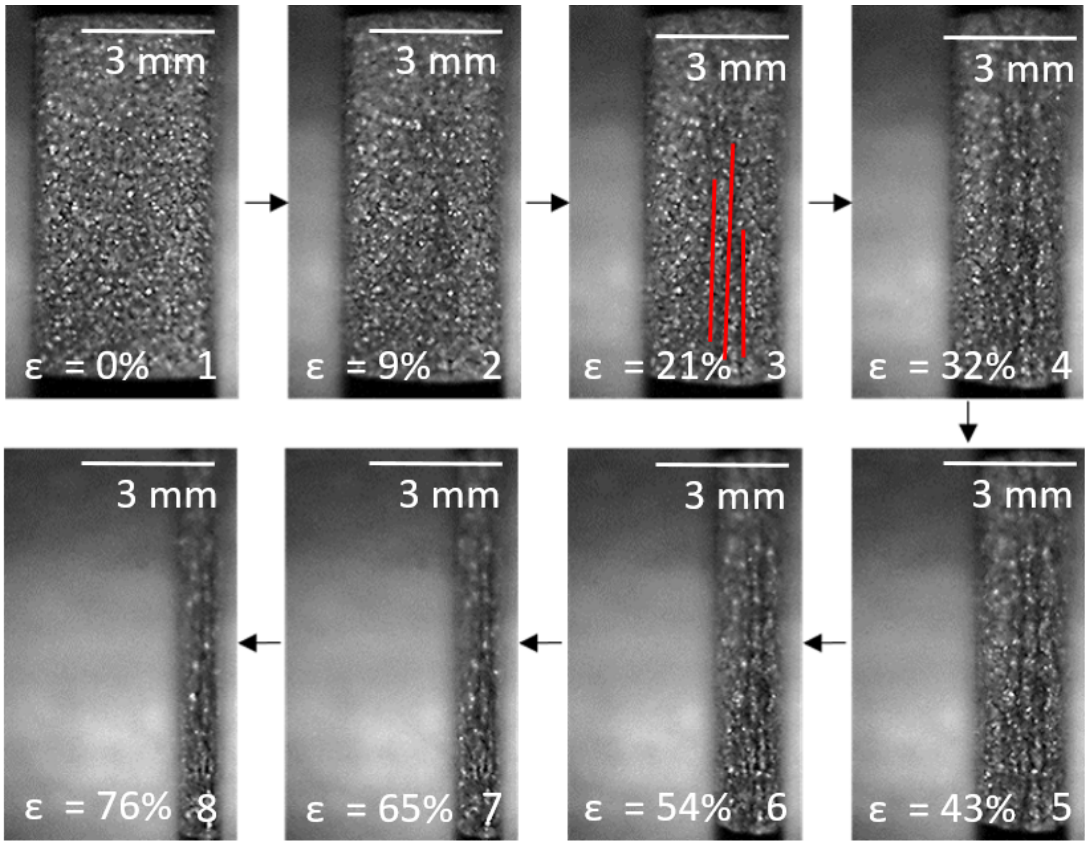

FIGURE 2.8: Time-evolved dynamic compression failure of the D3O at $5465s^{-1}$ using Split Hopkinson Pressure Bar apparatus. Inter-frame strains are denoted at the bottom-left corner of each image and specimen length scales are denoted on the top-right corner of each image. The red lines in image 3 emphasize larger-scale vertical localization bands that start to form in this material at approximately 10% strain. This corresponds to log-linear region in the red line in Figure 2.5.

To better understand the hardening regimes, ultra-high-speed camera images taken during deformation (Figure 2.8) are presented. In this D3O LITE D foam, some unique macroscopic deformation features are observed. Shown in Image 1 of Figure 2.8 is a reference image taken at 0% strain for the dynamic experiments. Image 2 corresponds to strains of around $8 - 10\%$, where small band-like features begin to appear. Image 3 shows the sample at 18 to 20% strains where these features become more visually apparent as indicated by the red lines in the image. Note the red lines are used to highlight the location of these vertical bands and this meant to ease the reader in visualizing the growth of the bands in subsequent images. These band-like deformation features are termed as "localizations" hereafter. It was observed that at strains between $20 - 35\%$ (Image 4), a greater number of localization features appear to nucleate, and this corresponds to the near-horizontal plateau in the log-linear regime of the stress-strain curve

in Figure 2.5. These localization features continue to nucleate and grow perpendicular to the compressive loading direction until strains of $42 - 45\%$ are reached within the sample, shown in image 5. After 45% strain, no more new nucleations are observed in the ultra-high-speed camera images, and at strains beyond 45%, the localizations begin to coalesce with each other until they span the entire length of the sample at 75 to 80% strain (shown in images 6 to 8). In the dynamic experiments, lateral expansion was measured at the aforementioned strains using ImageJ and a constant expansion rate was observed leading to a Poisson's ratio of ~ 0.11. After strains of $85 - 90\%$ are reached, the sample expands out of the field of focus of the camera.

2.6 Discussion

This paper investigated the compressive failure of a shear-thickening polymeric foam for quasi-static and dynamic conditions. It is important to better understand the behavior of these materials since this class of foams are currently being employed in energy absorption equipment (e.g., helmet liners for US team sports such as football, baseball and ice hockey, as well as protective inserts for Motorcycle jackets) and also in some military applications [69]. Limited data on these materials, and shear thickening foams in general, exist in the literature, and so the authors believe that this paper makes contributions towards better understanding how microstructural features and lengths scales of these types of foams may be related to quasi-static and dynamic compressive failure. In what follows, the authors discuss the results of this foam in the context of their general understanding of how polymeric foams behave.

To summarize the results and discussion of this paper, Table 2.2 is presented which consists of the stress regimes, Poisson's ratio measurements (ν) and the dominating failure mechanisms corresponding to that given ranges of strains. This table also provides image numbers corresponding to images from high speed camera for quasi-static case, and similarly for ultra-high speed camera images for the dynamic case from Figures 2.6 and 2.8 respectively, so that it is easier for the reader to visualize camera images while referring to the table.

First, the authors correlate commonly known deformation mechanisms to the stress-strain curves of our D3O LITE D foam in quasi-static and dynamic conditions (Figure 2.5). Generally, three different phases of deformation are observed during compressive failure of polymeric foams [17, 22, 49]. The first phase is linear-elastic regime, where the stress-strain response follows Hooke's law and the strain is completely recoverable. For polymeric foams, the linear-elastic limit is limited to small strains, typically less than 5% strain [41, 46]. It is to be noted that elastomeric foams can undergo much higher strains

than these and the deformation can still be mostly recoverable, but is non-linear [22]. The second phase is characterized by non-linear elasticity, where the material continues to plateau at a relatively constant stress, known as the elastic collapse stress σ^*_{el}. This property of foams is exploited for energy-absorbing applications [17]. The third and final phase of deformation is known as densification, where the foam begins to respond like a compacted solid [41, 49]. For semi-closed cell foams, these deformation and failure mechanisms are usually more complicated than fully open or closed celled foams due to the presence of higher number of face edges where damage can nucleate [47]. Each of the three phases is explained in the context of our material hereafter with a main focus on dynamic response.

In our dynamic experiments, the linear elastic regime extends to about $1-1.5\%$ strain and in this regime all stresses are carried by only the cell ligaments, which show small regions of buckling, directly contributing towards the stiffness of the material. There is no failure in the linear elastic regime and the strains are fully recoverable. Similar mechanisms are observed in the quasi-static case as well, but at different elastic strain limits as discussed earlier. In our dynamic experiments, the post-elastic collapse behaviour begins at around 1.5% strain and is dominated by buckling of both cell edges and faces. This mechanism spans the entire inelastic regime. In the first plateau, permanent bending of cell walls dominates up to a strain of $\sim 45\%$ alongside large-sized buckling regions near the cell walls. In the second plateau region following the permanent deformation of the cell walls, the cell faces begin to rupture followed by tearing of the cell edges at strains of $\sim 62\%$, and this process occurs progressively in the rest of the plateau regime. Initial damage is observed at the near-closed cells, and these cells begin to rupture at the strain nearing the end of plateau, reaching to the point of densification, which begins at around 81% strain. In our quasi-static experiments, the post-elastic collapse behaviour begins at $\sim 6\%$ strain and hardens linearly until $\sim 60\%$ strain after which gradual densification is observed up to strains of $\sim 83\%$. Similar failure mechanisms that have been discussed for dynamic conditions are activated in quasi-static conditions at similar strains except for that of complete densification. A deviation from typical foam behaviour [10, 17, 18, 20, 22, 49] in our experiments was that the hardening rate of the plateau stress was found to be more than an order of magnitude higher than the elastic collapse stress in quasi-static rate and almost two orders of magnitude higher in dynamic strain rate conditions. At these high strains, the opposing cell walls have been observed [49] to crush together and cell wall material is itself compressed and complete densification is observed. It is to be noted that each failure mechanism, once activated continues to remain active until failure.

After densification, complete pore collapse is observed. In the quasi-static case for our experiments (Figure 5), there was an inflection at the curve around $87 \pm 3\%$, and it is

TABLE 2.2: Summary table showing the stress regime, Poisson's ratio (ν) and the dominating failure mechanism corresponding to the given ranges of strains. It is to be noted that each failure mechanism, once activated continues to remain active until failure. Also, image numbers corresponding to that of Figure 2.6 are provided for high speed camera images for quasi-static case, and similarly for ultra-high speed camera images for the dynamic case with respect to Figure 2.8

2*Strain range	Quasi-static				Dynamic				
	#	Stress Regime		Failure mechanism	#	Stress Regime		Failure mechanism	Deformation features
0 – 10	1	Linear elastic	0.064	Elastic Collapse	1	Linear elastic	0.095	Elastic Collapse	None
10 – 20	2	Plateau	0.064	Buckling	2	First Plateau	0.095	Buckling	Nucleations begin
20 – 30	3	Plateau	0.075	Buckling	3	First Plateau	0.061	Cell Wall Bending	Higher Nucleations
30 – 40	4	Linear Hardening	0.042	Cell Wall Bending	4	First Plateau	0.089	Cell Wall Bending	Nucleations stop
40 – 50	5	Linear Hardening	0.064	Cell Wall Bending	5	Secondary Hardening	0.089	Pore Collapse	Localizations grow
50 – 60	6	Linear Hardening	0.053	Pore Collapse	6	Secondary Hardening	0.100	Pore Collapse	Growth & Coalescence
60 – 70	6	Densification	0.204	Pore Collapse	7	Densification	0.122	Tearing	Growth & Coalescence
70 – 80	7	Densification	0.569	Tearing	8	Densification	0.111	Complete pore collapse	Full sample length
80 – 90	8	Complete Densification	-	Complete Densification	-	Complete Densification	-	Post-pore collapse	-

likely related to complete pore collapse. In the dynamic case, the inflection was observed around $83 \pm 3\%$, which was lower than the quasi-static. The formation of the structural-scale vertical localizations are believed to be responsible for the lower pore collapse strain in the dynamic case as a result of these localization features consuming porosity during their nucleation, growth, and coalescence. This factor needs to be considered in any dynamic failure modelling of foams where large strains at high strain rates are experienced because the formation of these localizations govern the hardening rates in the plateau regime, which in turn are responsible for material response at high strain rates. Lastly, after complete pore collapse, post pore collapse hardening was observed. Post pore collapse hardening rates in both quasi-static and dynamic cases are found to be greater than the rate of densification in their respective cases. The dynamic post pore collapse hardening rate is observed to be greater than the quasi-static post pore collapse hardening rate. This is explained by the general rate dependency behaviour in bulk polymers [50] at high strains given when the entire porosity in the foam is crushed out, the sample essentially behaves like a bulk polymer material. Although not explicitly reported by the authors, similar effects are observed in other materials [22, 49]. After this point, at very large compressive strains of over 85%, the sample under the given mechanical loading tends to behave like material response of the parent material. It is to be noted that the vertical axis shown in Figure 2.5 is of log scale and these hardening rates may not be as easily visualized in the stress-strain curves presented in the paper.

The localization behavior foams advertised as shear thickening is not currently understood, but is likely related to some combination of chemical composition and structure (held proprietary by the manufacturer), the microstructure (in terms of pore size and wall thickness), and the strain energy that is available for failure (assessed via mechanical testing and stress-strain response). Additional experiments are needed to better understand the mechanisms for nucleation and growth of the localization features (e.g., interrupted compression or impact experiments coupled to X-Ray imaging of internal microstructure features), and energy-based or computational models are required to confirm experimental observations.

With this in mind, the authors briefly explore potential reasons for the observed localization features in this foam, which, to the knowledge of the authors, are unique to this as-advertised shear thickening foam. As mentioned, these localization features are believed to be a consequence of chemical composition and structure, and the microstructure (i.e., in terms of pore size and wall thickness). In this discussion, the authors focus on the microstructural contributions since the chemical composition, structure information and foam manufacturing processes are proprietarily held by the manufacturer. The authors link the localization features to instabilities that lead to buckling of cell walls perpendicular to the compressive loading direction. The onset of these instabilities are

believed to be related to the relative sizes of the pores and the wall thickness, where relatively large pore sizes results in relatively higher localized stresses concentrations, and relatively thinner walls are more susceptible to collapse under these relatively higher stresses. In this D3O LITE D material, the ratio of pore sizes (average of $82 \pm 26\mu m$) to wall thickness (average of $8.3 \pm 4.5\mu m$) is 4.3 to 28 (average 9.8). In other materials, where SEM images are available, the authors observe wall thickness to pore sizes ratios of ~ 0.025 and ~ 0.002 [54, 58], and perhaps these ratios play a role in the unique behavior of the Lite D foam. It is, however, to be noted that these materials have different compositions, and this form of foam microstructure with its unique wall thickness to pore size ratio, pore shapes, distributions, and locations of unexpanded polymer is found to be unique to D3O LITE D when compared to other images of foam microstructures in literature [7, 10, 41, 47].

2.7 Conclusion

The compressive response of D3O LITE D dilatant foams under quasi-static strain rate of 0.04 s-1 and dynamic strain rate of 5284 to $5720s^{-1}$ has been studied. Experimental methods for characterizing and studying the dynamic response of foams have been established and have found to reconcile with traditional experimental techniques. Comprehensive insights into compressive behavior of shear thickening foams are provided, which is relatively an unexplored area of research despite current use of these materials in many applications. Most notably, under dynamic loading conditions, unique macroscopic localization features are observed in the D3O LITE D foam under investigation in this paper, which do not appear at quasi-static rates or in any high rate testing of other polymeric foams (to the knowledge of the authors). This data can be used for modelling the observed localizations as a unique failure mechanism in mechanism-based modelling approach to predict material response. More studies at intermediate strain rates are required to identify the threshold strain rate for these localizations and to study the effect of these localizations on shear thickening behavior. As this is the first time that the D3O LITE D foams have been characterized in this way, the authors believe these experimental results will also serve as a good starting point for impactful modelling [7, 20]. The results of the tests performed and the future tests will be put together to make models to predict the effect of microstructure, strain rate and localizations on the compressive response of shear thickening foams.

Chapter 3

Quasistatic response of a shear-thickening foam: Microstructure evolution and Infrared thermography

Published as **Kapil Bharadwaj B**; Parcon, JS; Azar, A; Dennison, CR; Satapathy, S; Ouellet, S and Hogan, JD. *Quasistatic response of a shear-thickening foam: Microstructure evolution and infrared thermography*, Journal of Cellular Plastics. (2020)

Author	**Contributions**
Kapil Bharadwaj B	Conceived the ideas and experimental design of the study; Performed experiments/data collection; Data analysis and interpretation; Primary author (drafted the manuscript)
Parcon, JS	Data analysis and interpretation; Methods section - secondary author
Azar, A	Provided revisions to scientific content of manuscript
Dennison, CR	Provided revisions to scientific content of manuscript
Satapathy, S	Provided revisions to scientific content of manuscript
Ouellet, S	Provided revisions to scientific content of manuscript
Hogan, JD	Provided revisions to scientific content of manuscript; Provided stylistic/grammatical revisions to manuscript; Principal investigator

3.1 Abstract

In this work, the thermo-mechanical response of a dilatant polymeric foam in quasistatic tension and compression is studied, focusing on the links between microstructure, mechanical response, and associated temperature rises in these materials. The authors study these links for a commercially-available shear-thickening foam, named D3O LITE D. Samples were tested under quasi-static conditions for a strain rate of $0.1s^{-1}$ in tension and compression. Micro X-ray computed tomography (XCT) was used to study the evolution of microstructure (pore size and wall thickness) as a function of strain and this was achieved by developing MATLAB-based programs to analyze these microstructural features. The foam specimens were loaded until failure which allowed for the investigation of the elastic, inelastic, and failure regimes. From the XCT images, pore stretching and cell wall tearing are observed in tension, and buckling and pore collapse are observed in compression. These mechanisms are studied in-situ using an infrared thermal camera which record temperature profiles, and temperature measurements are linked back to stress-strain, and temperature-strain responses. For this material, the tensile yield stress was $0.57 \pm 0.10MPa$ and the elastic modulus was $5.47 \pm 0.10MPa$ respectively, at a yield strain of 0.10 ± 0.04. At the time of failure, the average temperature of the specimen was found to increase by $\sim 3.00°C$ and a local temperature increase of $\sim 8.00°C$ was observed in the failure region. In compression, the elastic collapse stress and elastic modulus were found to be $0.130 \pm 0.016MPa$ and $2.5 \pm 0.2MPa$, respectively. The temperature increase in compression at ~ 0.83 strain was $\sim 0.65°C$. These results represent some of the first mechanical properties on shear-thickening foams in the literature, and the discoveries on the linkages between the microstructure and the mechanical properties in this study are important for researchers in materials design and modelling.

3.2 Introduction

Polymeric foams are widely used in many automotive [1, 70], aerospace [1, 70, 71], military [7, 71], and packaging applications [7]. Their energy absorbing capabilities and low density make them an ideal candidate for protection materials, such as personal protection equipment (PPE) like knee pads [7] and, specific to this study, helmet liner materials [7, 17]. One specific type of foams are dilatant, or shear-thickening polymeric foams which react like a rigid material when subjected to high stress or deformation rates [25–27], making them considerable candidates for protection materials. This hardening mechanism allows for higher energy absorption during high rate and impact loading conditions. Recently, Traumatic Brain Injury (TBI) has received increased attention in all

fields, especially the military. The main function of the inner liner of the helmet, generally made of closed cell polymeric foams [17], is to absorb part of the impact/ballistic energy and to reduce the amount of load transmitted to the head which directly contributes to TBI. To make efforts toward improving typical foams used in helmet liners, there exist a number of studies on compressive [7, 10, 11], tensile [11, 12], shear [12], and fracture [16] behavior of these polymeric foams; however, minimal information is currently available with respect to shear-thickening foams. In this present study, we seek to understand the deformation mechanisms in tension and compression for a shear-thickening foam.

To fully exploit the energy absorbing capabilities of foam materials, it is necessary to understand, analyze, model, and validate the constitutive response of foams under multiple stress states. In the literature, less attention has been given to tension and other stress states [11, 12, 16] and more attention to compressive states [1, 7, 9–12, 20, 22, 70–73]. Ayyagari et. al [72] and others [11, 16, 21, 74] note the necessity of studying and understanding the mechanical behavior in polymeric foams under complex stress states for physics-based model development. These models are then used to determine parameters such as elastic moduli [11, 16], elastic collapse stresses [11], and failure strengths and strains [16] based on information from experiments, and microstructure, which enables industry to design better foam materials. Generally, polymeric foams have a definite isotropic compressive yield stress whereas dilatant foams tend to have a range of compressive yield stress at elastic collapse [9, 11, 25, 75, 76]. In one study, Ayyagari et al. [72] define the entire yield surface of isotropic foam materials which need only two yield strengths parameters from uniaxial compression and uniaxial tension experiments. In a separate study, Walter et al. [11] show in their model that the elastic moduli and failure strengths of polymeric foams increase linearly with foam density. Their phenomenological model predicts the constitutive response in both tension and compression. Ultimately, the benefit of creating models is gaining insights into how to control microstructure or composition (via manufacturing methods) in order to improve the foam performance for specific applications. These models require mechanical parameters that are obtained from experimental data, and this study seeks to contribute data for future modeling purposes.

In many studies, authors point to the importance of microstructure (usually in terms of density [7, 10, 18] and cell sizes [7, 10, 19]) and failure (usually through a post-test microscopic assessment of the sample [10]) on the material response of polymeric foams. It is well recognized that mechanical properties of polymeric foam materials depend on the properties of the base polymer material [4, 20], relative density [12, 21] (ratio of the foam density to the density of base material) and microstructural geometry (e.g., pore size and wall thickness) [7, 10, 19]. For example, Chen et al. [19] show the effect of variation of cell size and wall thickness on elastic and shear moduli of foams. In their study, material

properties are estimated through experiments, cell size and thickness distributions of the foam are measured from Scanning electron Microscopy (SEM) images, and existing models are applied to predict stiffness of the foam. Chen et al. [19] also note that variability in the cell wall thickness and cell size is important in overall tensile and shear response; this is important to note for this study since we characterize pore size and wall thickness which is then linked to foam response. In another study, Bouix et al. [7] show the differences in elastic collapse stress levels and plateau stress moduli that manifest due to microstructure differences in polypropylene foams. Also, the structural response of foams is strongly influenced by the cell geometry (foam apparent density, cell topology and anisotropy ratio) and by properties of the base material [18]. Thus, understanding the links between microstructure and mechanical properties is of great importance for designing next-generation foams.

Micro X-ray computed tomography (XCT) is a widely recognized characterization technique used to investigate the microstructure of a range of materials [71, 77–79]. With the development of XCT techniques, finite element models (FEM) based on the reconstruction of real foams using XCT have also been reported by many studies [36, 75, 80, 81]. For example, Fahlbusch et al. [81] describe a Representative Volume Element (RVE) - based model that predicts failure behavior of closed-cell polymeric foams whose microstructure information is extracted through XCT. This model shows the numerical and experimental failure points in foams in 11 different stress states for which experimental data exist. In another study, Youssef et al. [75] study the local deformation mechanisms of a polyurethane foam in compression by means of XCT. In their study, the XCT data is used to reconstruct the microstructure of the foam, and by using the constitutive equations of the bulk material and finite element modeling methods, the macroscopic response of the material is captured. There are other techniques to investigate microstructure such as SEM [16, 17, 47] or Fluorescence microscopy [82], but these are inherently two-dimensional and do not provide sufficient 3D information. In contrast, XCT offers an ability to determine 3D volumetric data, thus allowing researchers a tool to assess features at the microstructural level in 3D. Altogether, the literature demonstrates the importance of microstructure on the mechanical response of foams, and seek to contribute to this understanding in this paper.

In addition to efforts made to investigate failure [16, 83], develop models [11, 72], and characterize materials [73, 84], the sensitivity of mechanical response to temperature in foams is also well documented [18, 85–87]. For two different foam materials, Williams et al. [86] show that shear strength and stiffness properties of the foams exhibit an inverse relationship with temperature, whereas the shear strain at failure exhibits a linear relationship. Infrared (IR) thermography is one of the established methods to study the effects of temperature on failure and material behavior [38, 39]. Chrysochoos

[88] demonstrate the effective of use IR techniques to study material behavior such as thermo-mechanical characteristic analysis of fatigue mechanisms in polymers and steels. In a different study, Ohbuchi et al. [89] use thermal image analysis to visualize plastic deformation/crack propagation in stainless steel in quasistatic tension. This was developed by combining thermal image processing with elasto-plastic finite element analysis coupled with transient heat conduction calculations. These studies demonstrate the importance of temperature rises on mechanical behavior of materials. In the present study, mechanical tests are performed on a dilatant polymeric foams and the distribution of the specimen surface temperature is measured by using infrared thermography techniques. In this study, the main focus is on characterizing failure and show that temperature can also be indicative of failure, and that demonstration of these methods could be useful in studies considering temperature effects in addition to failure origin/propagation.

This current paper builds on past works investigating the effects of stress states, temperature, microstructure and failure on the mechanical response of polymeric foams. The present study is an extension of the work performed in a study by Bhagavathula et al.[25], where only the rate-dependent compressive response was examined. This current paper focuses on understanding the evolution of pore size and wall thickness on the behavior of the D3O LITE D shear-thickening foam in quasistatic tension and compression. As limited work is available in published literature on shear-thickening foam materials, this study intends to establish a better understanding of microstructural length scales in quasistatic behavior of a particular shear-thickening foam, accomplished through experimentation and characterization. This paper is comprised of the following sections: first, thermography techniques and sample preparation methods are established and described. Second, experimental methods are presented that include microstructure characterization techniques and mechanical testing methods, followed by the presentation of the experimental results. These results are supported by stress-strain curves, cumulative distribution functions of microstructural parameters, X-Ray tomograms, and infrared video images obtained from the infrared camera. Finally, results are discussed in the context of our understanding of quasi-static behavior of polymeric foams.

3.3 Experimental Methods

In this study, a shear-thickening foam obtained from D3O is studied. D3O foam is used in padding on sports equipment and currently investigated for use in ballistic protective equipment [60, 90]. The variant under investigation is D3O LITE D, which is a partially open and closed-cell polymer-based material. The foam density is reported as $220kg/m^3$ and the chemical composition is held proprietary by the manufacturer. Some

of the physical and mechanical properties provided by the manufacturer are listed on the manufacturer website [60]. The motivation in characterizing this material stems from the lack of testing of this highly marketed non-Newtonian shear-thickening foam, and this study aims to determine the behavior of this material over various stress states [25].

3.3.1 Sample Preparation for Mechanical Testing

Tensile dog bone specimens were used in this study and were manufactured using water jet cutting – an accepted sample preparation technique in experimental studies [91]. The dimensions of the gage section were 20 mm in length and $10mm$ in width with a thickness of $4mm$, which is governed by the thickness of the as-received foam sheet. The tensile dog-bone samples were designed with ASTM D3575 Standard [92] as a starting point (geometric ratios of the samples follow the standard), but were scaled down in dimensions to allow for sufficient longitudinal displacement until failure. For compression specimens, a hollow metallic punch was used to punch disk samples of diameter $8 \pm 0.3mm$ from an as-received sheet of uniform thickness of 4mm, with the axis of the disk oriented along the through-thickness direction of the foam sheet. Following traditional procedures for performing the infrared measurements, one of the specimens' faces was completely painted black using an airbrush. This is consistent with other practices in the literature [87, 89] for reducing reflection from the sample surface, and thus increasing the accuracy of the thermographic measurement. It was ensured that the samples end surfaces were parallel and that minimum damage was induced to the edges during sample preparation. The sensitivity of material strengths to geometry and specimen-size effects are widely discussed in the literature [16, 22], and it is expected that similar differences could be observed in our strengths and those provided by the manufacturer as different testing conditions may have been followed. It is noted that potential differences in composition, pore size, and wall thicknesses may also occur as a result of different sizes of received sheets when comparing across studies and those listed by the manufacturer.

3.3.2 Quasistatic Tension Experiments

The specimens were tested in tension at a quasistatic strain rate of $0.1s^{-1}$ using a Material Test System (MTS) - 810 machine. This assembly included infrared visualization capabilities with a high-speed infrared camera - FLIR X8503sc, which enabled us to observe temperature changes during testing. Details of the camera are discussed in the next sub-section. Both the camera and MTS machine were triggered manually at the same time, and synchronization was verified through comparison between when the piston displacement was first observed in the thermal images with the displacement data

recorded by the MTS machine (no adjustments were necessary). To perform the tension experiments, the specimens were mounted on screw-type tension grips with adequate surface area provided for clamping the sample. A $10kN$ load cell with a background noise corresponding to approximately 1N recorded the time histories of the forces, and the displacement of the piston was measured to an accuracy of $0.001mm$. The tension grips were connected to the load cell and the actuator displacement rate was set to be $2mm/s$, corresponding to a strain rate of $0.1s^{-1}$ in the sample. Specimens were driven to failure in all experiments. The engineering stresses are calculated by dividing the applied load by the original specimen gage surface area. The engineering strains are computed by dividing the gage displacement in the camera images by the original gage length.

3.3.3 Quasi-static Compression Experiments

The specimens were tested in quasistatic compression at a strain rate of $0.1s^{-1}$ using an Instron E3000 machine. Both camera and Instron were triggered manually at the same time, and the synchronization was verified through comparison between when the piston displacement was first observed in the thermal images with the displacement data recorded by the Instron machine (no adjustments were necessary). A cylindrical piston, moving at a constant displacement rate was used to compress the samples. The actuator speed was set to $0.42mm/s$, corresponding to a nominal strain rate of $0.1s^{-1}$ in the sample. Since no data regarding material densification was available before experimentation, the tests were terminated based on two conditions: first, when near-complete densification was observed in the force-displacement curve during loading, and second, when the actuator speed was no longer constant. Specimens were driven to densification in compression and strains exceeding 0.90 were achieved in all the quasi-static compression trials. The engineering stresses are calculated by dividing the applied load by the original specimen surface area, and the engineering strains are computed by dividing the specimen displacement by the original specimen height.

3.3.4 Infrared Thermography Methods

An infrared high-speed camera - FLIR X8503sc system was used in this study for temperature measurements. The Thermal Sensitivity/ noise equivalent differential temperature (NEdT) of the FLIR x8503sc infrared camera is $< 20mK$ as specified by the manufacturer. Further specifications of the infrared camera are shown in Table 3.1. The infrared thermal images and temperature data were recorded at a rate of 100 frames per second. At this frame rate, the FLIR X8503sc system provided 1280 x 1024 pixel resolution and this was sufficient to capture the whole loading event until failure. The integration time

was $1.0432ms$. For the camera temperature calibration, the FLIR X8503sc camera is placed within a temperature controlled chamber and set to visualize a blackbody outside the chamber through a hole in the chamber wall [93]. The chamber temperature is then cycled from ambient to highest specified operating temperature, then down to lowest, then back to ambient. A correction curve is generated from the data recorded and saved in the camera as part of the factory calibrations. These measurements are compared to a National Institute of Standards and Technology (NIST)-calibrated thermocouple. The calibration is performed for a range of temperatures. The infrared camera directly records all data to an onboard solid-state disk (SSD). To obtain temperature measurements during experiments, the detector output of the thermal camera is estimated from emissions of both target body and that of background. These emissions depend on ambient temperature, Ta ($^{\circ}C$), target temperature, T ($^{\circ}C$), and target emissivity, ϵ. The measurement principle applied in this thermography method is given by:

$$V(T, T_a) = \epsilon W(T) + (1 - \epsilon) W(T_a) \tag{3.1}$$

where $V(T, Ta)$ is the detector output, $W(T)$ is the Black body emission energy, $\epsilon W(T)$ is the emission of the target, and $(1 - \epsilon)W(Ta)$ is the background emission. The emissivity of the target body depends on its surface condition. The accuracy of the temperature measurements increases with increase in the emissivity of the surface [87, 89]. For example, for highly reflective (polished) surfaces, the emissivity and corresponding temperature readings will be lower. This has been a challenge for ductile materials [87], and has resulted in many authors painting their surfaces black [87, 89]. In this study, following convention, the target specimen was sprayed with black paint to obtain a higher emissivity of 0.92. The accurate measurement techniques of emissivity have been proposed [94], but there are many difficulties because of various kinds of errors, especially the atmospheric transmission coefficient. The coefficient of the band transmittance of the atmosphere should be estimated accurately because it is an important factor for measuring temperature with such a method when the distance between the measured surface and the camera is very large [94]. In our experiments, the distance between the camera and the object was only $0.25m$, so it can be assumed to be unity in this experiment. In the experiment, the ambient temperature was recorded to be $\sim 21^{\circ}C$. Before the experiment, the specimens were kept in the test room for hours to equilibrate to the room temperature.

The temperature data measurement was made using the FLIR ResearchIR software's rectangular region of interest (ROI) function and conforming to camera positioning, and selecting a fixed ROI on the sample surface for the entire course of the experiment was not possible, necessitating an external program for temperature data analysis. This software

TABLE 3.1: General specifications of the FLIR X8503sc infrared camera

Detector Type	FLIR indium antimonide (InSb)
Spectral Range	3.0 – 5.0 m
Full Resolution	1280 x 1024 pixels
Thermal Sensitivity/NEdT	<20 mK
Frame Rate (Full Window)	Programmable; 0.0015 Hz to 180 Hz
Accuracy	2% of reading
Standard Temperature Range	-20C to 350C (-4 F to 662 F)

allowed for export of csv files containing individual pixel temperatures of every infrared image. These csv files were imported to MATLAB and a program was designed to track displacements and to calculate average temperatures on the samples. The infrared images are also exported as monochromatic tiffs and the edge of the tension grip is tracked using image processing techniques. The infrared image index is converted to strain by synchronizing with the testing machine data, and monochromatic TIFFs and csv files are synchronized through strain. The temperature data corresponding to those pixels containing the grips are deleted. The background pixels are also deleted using a threshold background temperature.

3.3.5 X-Ray Computed Microtomography

Synchrotron radiation based X-ray microtomography was used at the Biomedical Imaging and Therapy (BMIT) facility - Canadian Light Source (CLS)[95] 05ID-2 - SOE-1 hutch, Saskatoon, to obtain volumetric information of the microstructure. The facility's capabilities are mentioned in Table 3.2 [96]. Samples of 5 mm x 5 mm x 4 mm were manually cut from the center of the sample gage section for imaging. This was done so as to accommodate the sample on the mounting pad. The samples were mounted with their loading axis parallel to the scan direction. The beam energy was set to 30 keV. The imaging setup used a Hamamatsu ORCA FLASH 4.0 detector. This detector provided an effective voxel resolution of 3 m where the distance between the specimen and detector was 20 $pm1mm$. This resolution provides sufficient scan volume in order to resolve the cell wall thickness $(3-30\mu m)$, and pore size $(30-120\mu m)$ analysis. The sample loading stage operated in intermittent motion and each sample scan comprised of 900 tomograms being acquired within 10 minutes over 180° of rotation. Reference images without the sample, and dark images without X-rays were also obtained before and after every scan to increase the quality of images during background filtering reconstruction.

3-D reconstruction of the tomograms was achieved using a MATLAB-based reconstruction program. This program performs 2D characterization on slices obtained from the 3D scans of the sample volume. To demonstrate these capabilities, a flow chart of the

TABLE 3.2: Beamline parameters of 05ID-2 - SOE-1

Source	Superconducting (SC) Wiggler
Energy Range	$25 - 150keV$
Wavelength	$0.08 - 0.5$ Angstroms
Resolution $\Delta E/E@E$	$M_1CT : 10^{-3}$ and $M_4KES : 10^{-3}$
Beamline Length	55 m
Maximum Beam Size (Horizontal x Vertical)	220 mm 11 mm @ 55 m
Maximum sample-detector-distance	6 m

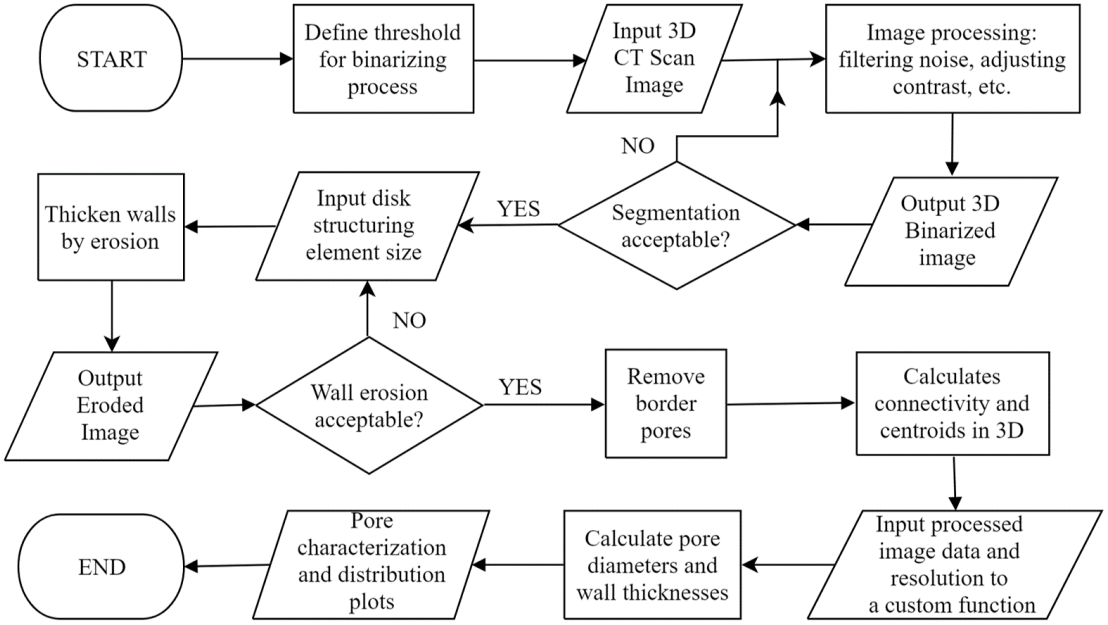

FIGURE 3.1: Flow chart of the MATLAB program used to reconstruct and analyze the Micro X-ray computed tomography scans of the polymeric foam specimen obtained from the Canadian Light Source.

image processing methodology adopted in this study is shown in Figure 3.1. Figure 3.2 shows a sample tomogram and sub-sequential image processing applied to it and is used to explain the flow chart in Figure 3.1. First, a threshold ranging from 0 to 1 is defined for converting greyscale images to binary images. The images are then converted to data type uint16 for better handling and processing, and to minimize loss of quality. The tomograms have varying contrast and brightness at different slices of the foam. The brightness is adjusted and the contrast is sharpened to obtain images with consistent lighting exposure to improve segmentation of distinct pores and walls. For example, the intensity of each pixel in greyscale images varies from 0 to 65535 for data type uint16, corresponding to black and white pixels, respectively. Depending on the amount of contrast in the original image, the threshold is varied manually to obtain the best result. For the tomograms obtained from CLS, the threshold was kept at a constant value of 0.34. Using the threshold, the adjusted and segmented image is converted to binary values.

Binarizing often results in the generation of additional noise and aliasing. Most of these unwanted features stand out because they are often small or large in terms of pixel area. They are filtered out by defining a range of pixel sizes to delete (pore sizes $< 25\mu m$ and wall thicknesses $> 50\mu m$). In the binarized images, walls have a value of 0, and the pores have a value of 1, and this is shown in Figure 3.2(b). Each slice is read and stored in a large 3D array for processing. Following this, a series of image processing operations are performed to segment the pores.

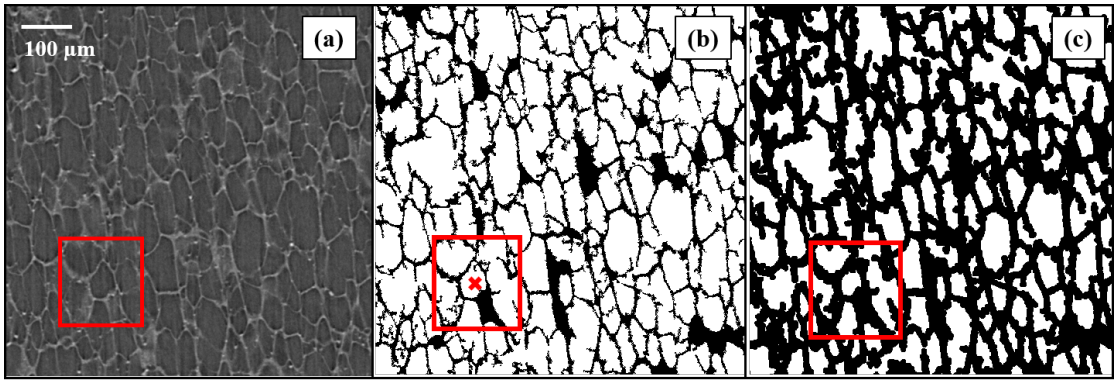

FIGURE 3.2: Segmented XCT image used to identify locations of throats (constrictions between two pores) within the sample, and for reconstruction. (a) Original XCT image with a specific pore of interest shown in the red box. (b) Binarized image after image segmentation with centroid. (c) Output eroded image showing thickened walls for closing off pores that opened up during binarization which is used to calculate pore centroids.

After image processing, the binarized image is stored in a 3D array. The segmented image is then visualized by plotting it and it is determined whether or not the image segmentation is acceptable. Parameters in the image processing step are varied until a desirable segmentation is obtained. Using the binarized 3D image, a disk structuring element is used to grow the pore size on the image in order to thicken the walls using a function called 'erosion'. The disk size was appropriately selected depending on the sizes of the pores for image erosion. Erosion is then implemented to close walls that may have been opened and filtered out during the image processing step. This process further minimizes the noise for improved data analysis. Similar to the output binarized image, the eroded image is visualized to determine if the erosion is appropriate as shown in Figure 3.2(c). After eroding the walls, the pores that are along the border of the scan are closed and filtered out. These regions are not of interest for data analysis since they are incomplete. The image without the border pores are stored in another variable. The eroded image without border pores are used to determine the pore sizes and wall thicknesses.

Using the output binarized images, the connectivity of pores in 3D is used to find the

connected regions in the images, and the coordinates of the 3D pore centroids are calculated. The coordinates of the pore centroids and resolution of the scan are input into a custom function that calculates the pore diameters and wall thicknesses. In this custom function, the pore diameters and wall thicknesses are calculated by counting the number of white and black pixels, respectively, in the positive and negative directions of three orthogonal vectors. The coordinates of the centroids are used as the starting point for all the pores. Corresponding to each centroid, 3 diameters (1 diameter in each x, y and z directions) and 6 wall thicknesses are calculated. These values are stored in a 3-D array for further data processing and plotting. For porosity measurements, the pore volume was calculated using the reconstructed XCT scans and was subtracted from the total sample scan volume. However, it is to be noted that porosity calculations were performed on the final segmented images from pore size measurements. Since different disk sizes were used to compute the segmented images for different strains, there is approximately 1% error in porosity calculations. Tomograms and MATLAB analysis of the pore size and wall thicknesses are shown next.

3.4 Experimental Results

In this section, the stress–temperature–strain plots, infrared images, XCT images, and microstructure data derived from tension and compression experiments are shown and discussed separately because of the differences in stress and temperature profiles observed for the different tension and compression stress states.

3.4.1 Quasistatic Tension Results

Three trials for tension were performed at the same nominal strain rate to verify repeatability of the material behavior. The stress-temperature-strain curves for quasistatic tension are shown in Figure 3.3. The x, y_1 and y_2 axes represent strain, stress (MPa) and temperature change ($^{\circ}C$), respectively, in a linear scale. The solid black curve (trial 1) is highlighted for clarity as this figure is later used to discuss temperature curves and microstructure changes, presented in a subsequent section. The dotted curves for trials 2 and 3 are shown for repeatability. In the quasistatic tension experiments, the yield stress was measured to be $0.57 \pm 0.20 MPa$ at a corresponding yield strain of 0.10 ± 0.04 across all samples. The elastic modulus in the corresponding strain range was measured to be $5.47 \pm 0.10 MPa$. In the inelastic deformation regime, the stress was found to linearly increase with strain at a rate of $0.44 \pm 0.05 MPa\epsilon^{-1}$. The inelastic deformation regime extends until a strain of 2.98 ± 0.07 is achieved, and no other notable features are observed on the stress-strain curve until failure. The failure strength and strain were

measured to be $1.99 \pm 0.05 MPa$ and 3.05 ± 0.05 across all samples, respectively. To observe the effects of black paint on the tensile response, one experiment was performed under similar experimental conditions with an unpainted specimen. This trial is represented by trial 3 (T3) in Figure 3.3 with a solid blue curve. As observed from the figure, there is no effect of the presence of black paint on the mechanical response.

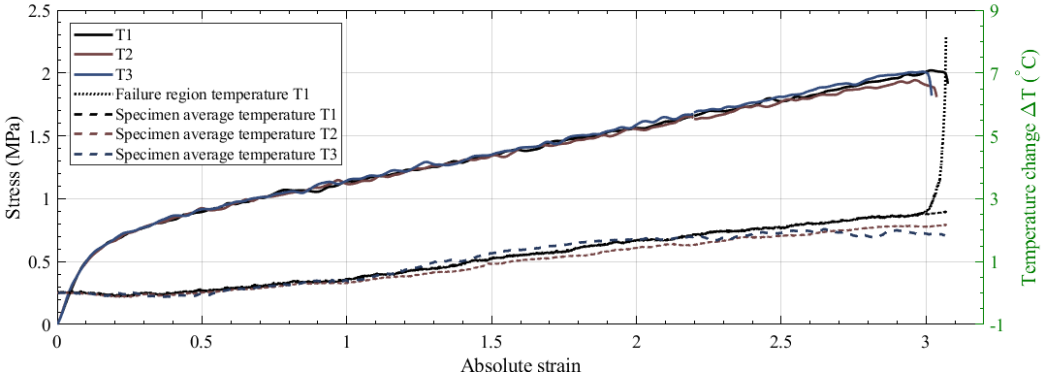

FIGURE 3.3: Figure showing Stress-Temperature-Strain ($y_1 - y_2 - x$) graph where black curve represents quasistatic tensile response of D3O LITE D foam. The black dashed curve represents average temperature measured across the entire gage section tracked through time. The black dotted curve represents temperature measured across the cross-section at localized region of failure tracked through time. The temperature of the sample is observed to uniformly increase with respect to strain until failure is initiated where a localized temperature increase of $\sim 8°C$ is observed.

3.4.1.1 Infrared Thermography Results

Shown in Figure 3.3 are the stress-temperature-strain curves of the tensile response of D3O LITE D. As noted earlier, the y_2 axis represents temperature changes observed on the specimen surface. To account for effects of atmospheric conditions, absolute temperature differences (ΔT) observed on the specimen surface are reported here (note the y-axis on the right side of the graph in Figure 3). The black dotted curve represents the temperature changes observed using a local ROI at the failure region. As observed from the curve, the temperature initially decreases by $\sim 0.05°C$ from 0 strain until a strain of ~ 0.25 is reached in the sample. Following this, the temperature continues to increase steadily at a rate of $1.02 \pm 0.05°C\epsilon^{-1}$ in the whole sample until failure. This drop and rise in temperature corresponds to the presence of an inflection on the curve at ~ 0.30 strain corresponding to the offset of the elastic regime. At a strain of ~ 3.0 at the region of failure, the temperature starts to increase rapidly at a rate of $90 \pm 5°C\epsilon^{-1}$ as the specimen starts to fail. A peak temperature rise of approximately $8°C$ is observed at the region of failure. The dashed black curve in Figure 3.3 represents the average specimen temperature changes observed using a large ROI over the specimen

cross section. A similar inflection is observed on the average specimen temperature curves as well, suggesting that the initial thermal response is globally similar throughout the sample. This can be corroborated from the figure where dashed and dotted black curves overlapping each other until a strain of 0.30 is reached in the specimen. Hereafter, the average temperature of the specimen continues to rise steadily at a rate of $1.02 \pm 0.05°C\epsilon^{-1}$ until failure. No notable features are observed on the temperature-strain curve until failure.

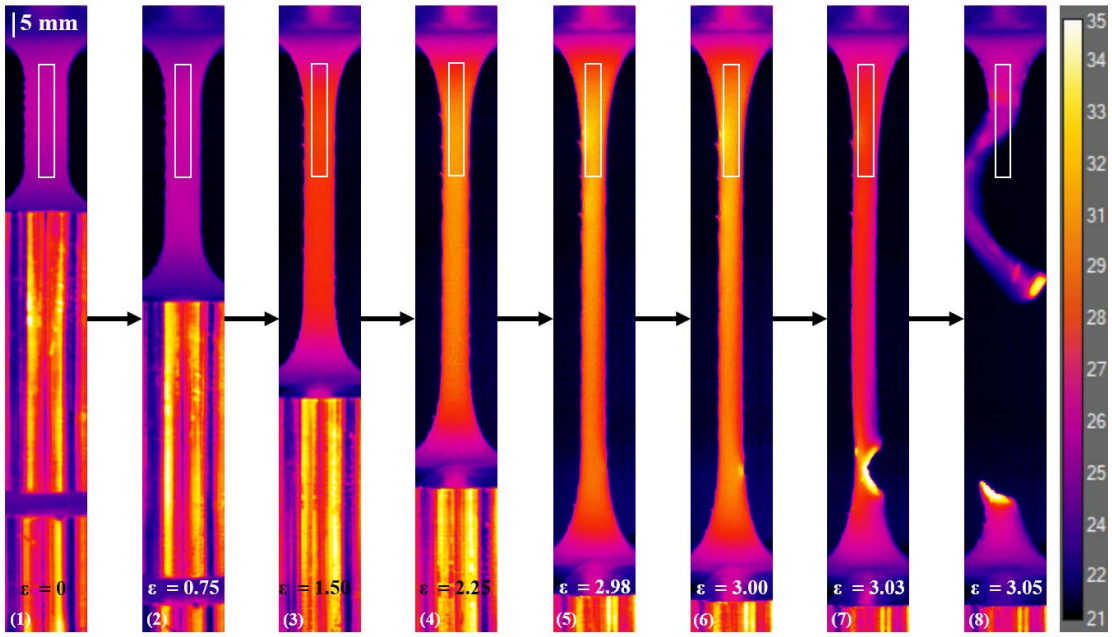

FIGURE 3.4: Thermal camera images from the quasistatic tension experiment at a strain rate of $0.1s^{-1}$ obtained using FLIR X8503sc imaging at 100Hz. Inter-frame strains and specimen lengths are denoted. Color bar on the right denotes temperature scale in Celsius. The last three images emphasize localized temperature increase that is observed at the failure region at a failure strain of 3.05.

Next, the global temperature measurements on the surface of a specimen are considered by examining individual images from the infrared camera. Figure 4 shows the infrared camera frames from one of the quasistatic tension experiments obtained using the FLIR X8503sc infrared camera filming at a framerate of 100Hz. Note the color bar on the right is in Celsius. Conforming to positioning of the camera and using a fixed ROI for the entire course of the event, a small ROI was selected as visualized in image (1) of Figure 3.4 which shows the pristine test sample. The dashed black curve in the temperature-strain axes shown previously in Figure 3.3 represents the average specimen temperature changes observed using the selected ROI over the specimen gage section. As seen from image (3) in Figure 3.4, at strains < 1.50 an appreciable amount of the surface area of the entire gage section is under observation within the ROI, but as strain increases, a large considerable area remains outside the fixed ROI. At strains higher

than 1.50, the specimen elongates in such a way that the gripped area of the dog bone specimen starts to appear inside the selected ROI. This presence of the extra area (which is not part of the gage section) reduces the measured rate of temperature increase as the gripped area does not contribute to the thermal measurements. This effect increases with increasing strain, and at strains higher than 2.25 the measured temperature plateaus until failure as seen in images (4) and (5) in Figure 3.4. It is to be noted that small changes in emissivity and surface condition occur during tensile testing and the errors caused by these effects are minute when compared to the overall temperature rise. At the onset of failure, the failure zone initiates at a point on the specimen perimeter as seen in image (6) in Figure 3.4, and failure propagates at $\sim 0.05m/s$ through the sample leading to complete tearing. Here, indirect measures of the thermal spikes are used to determine the supposed failure initiation/propagation and visualize the phenomenon through a thermal camera. The uncertainties associated with the ROI selection and corresponding temperature measurements were found to be less than 1%. This was found from temperature measurements using different size and shape ROIs on multiple locations on the sample surface.

3.4.1.2 Microstructure Results

Shown in Figure 3.5 is a composite figure of XCT images showing the evolution of microstructure in quasistatic tension. Note the loading direction is in the y direction. These images are obtained through XCT slices of the samples' center starting from 0.10 strain, at increments of 0.20 strain until a strain of 1. Image (1) shows the scan orientation of the specimens, where it can be observed from image (1) that there are irregularly shaped pores [25]. Some form of additives also appear to be concentrated at the pore boundaries which are visualized by small white dots in the XCT images [25]. Images (2) to (6) in Figure 3.5 show the differences in microstructure observed with increase in strain. There are no signs of permanent damage or pore elongation observed in image (2) as the pores remain intact. Signs of damage to the cell walls are observed in image (3) and they become increasingly prominent in images (4) to (6). Pore elongation and cell wall stretching also become more visually apparent in images (4) to (6).

Next, effects of mechanical loading on the evolution of pore size and wall thickness in these foam materials is explored. The procedure for determining the pore size and wall thickness measurements were discussed earlier. Note, it is recognized that foam samples recover up to $\sim$ 20% of the applied strain following tension testing, however, as will be shown, insights can still be gained as to what pore size length scales are activated during deformation. Pores with sizes less than $250\mu m$ were considered for pore size measurements based on visual confirmation from XCT scans. Now that different

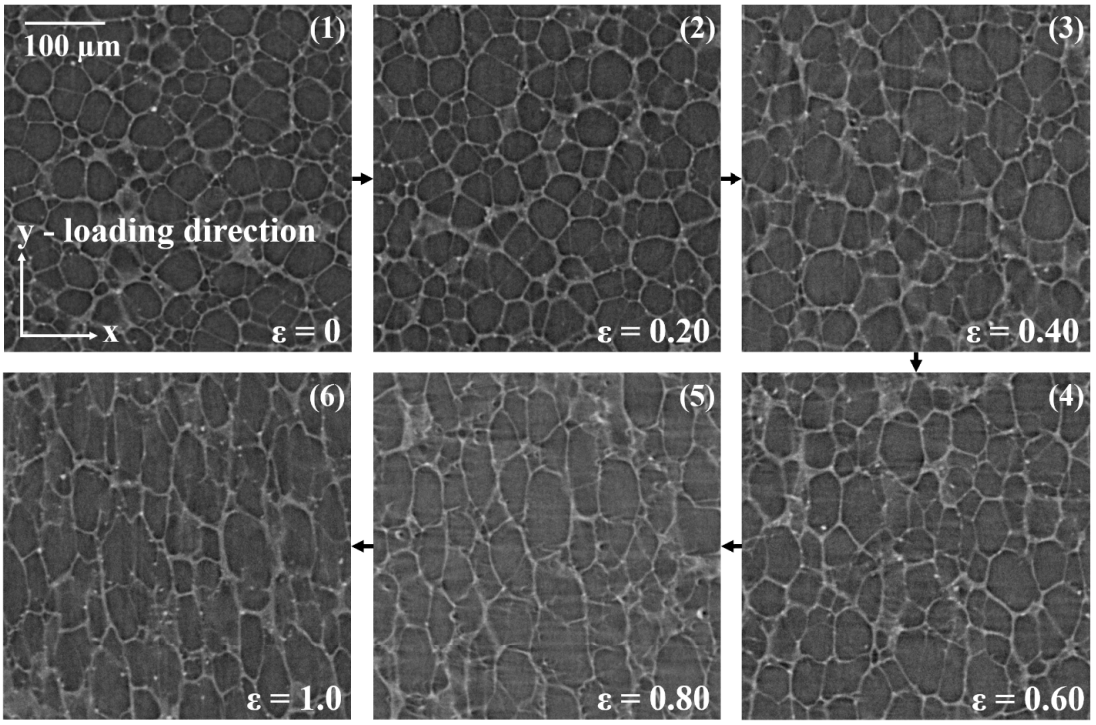

FIGURE 3.5: Composite figure showing microstructure evolution in quasistatic tension through XCT images of the sample center at increments of 0.20 strain until 1.0 strain. Visibly distinguishable differences in pore sizes are observed from strains greater for 0.20. Micro-tearing and damage of the cell walls is also observed for strains greater than 0.20.

characteristics of the pore size measurements have been identified, the effect of tensile loading on pore sizes is examined next in Figure 6. Here, the cumulative distribution of pore size in both x and y directions is plotted. The cumulative distribution is defined as:

$$G(x) = \int_0^x g(\bar{x})d\bar{x} \tag{3.2}$$

where $g(x)$ is the probability distribution of pore sizes. The pore size data set is a discrete set of n pores with sizes of $l_i(i = 1...n)$. Ordering this data for increasing pore size, and assigning a probability of $1/n$ to each pore, the normalized empirical cumulative distribution function, or eCDF, can be computed as the sum of these probabilities:

$$G_e(l) = \frac{1}{n}\sum_{i=1}^{n} I(l_i \leq l) \tag{3.3}$$

where the indicator function I has a value of 1 if $l_i \leq l$ and 0 otherwise. For each tomography scan, a total of $\sim 70,000$ pores were considered for size and thickness measurements. Shown in Figure 3.6 are the eCDFs which are used to identify the likely range of the pore sizes and trends. This is achieved by looking at the values between the 10th and 90th percentiles. This range is projected to be between $40\mu m$ and $120\mu m$ in both x and y directions for a pristine sample (pristine is labelled as 0 strain in Figure 3.6). In Figure 3.6, D_x and D_y represent the pore sizes in x and y directions, respectively. With increasing strain up to 0.3, a behaviorial trend is observed among the curves that smaller pores tend to elongate in both x and y directions while larger pores tend to contract in both directions. For strains greater than 0.3, the pore size distribution follows a constant and an expected trend [12, 16] where all pore sizes reduce in the x direction and increase in the y (loading) direction with increasing strain. From Figure 3.6, when the specimen is loaded in tension at a initial strain range of 0-0.7, it is observed that pores sizes of $D \sim 100\mu m$ show larger changes in the x direction when compared to the y direction. This is because smaller pores get stretched and coalese to form larger pores, thus increasing the number of pores that are greater than $100\mu m$. At strains greater than 0.7, the differences in pore sizes with $D > 100\mu m$ becomes more prominent and this can be visualized by the 0.9 and 1.0 strain curves having bigger pore diameters than other strains. For the 0.9 and 1.0 strain curves, there are also a greater number of larger pores possibly due to tearing and ripping of walls of small pores, resulting in coalescence into bigger pores.

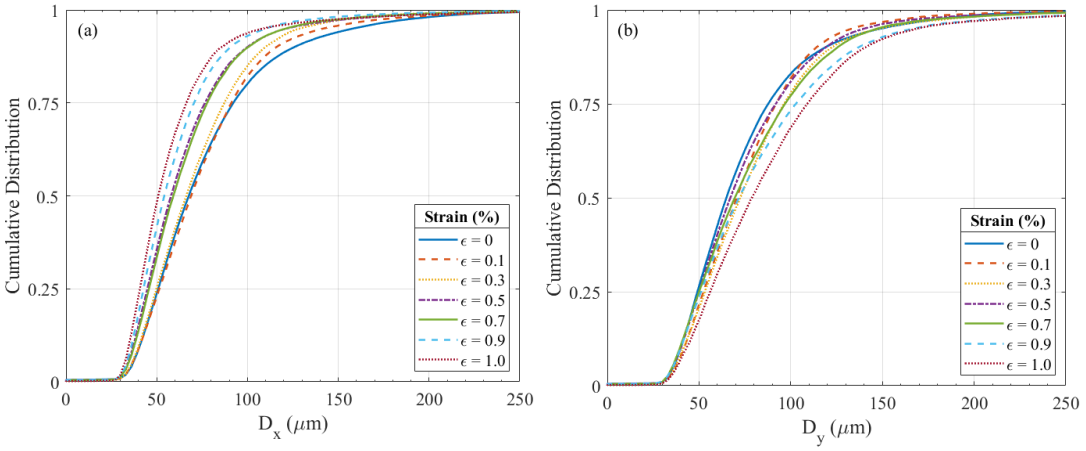

FIGURE 3.6: Emperical Cumulative Distribution Function (eCDF) plots of pore sizes shown for strain increments of 0.1 until $\epsilon = 1$ for quasistatic tension of D3O LITE D foam for both x and y directions. The $\epsilon = 0$ curves in both (a) and (b) represent the pristine sample.

Shown in Figure 3.7 are the eCDFs of the wall thicknesses for strains of 0 to 1.0. Wall thickness sizes less than 50m were considered based on visual confirmation from XCT

images. In Figure 7, t_x and t_y represent the wall thicknesses in x and y directions, respectively. The wall thickness range is projected to be between $3\mu m$ and $30\mu m$ in both x and y directions for a pristine sample. Profiles of t_x and t_y are similar. For all samples, it is consistent that t_x is less than t_y as strain in the y direction increases. When compared across samples, both t_x and t_y decreases as strain increases. This trend is followed consistently throughout for t_x. For t_y, it generally follows a similar trend but with slight variations. t_y for a pristine sample is different from the other strains. Also, there is another effect that makes t_y smaller as strain increases. This is possibly due to tearing of walls and making thicker walls thinner through plastic deformation. Although relative differences between these values are small, these variations in wall thickness evolution as a function on increasing strain are to be noted.

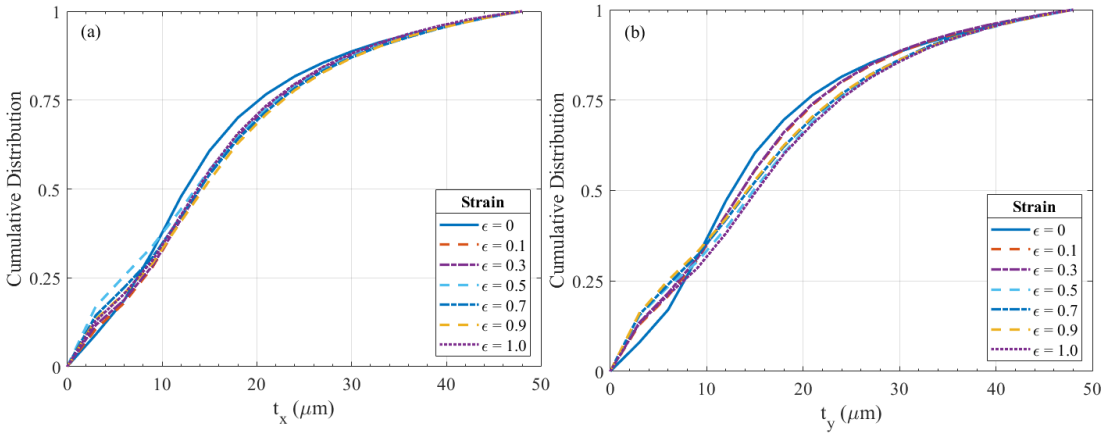

FIGURE 3.7: Cumulative Distribution Function (eCDF) plots of wall thickness shown for strain increments of 0.10 until 1.0 strain for quasistatic tension of D3O LITE D foam for both x (a) and y (b) directions. The $\epsilon = 0$ curves in both (a) and (b) represent the pristine sample.

To better understand the evolution of microstructure during the quasistatic tensile response of this D3O LITE D foam, all quantitative microstructure data is consolidated and presented in the form of percentile plots for both pores sizes and wall thickness variations in Figure 8. The percentile plots are obtained from the CDF function for G(x)=0.1, 0.25, 0.5, 0.75 and 0.90 (e.g. G(x) = 0.1 is the tenth percentile). The presentation of the data in percentiles is done to help clarify trends observed in the cumulative distribution plots. In Figure 3.8(a), the x and y axes represent pore size (μm) and strain, respectively, and wall thickness (μm) and strain, respectively in Figure 3.8(b). A single color scheme is used for both pore size and wall thickness percentile curves, and are denoted by $x - P_i$ and $y - P_i$ in the common legend at the top of the figure, where the percentiles are P_i where i represents the strain percentage. In both subplots, porosity is plotted as a function of strain which gives more basis of discussion.

First shown in Figure 3.8(a) are the percentile plots corresponding to the pore size eCDFs in Figure 3.6. At strains of less than 0.2, the trend is clearly observed that smaller pores tend to deform first and they deform equally in both x and y directions. This results in a sudden decrease in porosity. As strain increases greater than 0.2, it is observed that pores of all sizes show expected behavior that sizes increase in the y direction and decrease in the x direction. This results in a near constant rate of increase in porosity of the material as shown in Figure 3.8(a). From Figure 3.8(a), it is also observed that the number of pores with size $< 100\mu m$ are smaller for higher strains than the pristine sample. This is consistent with the previous statement that as smaller pores gets stretched, there will be fewer of the small pores. Shown in Figure 3.8(b) is the percentile plots for the wall thicknesses in both x and y directions. Again, we discuss percentiles of G(x)=0.1 ,0.25, 0.5, 0.75 and 0.9. In summary, it is observed that there is no effect of tensile loading on evolution of wall thicknesses throughout the strain range. This implies that the stress response is primarily governed by geometry change of the pore structure. Generally, with increase in strain, the trend of the observed microstructural length scales tend to follow a very slight linearly increasing path until onset of failure occurs. Finally, as noted before, bigger pores are more susceptible for larger pore size variations and this is true until the onset of localization is observed.

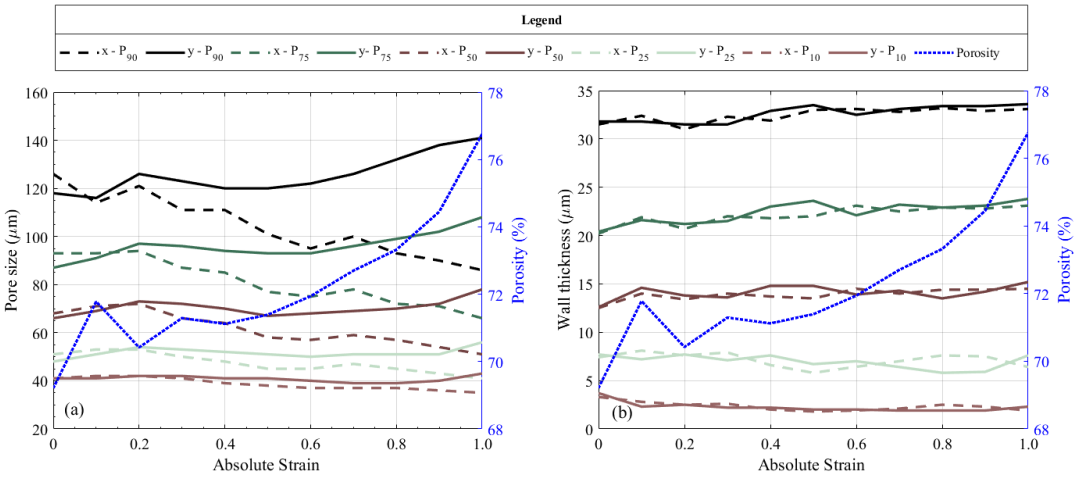

FIGURE 3.8: Compiled percentile plots of (a) pore size and (b) wall thickness shown for 10th, 25th, 50th, 75th and 90th percentile in both x and y directions for quasistatic tension of D3O LITE D foam. Plot also shows evolution of porosity with strain.

3.4.2 Quasistatic Compression

Next, the stress-temperature-strain curves for quasistatic compression are shown in Figure 3.9. The x, y_1, and y_2 axes represent strain, stress (MPa) and temperature change ($^{\circ}C$), respectively. The solid curves represent the stress-strain responses for the three

different trials and the dotted curves represent the temperature-strain profiles for the corresponding experiments. In the quasistatic compression experiments, the elastic modulus was measured to be $2.5 \pm 0.2MPa$. For this partially open/ partially closed cell foam material, the end of the linear-elastic regime was not clearly identifiable and a gradual transition was found from the elastic to plateau regime beginning in a strain range of $0.02 - 0.06$ strain, which does not yield a specific value of the elastic collapse stress σ^*_{el}. Therefore, an average stress over the specified strain range of 0.042 – 0.056 was calculated, and σ^*_{el} was measured to be $0.130 \pm 0.016MPa$. The stress-strain curve then starts to plateau at a strain of ~ 0.06 and a stress of $\sim 0.155MPa$, indicating the start of the elastic collapse regime. From this point, the sample continues to harden with a constant hardening rate of $0.93 \pm 0.20MPa$ until a strain of ~ 0.5 is reached. The sample then begins to slowly densify starting at a strain of ~ 0.7 at an increasing rate until a strain of 0.83 ± 0.03 is reached in the sample, at which point the sample starts to densify rapidly, corresponding to complete pore collapse. It is also observed that there was a small increase in the hardening rate followed by a gradual decrease at this 0.83 ± 0.03 strain and further loading the sample leads to near-complete densification in the material.

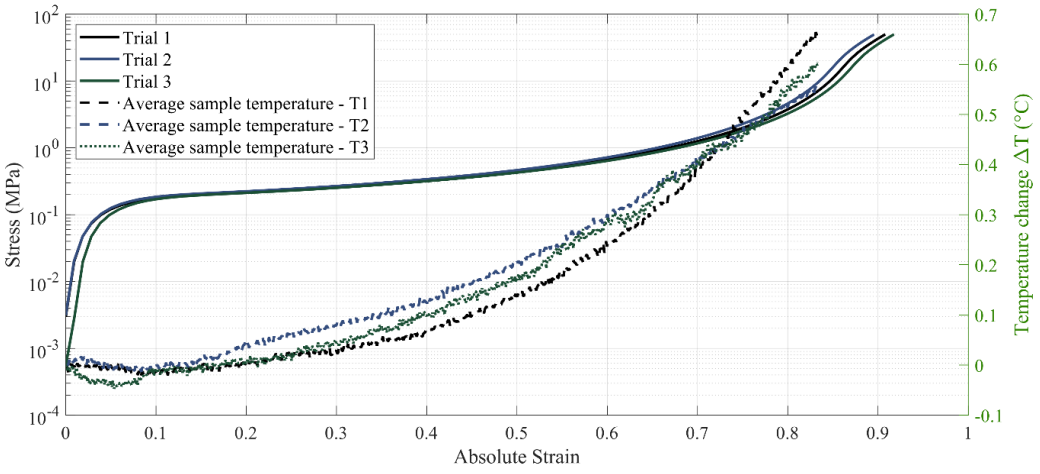

FIGURE 3.9: Figure showing Stress-Temperature-Strain ($y_1 - y_2 - x$) graph of quasistatic compressive response of D3O LITE D foam. The solid curves represent the stress-strain profiles and the dotted curves represent the strain-temperature profiles of average temperature measured across the sample surface for the corresponding trials. The temperature of the sample is observed to increase with respect to strain and an average temperature increase of $\sim 0.65°C$ is observed at a strain of ~ 0.83.

3.4.2.1 Infrared Thermography Results

Shown in Figure 3.9 are the temperature-strain curves taken from compression experiments of D3O LITE D, represented by the dotted curves. As noted earlier, the y_2 axis on the right represents temperature changes and it is noted that absolute temperature

differences (ΔT) observed on the specimen surface are reported here. As observed from the curves, the temperature initially decreases by $\sim 0.03 \pm 0.01°C$ from 0 strain until a strain of ~ 0.05 is reached in the sample. This drop and rise in temperature corresponds to the presence of an inflection on the stress-strain curve at a strain of ~ 0.05, corresponding to the offset of the elastic regime. As observed from the curves, the average temperature in the sample then increases with a gradually increasing slope through all the stress regimes. Specifically, the temperature continues to increase in a parabolic fashion with respect to strain and an average temperature increase of $\sim 0.65°C$ is observed at a strain of ~ 0.83.

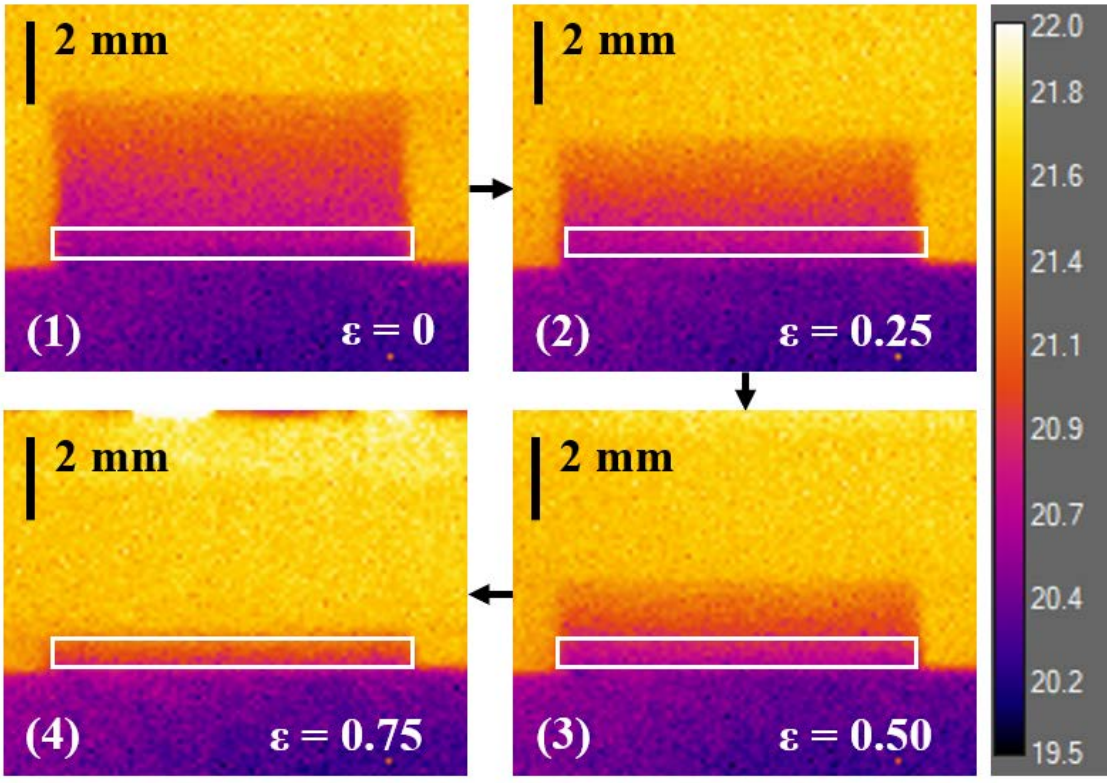

FIGURE 3.10: Thermal camera video images from the quasistatic compression experiment at a strain rate of $0.1s^{-1}$ obtained using FLIR X8503sc at 100Hz. Inter-frame strains and specimen lengths are denoted. Color bar on the right denotes temperature scale in Celsius. The white box represents the region of interest over which temperature measurements are averaged.

Shown in Figure 3.10 is a series of infrared video frames from one of the quasistatic compression experiments obtained using the FLIR X8503sc infrared camera filming at a framerate of 100Hz. Note the color bar on the right is in Celsius. A fixed ROI was chosen for the entire course of the event, as visualized by the white rectangular boxes in the images. The relative temperature difference between the top and bottom compression platens was measured to be $\sim 0.75°C$ and this can be visualized as a temperature gradient across the sample in image (1) of Figure 10. Similar gradients were observed

for the other compression experiments. From images (2) and (3), it is observed that the average temperature of the whole sample increases gradually with increasing strain. As the strain increases, the overall temperature distribution in the sample becomes more uniform as visualized in image (4). At higher strains in the densification regime in image (4), the pixels available through the thickness are reduced, limiting the temperature measurements up to ~ 0.83 strain. The uncertainties associated with the ROI selection during compression testing and corresponding temperature measurements were found to be approximately 2.5%. This was found from temperature measurements using different size and shape ROIs on multiple locations on the sample surface and over all samples.

3.4.2.2 Microstructure Results

Shown in Figure 3.11 is a composite of XCT images showing the evolution of microstructure in D3O LITE D foam in quasistatic compression. Note the loading direction is in the y direction. These images are obtained by taking XCT slices of the samples' center starting from 0.1 strain, at increments of 0.2 strain until 0.9 strain. Image (1) shows the pristine sample and also shows the scan orientation of the specimens. Images (2) to (5) show the differences in microstructure observed with increasing strain up to 0.7. As seen, there are no signs of permanent damage and the pores remain intact. Image (6) shows the recovered microstructure at a strain of 0.9, which corresponds to the post densification regime, and in the image signs of damage to the cell walls are observed as a result of complete pore collapse. The quantitative measurements of pore sizes as a function of strain are explored next.

Shown in Figure 3.12 are the eCDFs which are used to identify the trends of pore size evolution in quasistatic compression. D_x and D_y represent the pore sizes in x and y directions, respectively. As seen from the figure, the differences in pore sizes for strains less than 0.7 are relatively small, and it noticed that most strains are overlapping with the 0 strain pristine curve, indicating that they have recovered their sizes. It is observed that mid-range pore sizes between $80-150\mu m$ are most susceptible to permanent deformation. It is inferred that this strain recovery occurs non uniformly for the x and y directions as no clear trends are observed in the pore size distribution. From the blue dashed curves shown for 0.9 strain, it is observed that post densification, the pore sizes are not recovered completely and this is seen from the curve shifting to the left in the cumuluative distribution for D_y. This indicates pore squishing in the loading direction, and the blue dashed curve shifting to the right in the cumuluative distribution for D_x indicates permanent expansion in the lateral direction. Similar to the tensile loading case, no differences in wall thicknesses were observed with increasing strains, and hence eCDFs for wall thicknesses are not shown. Since no clear trends are observed for the

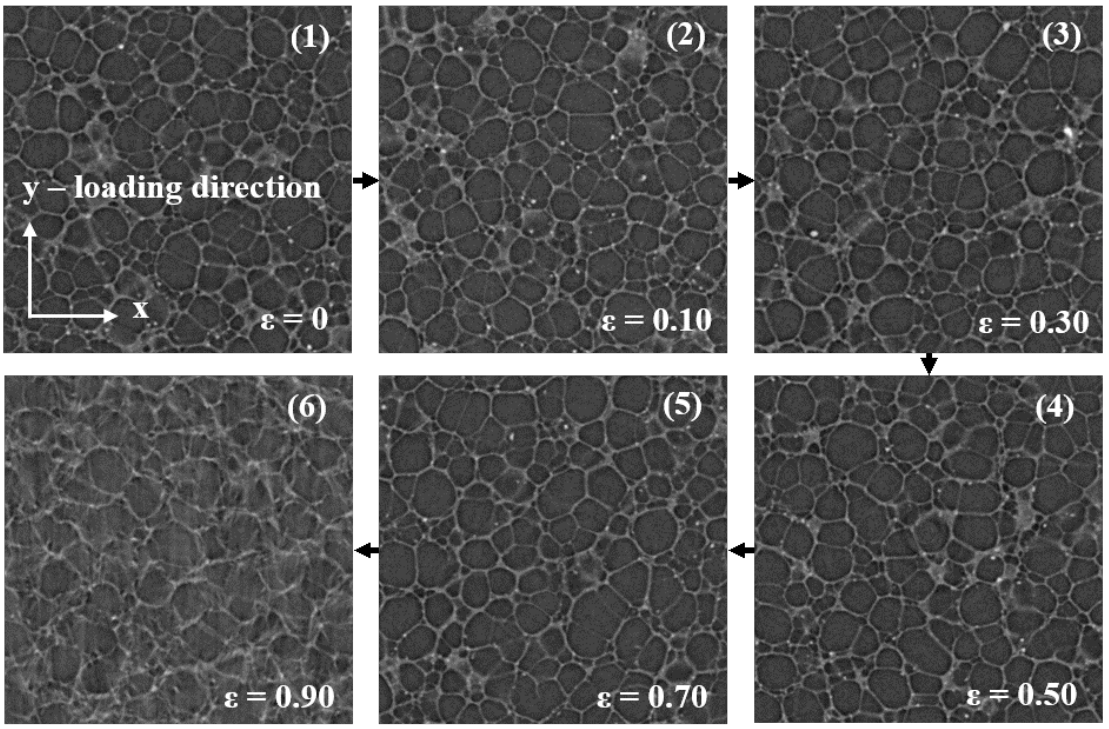

FIGURE 3.11: Composite figure showing microstructure evolution in quasistatic compression through XCT images of the sample center at increments of 0.2 strain until a strain of 0.9. Relative differences in pore sizes are not observed in images (1) to (5) up to a strain of 0.7. Ruptured cell walls and damaged pore structures are observed in image (6), corresponding to a strain of 0.9.

evolution of both pore size and wall thickness in the quasistatic compressive loading case, the percentile plots are also not shown.

3.5 Discussion

This paper investigated the thermo-mechanical behavior and microstructure evolution during quasistatic tensile and compressive failure of a shear-thickening polymeric foam. It is important to have a better understanding of the behavior of these materials since this class of foams are currently being employed in energy absorption equipment (e.g., helmet liners for Football, Baseball and Ice Hockey; inserts for Motorcycle jackets) and military applications [90, 97]. Limited data on the foams in this study, and shear-thickening foams in general, exist in the literature, and so this paper seeks to make contributions towards better understanding how microstructural features and thermal response of these types of foams may be related to quasistatic response and how the quasistatic response may differ from a typical polymeric foam. In what follows, the authors discuss the results of behavior of this foam in the context of their general understanding of how polymeric

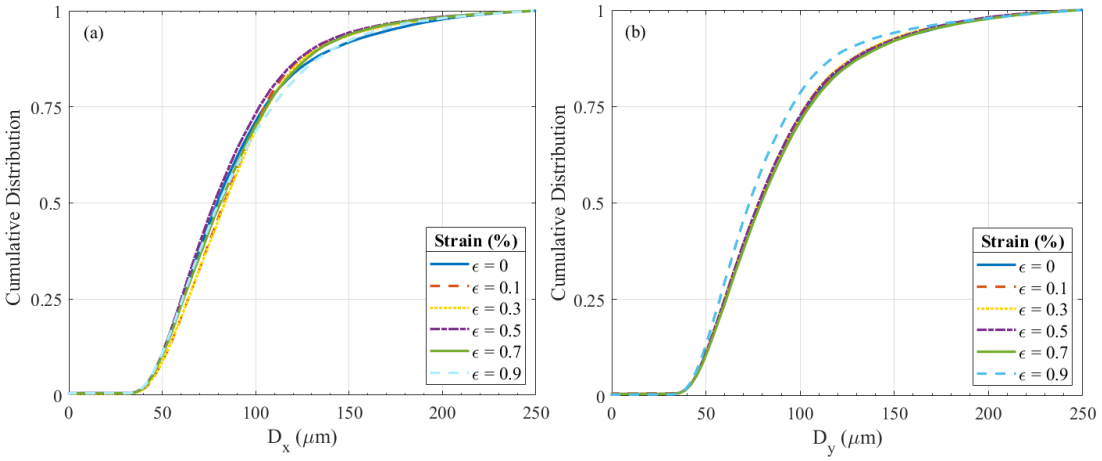

FIGURE 3.12: Cumulative Distribution Function (CDF) plots of pore sizes shown for strain increments of 0.10 until 0.90 for quasistatic compression of D3O LITE D foam for both x (a) and y (b) directions. The $\epsilon = 0$ curves in both (a) and (b) represent the pristine sample.

foams behave in quasistatic tensile and compressive loading, highlighting our key results where necessary. The results obtained through infrared thermography and mechanical measurements, as well as qualitative and quantitative data obtained from XCT provide the basis for this discussion. First, each regime in the stress-strain curves in Figures 3 and 9 are discussed in greater detail with the help of microstructure data, temperature-strain curves, and infrared camera images.

3.5.1 Quasistatic Tension

The first part of the tensile stress-strain curve is the elastic regime, which represents strains less than 0.08 ± 0.04 for D3O LITE D. The tensile elastic modulus for the D3O LITE D is found to be $5.47 \pm 0.10 MPa$. For polymeric foams, the linear-elastic strain limit is found to be different for different foam materials throughout literature [11, 12, 16]. Comparing similar density foams as the D3O LITE D for quasistatic tensile loading, Walter et al.[11] report an elastic strain in the range of 0.03 ± 0.02 with an elastic modulus of $\sim 226 MPa$ for a $200 kg/m^3$ density PVC foam. Zenkert et al.[12] found elastic strains less than 0.02 with an elastic modulus of 395 MPa for a $205 kg/m^3$ density PMI foam. In another study, Kabir et al.[16] measure an elastic strain of 0.04 ± 0.01 with an elastic modulus of $\sim 140 MPa$ for a $240 kg/m^3$ density polyurethane foam material.

Limited data exists on the thermal response of foams in the literature. For the D3O LITE D material studied here, it is observed that the average temperature of the sample initially decreases by $\sim 0.05°C$ over ~ 0.25 strain, which corresponds to the end of the elastic regime of the material. The surface temperature decrease under uniaxial tension

within the elastic strain limits and is caused due to the thermoelastic effect, which is well described in existing literature [98, 99]. In any deforming structure with a positive coefficient of thermal expansion, the strain field causes a change in the internal energy of the specimen such that compressed region becomes hotter and the expanded region becomes cooler and the mechanism responsible for thermoelastic effect is the lack of thermal equilibrium between various parts of the deforming structure. Considering the energy and entropy balance equations during tensile loading, in theory it is assumed that there is no additional work other than the elastic stretching and that the volume of the material does not change in the elastic regime and the length change is compensated for by the change in cross-sectional area [98]. In the infrared images, no notable features are visible on the surface and temperature is uniformly distributed across the surface in the elastic regime. From the wall thickness measurements, the 0.50 strain curve show the highest cumulative distribution between tx for thickness $< 10\mu m$, and this strain of 0.50 corresponds to the end of the linear elastic regime, and at this stage, to compensate for thermoelastic effects, the relative increase in length is compensated by volume change [98]. From the XCT data, it is visualized in images (1-2) of Figure 3.5 that larger pores remain the same sizes and there is no visible damage to the microstructure in the elastic regime (strains $< 0.10 \pm 0.04$). In this range of strain, it is observed from Figure 3.8(a) that all pore sizes do not undergo deformation, but there is a slight increase in the porosity. This is believed to be caused due to relative differences in permanent elongation/contraction being experienced by the different pore sizes as seen in Figures 3.6 and 3.8.

Following the elastic regime is the inelastic plateau regime. Over the inelastic deformation regime, the stress in the sample rises linearly with strain at a rate of $0.44 \pm 0.05 MPa\epsilon^{-1}$ over 0.3 to 2.98 ± 0.07 range of strain. The yield stress for the D3O LITE D material was found to be $0.57 \pm 0.20 MPa$. Comparing similar density foams as the D3O LITE D, Zenkert et al. [12] measure a yield stress of $\sim 6.45 MPa$ for a $205 kg/m^3$ density PMI foam, and Kabir et al. [16] measure a yield stress of $3.60 \pm 0.10 MPa$ for a $240 kg/m^3$ density polyurethane foam material. It is to be noted that elastomeric foams can undergo higher strains than those experienced before the linear-elastic strain limit and the deformation can still be mostly recoverable, but is non-linear [22]. After a strain of 0.20 ± 0.05 is reached in the specimen, there is an inflection in the temperature curve at roughly the point in the stress-strain curve that corresponds to the post-elastic part. The temperature starts to increase beyond a strain of 0.30 ± 0.05 resulting from thermal energy release in the process of micro-tearing of the cell walls. Over this entire range of strain, an average temperature rise of 2 degrees is observed within the specimen at the end of the inelastic regime. In XCT images (3-6) of Figure 3.5, it can be observed that with increasing strain in the y direction, pore sizes show visually observable differences

in sizes. For strains greater than 0.30, it can also be observed from the images that pore boundaries and walls show signs of damage and permanent deformation. Throughout the inelastic regime, the porosity is observed to linearly increase at a rate of $0.075\%\epsilon^{-1}$ until failure.

Prior to complete tearing and failure, the pre-failure regime as defined by the initiation of tearing starts at a strain of 2.98 ± 0.07 for D3O LITE D. The ultimate tensile strength was measured to be $1.99 \pm 0.05 MPa$ and the failure strain was measured to be 3.05 ± 0.05 across all samples. Prior to failure, minor fluctuations in temperature are observed and this is likely due to the result of localization because of pore tearing. At the begining of the pre-failure regime, a local heat zone is observed in image 6 of Figure 4 which indicates local failure being initiated within the sample. This heat spot results from energy release in the course of the breaking of chemical bonds during failure [99]. At the onset of failure, the failure zone initiates at a point on the specimen perimeter and failure propagates at $\sim 0.05 m/s$ through the sample leading to complete tearing. In Figure 3, the dotted black curve shows the temperature measured across the region of failure. In the local failure region, there is a sharp rise in temperature by $\sim 8°C$ degrees observed at the point of failure at a strain of 3.05 ± 0.05.

3.5.2 Quasistatic Compression

In this sub-section, commonly known deformation mechanisms in polymeric foams are correlated to the stress-strain response of our D3O LITE D foam in quasi-static compression loading (Figure 3.9). Generally, three different phases of deformation are observed during compressive loading of polymeric foams [84, 100]. The first is the linear-elastic regime, where the stress is directly proportional to the strain response following Hooke's law and the elastic strain is completely recoverable. For typical polymeric foams, the linear-elastic limit is limited to small strains less than 0.05 [84]. During elastic loading, all stresses are carried by only the cell walls that show small regions of buckling which directly contribute towards the stiffness of the material [71]. The complete pore recovery in the elastic regime is depicted by image (2) in Figure 3.11, and the orange dashed curves shown in Figure 3.12. Although these curves represent the recovered microstructure for a 0.10 strained sample, it is observed that even in the post-elastic limit, even higher strains are fully recoverable as the orange dashed curves lie on top of the solid blue curves shown for the pristine sample. In the D3O LITE D material, the linear elastic regime extends to $\sim 0.01 - 0.015$ strain. Comparing other foam materials with similar density as the D3O LITE D foam for quasistatic compressive loading, Walter et al.[11] report elastic strains less than 0.03 with an elastic modulus of $\sim 145 MPa$ for a $200 kg/m^3$ density PVC foam. In another study, Zenkert et al. [12] found elastic strains

less than 0.02 with an elastic modulus of $395MPa$ for a $205kg/m3$ density PMI foam. Comparing these results with tension, it is found that the PMI foams used by Zenkert et al. [12] show a symmetric behavior in both tension and compression. Similar to tensile behavior, the thermoelastic effect is also observed in the elastic regime in the thermal response of the quasistatic compression of D3O LITE D foam.

The second phase is the plateau regime characterized by non-linear elasticity, where the foam material continues to plateau at a relatively constant stress, known as the plastic collapse stress σ^*_{pl}. Plastic collapse typically gives a long, approximately horizontal, plateau to the stress response in the material. This property of polymeric foams is often exploited for energy-absorbing applications [17, 18, 84]. For the D3O LITE D material, the plateau behavior begins at around 0.06 ± 0.01 strain and deformation is dominated by buckling of cell walls [71]. This mechanism spans the entire inelastic regime. Under compressive loading, polymeric foams can undergo higher strains than the elastic limit and the deformation can still be mostly recoverable, but is non-linear [82]. This phenomenon is observed for the D3O LITE D material as well, and is depicted by the XCT images (2)-(5) in Figure 3.11 showing pore size recovery, and the curves representing strains from $0.30 - 0.70$ in Figure 3.12 showing similar pore size trends. These curves also show uneven variations in pore relaxation, indicating that permanent bending of cell walls likely begins only at the later stages of the plateau regime, almost nearing densification. The collapse stress for D3O LITE D in quasistatic compression is found to be $0.155MPa$. For other foams with similar densities, the collapse stress has been observed to be $5.97MPa$ for a $200kg/m^3$ density PVC foam [11] and $6.45MPa$ for a $205kg/m^3$ density PMI foam [12], making D3O LITE D one order of magnitude weaker when compared to these materials.

The third and final phase of compressive deformation is called densification, where the foam begins to respond like a compacted solid [7, 17, 70]. After initial densification, complete pore collapse is observed. For the D3O LITE D material, there was an inflection at the stress-strain curve around 0.83 ± 0.03 strain and stress of $6.45 \pm 0.12MPa$ (Figure 3.9), and it is believed that is likely related to complete pore collapse. In other studies in the literature, variation in densification strains has been shown between different materials and this range is often reported to start at strains greater than 0.50 [1, 7, 12, 25, 70]. After complete pore collapse, at these high strains, the opposing cell walls crush together and cell wall material is itself compressed and complete densification is observed. Lastly, for the D3O LITE D material studied here, the average temperature of the sample was found to increase in a parabolic fashion without any deviation, starting at the end of the linear elastic regime, to the densification regime.

3.5.3 Implications for Modelling

Next, the modeling implications of the observations made in this study are explored, and discuss the necessity and advantages of including real microstructures in material models. In one study, Jarfelt et al. [101] measure pore sizes of different density foams to aid in thermal conductivity calculations of foam materials. They measured different cell gas contents to accurately calculate the radiation transmission coefficients. Although not implicitly stated, from the measurements in their study, it is observed that there is a linear relationship between carbon dioxide content and cell size, which has a direct effect on effective thermal conductivity measurements. In another study, Mills et al. [40] note the differences in microstructures with respect to closed-pore content, pore orientation and spacing, and pore size, and relate these parameters to foam manufacturing processes. In some models in the literature, it is also observed that micro-mechanical models based on idealized foam microstructures of either an ordered or random network [102] of pores may not always reflect the experimentally determined values accurately in one particular loading direction. Further, it is to be noted that the structural response of foams is strongly influenced by the cell geometry (cell topology, foam density and anisotropy ratio) and by properties of the base polymer material [40]. Existing research on open-cell foams have also considered a wide range of pore microstructures, including polyhedrons, truncated octahedrons and rhombic dodecahedrons [102]. Many studies [9, 17, 36, 40, 102, 103] note a necessity of including these length scales in the constitutive models to better predict material response. This can be achieved by generating unit cells based on statistics of real microstructural parameters of foams such as closed-pore content, pore size and wall thickness, and the pore orientation and spacing. One of the identified contributions of the present study is that the characterization techniques provided here can be employed directly, or improved upon, to identify such statistics of foam microstructures, enabling better micro-mechanical modeling. For example, the XCT data of foam can provide insights into the cell-by-cell deformation of the foam, which is hypothesized by Di Landro et al. [17], Mills et al. [9] and other microstructure-based models.

3.6 Conclusion

The thermo-mechanical quasistatic tensile and compressive response of a shear-thickening polymeric foam D3O LITE D is explored at a strain rate of $0.1s^{-1}$. Important microstructural parameters like pores sizes ($40\mu m$ to $120\mu m$) and wall thicknesses ($3\mu m$ to $30\mu m$) have been identified using Micro XCT and image processing techniques. Overall for the tensile stress state, pore sizes were found to increase linearly with increasing strain, and it was observed that bigger pores ($D > 100\mu m$) are more susceptible to greater changes

in size when strained when compared to smaller pores. The changes in wall thicknesses were comparatively negligible through the entire strain range (0 to 3.05 ± 0.05). For the compressive stress state, no clear trends in pore size evolution were observed and permanent damage was found to occur only after complete pore collapse at strains $> 0.83 \pm 0.03$. The thermal response of this foam during quasistatic testing was established using Infrared Thermography, and in tension, the average specimen temperature was found to increase by $\sim 3°C$ and concurrently a local temperature increase of $\sim 8°C$ was observed at the failure region over a strain of 3.05 ± 0.50. In compression, the temperature was found to gradually increase until densification. Altogether, these observations and discoveries made in this paper are supported by stress-strain curves, XCT images of original and evolving microstructure, pore size and wall thickness distributions, and high speed infrared thermography images. As this is the first time that the D3O LITE D foams have been characterized in this way, the authors believe these experimental results will also serve as a good starting point for impactful modeling [9, 17].

Chapter 4

Density, microstructure and strain-rate effects on the compressive response of polyurethane foams

Accepted to be published as **Kapil Bharadwaj B**; Meredith, C; Satapathy, S; Ouellet, S; Romanyk, D; and Hogan, JD. *Density, microstructure and strain-rate effects on response of polyurethane foams*, Experimental Mechanics (2021)

Author	**Contribution**
Kapil Bharadwaj B	Conceived the ideas and experimental design of the study; Performed experiments/data collection; Data analysis and interpretation; Primary author (drafted the manuscript)
Meredith, C	Performed experiments/data collection; Methods section - secondary author; Provided revisions to scientific content of manuscript
Satapathy, S	Provided revisions to scientific content of manuscript
Ouellet, S	Provided revisions to scientific content of manuscript
Romanyk, DL	Provided revisions to scientific content of manuscript; Provided access to crucial research equipment
Hogan, JD	Provided revisions to scientific content of manuscript; Provided stylistic/grammatical revisions to manuscript; Principal investigator

4.1 Abstract

A better understanding of the effect of density, microstructure, and strain-rate on the mechanical response of polymeric foam materials is needed to improve their performance. The objective of this paper is to study the combined influence of density, microstructure, and strain-rate on the compressive stress-strain response of polymeric foams. Microstructural morphological parameters (e.g., pores sizes and wall thicknesses) have been quantified using Micro X-ray tomography and MATLAB-based techniques. Polymeric foam samples were examined under uniaxial compression loading at quasistatic (0.001 to $0.1s^{-1}$), intermediate (1 to $250s^{-1}$), and dynamic strain rates (3200 to $5700s^{-1}$). All experiments were coupled with high speed cameras to measure strain using 2D digital image correlation, and to visualize deformation. The variation of the mechanical properties across all densities (e.g., elastic modulus and collapse stress) are found to behave in a power-law fashion with respect to strain rate. A comprehensive data set across a varied range of densities and strain rates, especially intermediate strain rates is lacking in previous research, and generalized phenomenological relationships developed in this paper to predict combined influences of density, microstructure, and strain-rate over varied range of materials are important contributions of this work. The results showed that the power-law relationships act as a good predictor for the prediction of mechanical properties and elastic response, and as an indicator for deformation mechanisms in these polymeric foams.

4.2 Introduction

Polymeric foam materials are used to mitigate energy transfer between objects during a varied range of events. These foams are used in a wide range of applications such as military [3, 4], aerospace [1–3], automotive [1, 2], and packaging applications [4]. Their low densities and energy absorbing capabilities make them an ideal candidate for usage as protection materials, such as in personal protection equipment (PPE) like helmet liner materials [4, 7] and knee pads [7]. In these applications, the foams are often subjected to severe loadings involving multi-axial stress states and dynamic strain rate loading conditions. By gaining a better understanding of the mechanical properties of polymeric foams, higher quality protective equipment materials may be manufactured.

Studies on the use of foams for protective applications have considered a variety of possible materials that could be used in dynamic environments, such as functionally graded foams (FGF)[104], micro-lattice structures[105], and single and bi−layered foams [24]. For example, Cui et al.[104] investigated the properties of FGFs and found that

they are more effective at absorbing energy at lower strain rates and are slightly less effective at high strain rates because the foam properties are dominated by the lowest density layers at high strain rates. In a separate study, Schaedler et al.[105] studied micro-lattice structures finding that their energy absorbing capabilities are higher at lower strain rates, although, further investigation is required for higher strain rates. In another study, Fitek et al.[24] compared the peak acceleration responses helmets with different foam liners of a range of densities from 32 to 80 kg/m^3. These foams were studied under both quasistatic and impact loading conditions, and acceleration responses were compared with finite element method (FEM) simulations to make quantitative comparison of compressive response between materials of different densities. From the results in these studies [24, 104, 105], it was observed that the relationship between density, strain rate, and mechanical strengths in these materials are not fully understood.

To characterize foam materials, some authors used energy absorption diagrams, which plots the amount of absorbed energy as a function of the transmitted load [18]. Other authors have investigated in more details the microstructure [17], density [10, 17] and strain rate [10, 17] [7, 22, 49, 106], effects on mechanical properties. In their study, Saha et al.[10] discuss the behavior of closed-cell polyurethane and polyvinyl chloride (PVC) foams under compressive dynamic loading conditions and show that PVC foams show a higher degree of strain rate dependency on performance when compared to polyurethane foams. It is observed that in these materials, stress is dependent on combined effects of strain rate, stress state, and mode of failure. In another study, Di Landro et al. [17] observed the effects of density on mechanical response, and found that higher density foams have a higher compressive plateau, so they are able to absorb more energy at constant stress. This may help reduce transmitted load while limiting the load on the structure, compared to a lower density foam, which may densify and end up transferring higher loads. They also observed that higher density foams transmit relatively higher instantaneous acceleration loads, which are often an undesirable type of load transfer in impact applications [24]. A number of other studies aimed at studying density effects have found that higher densities in foams lead to increasing energy absorption with increasing strain rates [7, 10, 13, 14] up to a threshold density and strain rate. For example in one study, Ouellet et al.[49] found this threshold rate to be approximately $1000s^{-1}$, after which the rate sensitivity is observed to change [49, 104].

In addition to efforts made to investigate material responses under different stress states [10, 14, 17, 107], and for a range of density effects [7, 10, 17, 108–110], the sensitivity of mechanical response to microstructure (pore morphology) in foams is also documented [3, 7, 10, 111, 112]. One way to examine material microstructures is through the use of micro X-ray computed tomography [113] which allows for examination of the internal microstructure of the foam. Micro X-ray computed tomography (XCT) is a widely

recognized characterization technique that makes use of computer processed X-ray measurements to reproduce cross−sectional images of internal objects for a range of different materials [3, 77, 79]. By examining the microstructure of the foam material before and/or after experiments, one is able to gain insight into the relationship between foam pore size and wall thickness with the mechanical behavior of the material. This is important because some studies [7, 10] involving foams have compared different microstructures, finding that the smaller pore size generally had higher strengths and absorbed more energy at high strain rates when compared to larger pore sizes. In one example, Bouix et al.[7] also found that changes in the strain rate have smaller effects on foams with smaller pore sizes compared with larger pore sizes. Altogether, these studies point to the importance of the microstructure length scales on the rate-dependent response of polymeric foams.

In the present paper, we seek to explore the effects of density, microstructure (pore size and wall thickness), and strain rate on the mechanical response of polymeric foams. This paper is comprised of the following sections: first, experimental methods are presented that include microstructure characterization techniques, specimen preparation, and mechanical testing. This is followed by the presentation of the experimental results. These results are supported by XCT images, cumulative distribution functions of microstructural features (e.g., pore size), and stress-strain curves. Finally, empirical relationships of mechanical strength parameters are described along with detailed discussion of implications and contributions of the present work with respect to the existing literature.

The materials investigated in this work are open-cell polyurethane foams that were manufactured by PORON. In this study, foams of three different densities are examined under uniaxial compression loading at quasistatic, intermediate, and dynamic strain rates. The material densities were: 195 kg/m^3 (termed 'low density' or LD throughout for brevity), 244 kg/m^3 (termed 'medium density' or MD) and 405 kg/m^3 (termed 'high density' or HD). The density of the samples is measured through Archimedes principal (weighing and measuring displacement volume) and these measurements match those listed by the supplier, which are obtained using ASTM D 3574-95 Test A standard [114]. The chemical composition of the materials is held proprietary by the manufacturer and some of the physical and mechanical properties provided by the manufacturer are listed in Table 4.1. Generally, it is observed that strengths increase as the density increases.

4.2.1 Microstructure Characterization

Shown in Figure 4.1 are the microstructures of the three different density foams. These images are XCT scans of the pristine specimens. Visually comparing the low density

TABLE 4.1: Physical and mechanical properties of PORON XRD foams provided by the manufacturer [114–116].

Property	Test method	Material		
		LD	MD	HD
Density (specific gravity)	ASTM D 3574-95 Test A	0.14	0.19	0.40
Compressive strength (kPa)	$0.08s^{-1}$@ 25% deflection	8-23	10-38	69-138
Tear Strength, min. (kN/m)	ASTM D 624 Die C	0.8	0.9	2.5
Tensile Elongation, min. (%)	ASTM D 3574 Test E		>145	
Tensile Strength, min. (kPa)	ASTM D 3574 Test E	207	310	483

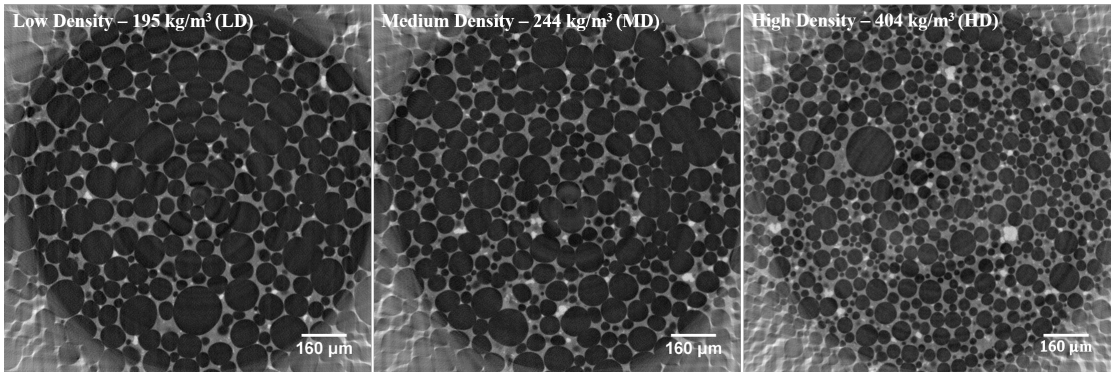

FIGURE 4.1: Pristine microstructures of open-cell polyurethane foams with different densities of $195kg/m^3$(LD), $244kg/m^3$ (MD), and $405kg/m^3$ (HD) obtained from X-ray tomography scans.

foam ($195kg/m^3$) to the high density foam ($405kg/m^3$), differences in pore sizes and the number of pores are noted. It is generally observed from these images that as density decreases the average pore size typically increases, and for a given specimen size, this causes a reduced number of total number of pores available for pore characterization. These characteristics will be quantified later. Conventionally [23, 101], authors classify open-cell foams based on the relative density (ρ/ρ_s) of the foam. In the present study, X-Ray tomography reconstructions are also used to identify the connectivity of the pores to determine whether or not the foam is open- or closed-cell, and it was also found that the ratio of volume of completely closed pores compared to scan volume was relatively low, confirming the macroscopic open-cell nature of the foams.

Synchrotron radiation based X−ray microtomography was performed at the Biomedical Imaging and Therapy (BMIT) facility − Canadian Light Source (CLS)[95] 05ID−2 − SOE−1 hutch, Saskatoon, to obtain volumetric information on the microstructure. The specimens were mounted with their loading axis parallel to the scan direction. The resolution of the scans was $1\mu m$ per voxel and the maximum scan thickness was $5mm$.

This resolution provides sufficient scan volume in order to resolve the cell wall thickness ($< 30\mu$m), and pore size ($< 250\mu$m) analysis. The specimen loading stage operated in intermittent motion and each specimen scan comprised 900 tomograms being acquired within 10 minutes over a 360° rotation. Reference images without the specimen, and dark images without X-rays were also obtained before and after every scan to increase the quality of images during background filtering reconstruction [117].

TABLE 4.2: Microstucture characterization pore metrics

Type	Density (kg/m^3)	Foam thickness (mm)	Average pore size (μm)	Average wall thickness (μm)	Average porosity (ϕ)
LD	195	4.2	60 ± 55	10 ± 9	0.87 ± 0.06
MD	244	3	45 ± 35	11 ± 10	0.83 ± 0.06
HD	404	3	32 ± 30	11 ± 10	0.76 ± 0.05

A MATLAB-based program was developed to perform image segmentation on the XCT slices to calculate pore sizes and wall thicknesses. First, the original grayscale images are imported into an array in MATLAB and stacked over each other. Then, all images are converted to a binary scale with appropriate thresholding (to account for differences in contrast in the XCT scans) so as to identify the pore boundaries and empty spaces between them. This gives the representation of the specimen in the form of a three dimensional matrix containing 1's (denoting solid material) and 0's (denoting empty spaces or voids). The border pores are cropped out to remove the edge artifacts and a cylindrical projection containing pores remains as seen in Figure 4.2(a). Using a standard MATLAB function called "erosion", the walls are thickened to connect walls that may have been disconnected during image processing or pore scanning, and this produces completely closed pore structures. An example of the resulting image is shown in Figure 4.2(b). Using the images of the thickened pores shown in Figure 4.2(b), the centroids of every pore volume are calculated in 3D using the standard "regionprops" function and stored. Next, the coordinates of all the centroids are plotted onto the original 3D binarized stacked images. From these centroids, vectors are drawn in 6 orthogonal directions in $\pm x$, $\pm y$ and $\pm z$ as shown in Figure 4.2(c). The program then calculates the number of pixels encountered as 0's (within a pore) followed by 1's (as it passes through a pore wall) along these vector directions and these pixel counts are multiplied by appropriate length scale conversions to calculate pore sizes and wall thicknesses. The pore sizes and wall thicknesses for each specimen are then tabulated and stored for further data processing. This type of analysis needs to be performed when working with open-celled microstructures because pore sizes cannot be easily determined like in other material systems like advanced ceramics [118]. Shown in Table 6.1 are the pore metrics calculated from characterization of the three density foams. The first column shows

the type of foam, followed by density, and the as-received sheet thicknesses. The table also shows the average pore size, average wall thickness, and average porosity (ϕ) for all foams. The porosity of the low, medium, and high density foams is measured to be 0.87 ± 0.06, 0.83 ± 0.06, and 0.76 ± 0.05, respectively. These differences in porosity are obtained as a result of different thresholds across difference sample scans. Due to the variation of pore sizes in these materials, the total number of pores characterized for each density varied among each other, and were found to be ~ 1750 pores, ~ 3100 pores, and ~ 9950 pores for the LD, MD, and HD foams, respectively. It is to be noted that the variability in these pore metrics measurements is determined by the thresholding limits from the reconstruction. To explore the repeatability of the results, the initial stack of images were rotated by various degrees and the analysis was carried out on these images. Pore size and wall thickness distributions were found to be equivalent to when performing these operations on the original image stack.

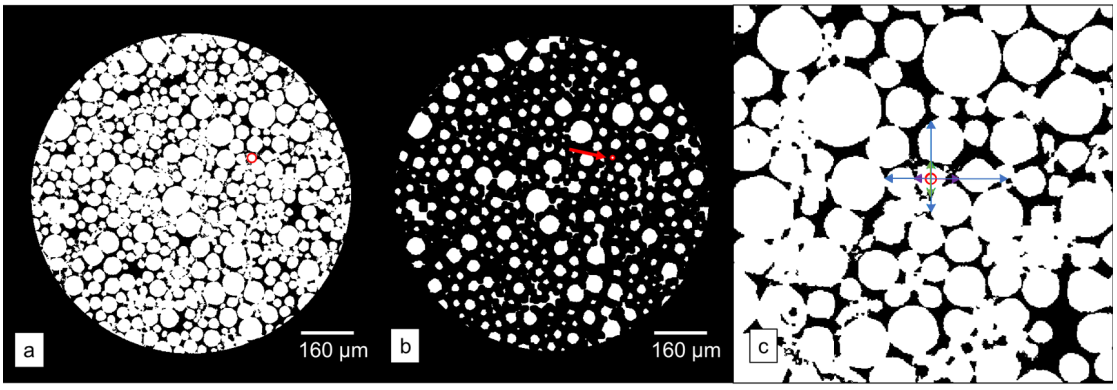

FIGURE 4.2: Microstructure characterization methods (a) Binarized image of foam scan with border pores cropped out. (b) Thickened walls to identify pore centroids. (c) Zoomed view of a single pore shown with red arrow from (b) showing orthogonal vectors extended from pore centroids to calculate pore size and wall thickness.

4.2.2 Specimen Preparation for Mechanical Testing

To ensure consistency across strain-rates in compression testing, a single specimen diameter was used for both quasistatic, intermediate, and dynamic experiments. Using a special metallic hollow punch, disk specimens of diameter $8.0 \pm 0.3mm$ were cut from an as-received sheet of uniform thickness of 4.2 mm, 3.0 mm, and 3.0 mm for the LD, MD, and HD foams, respectively, with the axis of the cylindrical disk oriented along the through-thickness direction of the as-received sheet of foam. Care was taken to ensure that the end surfaces of the specimens were parallel, and that minimum damage was induced to the edges during specimen preparation. The sensitivity of material strengths to geometry, testing methods, and specimen-size effects are widely discussed in literature

[16, 22]. It is noted that differences in the compressive strengths between this study and those provided by the manufacturer is expected because the specimen sizes used in the ASTM D3574-95A standard [114] is cuboidal shape with a dimensions of f 50 mm x 50 mm x 25 mm , whereas the test specimen size in our study is cylindrical shape with 8 mm diameter and thickness was governed by the thickness of the as-received foam sheets. The sample geometries were selected based on as-received sheets, ability to compress to sufficient densification strains based on available experimental setups, to have consistent sample sizes across test setups, and to achieve reasonable strain rates and force equilibrium. These samples are similar sizes to those in the literature [3, 119]. It is noted that potential differences in composition, pore size, and wall thicknesses may also occur as a result of different sizes of as−received sheets than those that are reported by the manufacturer.

4.2.3 Quasistatic Compression Experiments

The specimens were tested in quasistatic compression at strain rates of 0.001 to $0.1s^{-1}$ using an Instron E3000 material testing system. A 3 kN load cell with a background noise corresponding to approximately ±0.01 N recorded the time histories of the forces, and the displacement of the piston was measured to an accuracy of 0.001 mm using a linear variable differential transformer displacement sensor. The load cell resolution is sufficient to capture the necessary trends in the force measurement needed to properly assess the elastic properties. The engineering stresses are calculated by dividing the applied load by the original specimen surface area, and the engineering strains are computed using digital image correlation (DIC) using a high-speed AOS PROMON U750 camera. DIC methods are discussed in a later sub-section. Three trials with the same loading conditions were performed to verify repeatability of the material behavior.

4.2.4 Intermediate Compression Experiments

Intermediate strain rate compression experiments were performed at two rates using different loading techniques. The first strain rate, $1s^{-1}$, utilized an Instron 8871 load frame at displacement rates of 3 mm/s for MD and HD foams and 4.2 mm/s for LD foams, corresponding to the sample thicknesses. A 1 kN load cell with a background noise corresponding to approximately ±0.01 N recorded the time histories of the forces. The deformation of the sample was recorded with a FLIR Grasshopper 3 camera at $164fps$ with a $200mm$ macro lens. Both the force measurement and image capturing was controlled by the DIC software to ensure the data were time-synchronized. The sample

surface was illuminated with a halogen fiber optic light that ensured good brightness even at high strains.

The second intermediate rate was approximately 175 to $250s^{-1}$ and utilized a drop tower to reach the necessary velocity. A force sensor was attached to a steel base plate, and the sensor had a metal loading cap screwed into it that transmitted the force to the quartz sensing element inside the sensor. The foam sample was placed on the loading cap. A tup, that is the metal rod is positioned above the sample, and dropped to load the sample. The tup is relatively heavy ($\sim$ 4.5 kg) compared to the foams and so the velocity is nominally constant over the majority of the loading time. The slowest velocity achievable was programmed into the drop tower software ($770mm/s$), corresponding to a drop height of approximately $25mm$ above the sample. The force sensor was a PCB 200B04 with a capacity of $4.45kN$ and an upper frequency limit of $75kHz$. The voltage output of the force sensor was measured with an oscilloscope that was triggered on the rise of the sensor output following impact. The sample deformation was recorded with an iX716 high speed camera at $20,000fps$ and an exposure time of $20\mu s$ with a $200mm$ macro lens. When the scope triggered, a trigger signal was sent to the camera. In order to time-synchronize the force and camera framing, the camera exposures were sent to the oscilloscope and were also recorded. The samples were illuminated with multiple halogen fiber optic lights to ensure optimum brightness and contrast.

For the intermediate compression tests, the engineering stresses were calculated by dividing the applied load by the original sample area, and the engineering strains were computed using DIC software. At least three tests with the same loading conditions were performed to verify the repeatability of the foam behavior.

4.2.5 Dynamic Compression Experiments

The dynamic compression experiments were performed using a split-Hopkinson pressure bar (SHPB) apparatus also known as the Kolsky bar, with bars that were made of solid Aluminum (Al). The Kolsky bar apparatus consists of a projectile launcher, a striker bar (Al), an incident bar (Al), and a transmission bar (Al). In a Kolsky bar experiment, a striker bar is launched from the projectile launcher and strikes the incident bar, generating an elastic stress wave that travels through the incident bar and through the specimen, dynamically loading it. Due to the mismatch of mechanical impedances of the bar material and the foam specimen, mechanical waves are generated at either end faces of the specimen. Two strain gages are mounted on diametrically opposite sides of the incident bar, and the transmission bar via a bridge configuration, to record these mechanical waves as strain histories, and they are connected to a data acquisition system.

The strain gages had a resistance of $350 \pm 0.3\%$ with a gage factor of $2.130 \pm 0.5\%$ (Micro Measurements CEA-13-250UN-350 semiconductor strain gages). Each strain gage set was connected to an individual conditional amplifier (Vishay InterTechnology 2310B), and a gain of ~ 100 to 1000 is applied on the transmission gage signal because of the small magnitudes of transmitted pulses. The output from the conditional amplifiers is saved to an HBM Gen3i High-Speed Recorder at a sampling rate of 25 MHz. The background noise in these strain measurements was $\approx \pm 1$ micro strain, and was found from careful observation of transmitted gage raw voltage data. The 1 micro strain corresponds to $\sim 20\%$ of the measured strain at the onset of yielding (~ 5 micro strain). The lengths of incident bar and transmission bars were 1000 and 910 mm respectively, with a diameter of 12.7 mm. A 500 mm long solid flat-ended projectile with a similar diameter was used in this study to generate a top-hat loading profile. The length of the bars and the relative positioning of strain gages avoided overlapping of the stress waves [57], also ensuring that longer loading durations are available in order to obtain larger strains. A 160 GSM paper was used as a pulse shaper for the dynamic experiments, and this was selected after multiple trial and error methods were pursued using different pulse shapers. Paper pulse shaper was also used in other studies in literature [120]. The use of a paper pulse shaper did not change the rise time but helped reduce high frequency noise in the input wave, as well provided acceptable force equilibrium. The controlled deformation of the pulse shaper generates the desired loading profile of the input pulse that is a flat top hat, and this ensures constant deformation rate in the specimen under dynamically equilibrated stress conditions [46]. In our Kolsky bar experiments, the engineering stress is calculated from the transmitted strain-time history [121, 122].

In the present study, the dynamic compression experiments were coupled with an ultra-high-speed Shimadzu HPV-X2 camera to visualize deformation features, as well as to perform strain measurements using DIC. The dynamic stress equilibrium in the specimens was verified by comparing the forces at input bar-specimen and specimen-transmission bar interfaces, and the force curves indicated that reasonable force equilibrium was attained within the specimen. Example figures of force balance curves and filtering of the dynamic stress-strain curves are provided by the authors in Bhagavathula et al.[25]. The challenges of developing Kolsky bar systems to accurately measure the dynamic response of foams are well documented in the literature [7, 10, 13, 14, 123], and the testing methods that are pursued in the present study are consistent with those in the literature.

4.2.6 Digital Image Correlation (DIC)

DIC is used to measure the strain during experiments in all experiments. DIC is a non-contact full-field quantitative strain measurement technique that allows the determination of in-plane displacement components, and therefore the surface strain fields experienced by the specimen during loading [113]. Imaging of specimen surface was conducted in all experiments to provide images for DIC. As mentioned earlier, the quasitatic testing setup was coupled with a high-speed camera AOS PROMON U750 which provides a resolution of 1280 x 1024 pixels and recorded at a frame rate of 100 frames per second. A FLIR Grasshopper 3 camera at 164 fps was used to record the $1s^{-1}$ intermediate compression experiments, and an iX716 high speed camera at $20,000fps$ was used for the 175 to $250s^{-1}$ intermediate compression experiments. In the dynamic compression experiments, the ultra-high-speed camera Shimadzu HPV-X2 camera captured 256 images for each experiment and is triggered by a split signal from the incident strain gage. In dynamic experiments, the ultra-high-speed camera operated at a framerate of 1 million frames per second at a resolution of 400 x 250 pixels. The camera output pulses were used to correlate times between the images and the strain gage measurements. All cameras were equipped with a telecentric lens to eliminate out-of-plane motion capture. The naturally occurring microstructural pore texture of the surface of the specimen was too small to be captured using the available pixels and hence all specimens were coated with black paint using an ultra-fine point Harder and Steenbeck Infinity airbrush to form a speckle pattern on the specimen surface for accurate correlation purposes. A sample speckle pattern is shown in Figure 4.3(a) for quasistatic compression experiment of PORON HD at $1s^{-1}$.

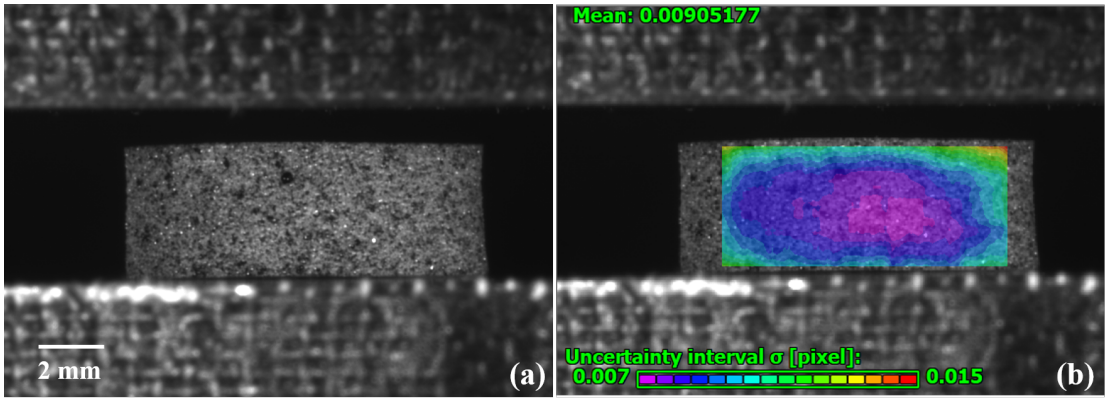

FIGURE 4.3: (a) Speckle pattern on prepared cylindrical specimen (b) Region of interest used to compute strains using digital image correlation.

These camera images are used for DIC strain measurements using the VIC-2D 6 software [124]. In DIC analysis, a region of interest (ROI) is defined on the sample surface, and

TABLE 4.3: DIC parameters

Technique	**Quasistatic 2D**	**Intermediate 2D**	**Dynamic 2D**
Pre-filtering	Gaussian	Gaussian	Gaussian
Subset	7	5	1
Step	72	65	31
Correlation criterion	ZNSSD	ZNSSD	ZNSSD
Shape function	Affine	Affine	Affine
Interpolation function	Bicubic Spline	Bicubic Spline	Bicubic Spline
Number of images	∼3000	∼250	128
Pixel to mm conversion	98 px/mm	85 px/mm	48 px/mm
Strain smoothing method	Savitzky-Golay	Savitzky-Golay	Savitzky-Golay

displacements of all the subsets defined within the ROI are tracked as the specimen deforms during loading. In each displacement step, the subsets in the deformed images are "matched" with the pattern in the reference image using the difference in gray scale intensity levels at each interpolation point. In each subset, a correlation peak is defined by interpolating the grayscale level at or between pixels, and the position of the peak provides a local displacement [125]. For these measurements, the optimum settings of the brightness and contrast on the material surface is obtained by using a combination of high intensity LEDs and speckle patterns. The system was adjusted for every specimen such that images with good sharpness and exposure are obtained which provided an optimal subset size in the VIC-2D 6 software. The software's built-in algorithm provides a "suggested subset size" and noise level with the minimum estimated error that is based on the quality of speckle pattern and contrast level using the reference image. An example ROI used for DIC measurements is shown in Figure 4.3(b) and the noise level was found be to < 0.01 in all the experiments. The DIC parameters are noted in Table 4.3. For the large deformations experienced during compression, incremental DIC is utilized to avoid de-correlation, which uses the image of the previous displacement step as the reference image for correlating the positions of the speckles in the next displacement step. It is to be noted that the primary interest in this paper is to measure the axial strain experienced by the specimens, and 2D DIC allows for the accurate measurement of this strain [126].

4.3 Experimental Results

4.3.1 Microstructure Characterization

4.3.1.1 Pore size characterization

By visualizing the pore size data (or wall thickness data) in an empirical distribution function (eCDF), insights can be gained as to what pore size length scales are activated

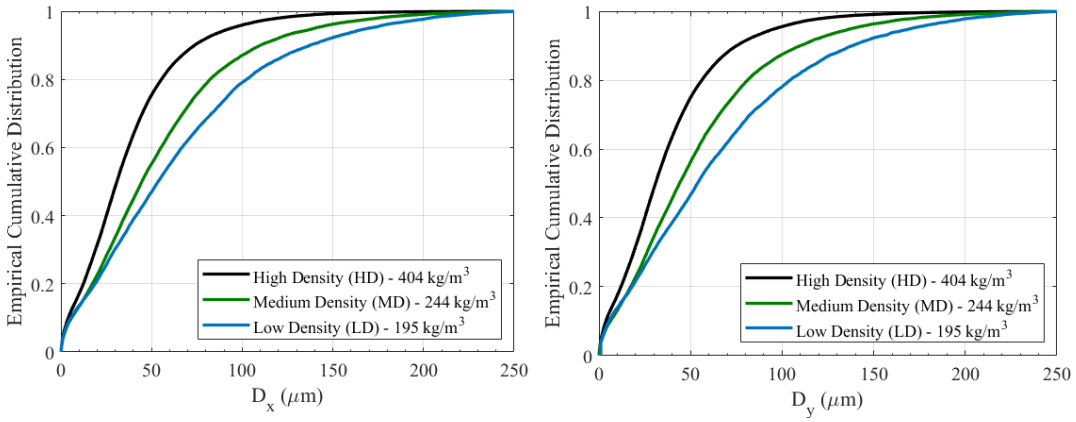

FIGURE 4.4: Empirical distribution functions showing pore sizes of different density foams in both x and y directions. The black, green and blue curves represent the high density (HD), medium density (MD), and low density (LD) foams, respectively. Pore size eCDFs appears to shift left as density increases.

during testing. The cumulative distribution [127] is defined as:

$$G(x) = \int_0^x g(\bar{x})d\bar{x} \tag{4.1}$$

where $g(\bar{x})$ is the probability distribution of the pore sizes. The pore size data set in each direction is a discrete set of n pores with sizes of ℓ_i (i=1...n). Ordering this data for increasing pore size, and assigning a probability of $1/n$ to each pore, the normalized empirical cumulative distribution function can be computed as the sum of these probabilities:

$$G_e(\ell) = \frac{1}{n}\sum_{i=1}^{n} I(\ell_i \leq \ell) \tag{4.2}$$

where the indicator function I has a value of 1 if $\ell_i \leq \ell$ and 0 otherwise. Pores with sizes less than $250\mu m$ were considered for further analysis based on visual confirmation from the XCT scans (Figure 4.1). Orthogonal scans in the z direction were also obtained and the pore size distribution in the z direction was found similar to that of the x direction, enabling us to compare cumulative distribution of pore size in x and y directions. Shown in Figure 4.4 are the eCDFs which are used to identify the likely range of the pore sizes and trends, where D_x and D_y represent the pore diameters in x and y directions, respectively. This is achieved by looking at the values between the 10th and 90th percentiles. It is observed that the different density foams have varied sizes in the x and y directions. For the low density foam, the limits lie between $5 - 114\mu m$ for the x, and $6 - 142\mu m$ for the y directions. For the medium density foam, the limits lie between $6 - 100\mu m$, and $8 - 110\mu m$ for the x and y directions, respectively. For the high density foam, the pore sizes are found to be near spherical in nature with limits ranging from $5 - 75\mu m$ for both x and y directions. Generally, the eCDF shifts to the right as the density decreases, and

this indicates that pore sizes are larger in the lower density foams. The eCDF curves also reveal that the the sizes for D_x is greater than D_y, and this is likely a result of the foaming direction during the manufacturing process.

4.3.1.2 Wall thickness characterization

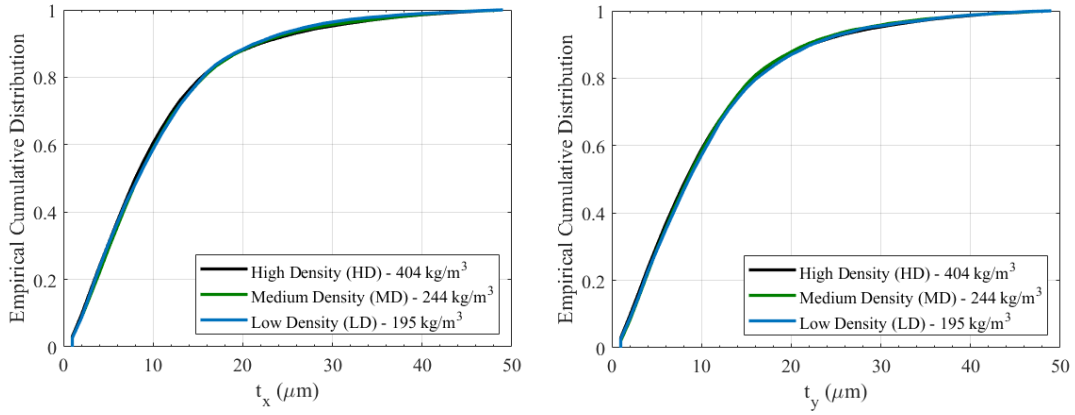

FIGURE 4.5: Empirical distribution functions showing wall thicknesses of different density foams in both x and y directions. The black, green and blue curves represent the high density (HD), medium density (MD), and low density (LD) foams, respectively. Wall thickness eCDFs appears to be similar for all densities.

Shown in Figure 4.5 are the eCDFs of the wall thicknesses for all the different foams. Wall thickness less than $50\mu m$ were considered based on visual confirmation from XCT images (Figure 4.1). In Figure 4.5, t_x and t_y represent the wall thicknesses in x and y directions, respectively. The wall thickness range is measeured to be between $2\mu m$ and $23\mu m$ in both x and y directions for the pristine specimens, and it is is observed that profiles of t_x and t_y are similar for all the different density foams. These observations are made from looking at individual plots of each specimen with t_x and t_y on the same plot. Although relative differences between the different density foams are minor ($< 1\mu m$), these minor differences in wall thickness are to be noted.

4.3.2 Compression Experiments Results

The stress-strain responses of the different density PORON foams at quasistatic, intermediate, and dynamic strain rates are shown in Figure 4.6. The y-axis represents stress in megapascals in a logarithmic scale and the x-axis represents engineering strain. It is to be noted that three trials for each experiment were performed for repeatability and representative curves are shown.

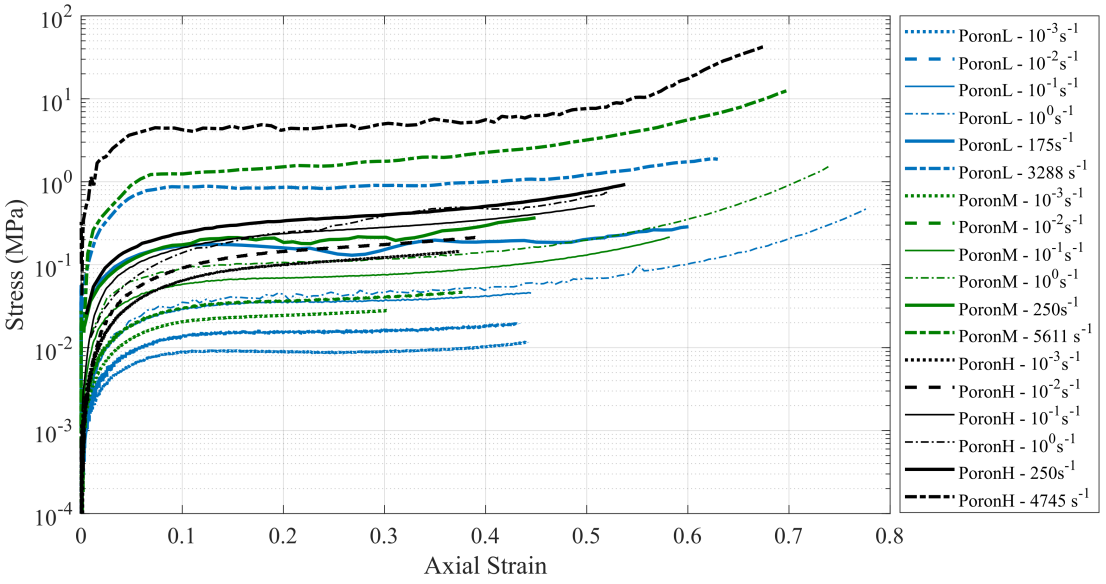

FIGURE 4.6: Figure showing the representative stress-strain responses under quasistatic, intermediate, and dynamic compression for different density PORON foams. The blue, green and black curves represent the low density, medium density, and high density foams, respectively. The different strain rates are represented by separate line styles as shown in the legend.

All curves show three stress regimes, namely, *elastic behavior* up to a yield or *collapse* stress (σ_{pl}), a *plateau* stress regime where the stress is near constant, and a *densification* regime where stress increases rapidly with increasing strain [7, 10, 113, 128]. In this paper, due to differences when DIC correlation is lost, different maximum strains were obtained throughout the experiments. From Figure 4.6, it is observed that the compressive response of the PORON foams in all the strain rate regimes exhibit a typical elastomeric foam behavior with some minor differences. Namely, typical foam responses have a sudden change in slope when the stress reaches the elastic stress limit and its value is easily identifiable [16, 22, 46]. For all the different densities, it was found that there was a gradual transition from the elastic regime to the plateau regime beginning at a strain of ~ 0.02 and plateauing at approximately 0.08 strain, which marks the range of yield strain for this material. Polymeric foams have a pore collapse stress (σ_{pl}, stress at 0.25 strain) which represent the stress when foams start to deform post elastic limit when loaded beyond the linear-elastic regime. The collapse of the pore structures gives a long, approximately horizontal plateau to the stress-strain response, where the strain is partially recoverable and some permanent deformation is observed to the foam microstructure post-experiment. In this study. the elastic modulus and the pore collapse stress across the varied strain rates for the different density foams are tabulated in Table 4.4. Comparing the collapse stress between the quasistatic and dynamic strain rates, the dynamic values are anywhere from 70 to 90 times the quasistatic values and, in the case of the elastic modulus, the dynamic ones are higher by 100 to 150 times.

TABLE 4.4: Elastic modulus and pore collapse strengths of PORON foams at quasistatic, intermediate, and dynamic strain rates.

	Elastic modulus (MPa)			Collapse stress (kPa)		
Strain rate	LD	MD	HD	LD	MD	HD
0.001	0.12±0.01	0.23±0.02	0.62±0.01	7.78±0.75	17.19±2.51	65.38±0.68
0.01	0.27±0.01	0.42±0.04	0.79±0.03	15.07±0.61	29.63±1.11	90.13±1.24
0.1	0.52±0.04	0.94±0.01	1.65±0.20	29.97±0.76	56.58±3.22	159.17±1.84
1	0.77±0.04	1.73±0.11	4.37±0.63	55.51±0.72	93.77±2.72	276.72±29.39
175	3.62±0.43			243.12±21.22		
250		9.32±0.39	25.06±2.62		491.95±56.98	1738.84±171.94
3275±840	14.19±4.71			669.56 ±112.71		
4577±1117		23.71±5.31			1344.67±159.41	
4307±1330			92.07±29.64			4629.54±447.25

4.4 Discussion

In this section, first, the discussion on microstructure characterization along with its implications for modeling are presented, followed by the discussion of effects of density, and strain rate on mechanical response of these foam materials. Here, the deformation mechanisms associated with the different deformation regimes are discussed. The deformation and failure mechanisms described here are directly dependent on the foam microstructural length-scales [23] such as pore size and wall thickness, and measuring these parameters would help for accurate modeling of material deformation at the microstructure length-scale. The mechanisms described here mostly presents the response of foam under compressive loading applied in the rise direction where the cell walls take the bulk of the load during compression, and also applies to all the experiments performed in this paper.

All three foams of different densities in this study have similar stress-strain behavior: an elastic response followed by a plateau stress stage. However, some differences can be noticed between the strain rates and densities in the experiments in this paper. For example, in quasistatic loading, the medium and the high density foam shows a collapse stress of ~ 4 and ~ 5 times larger as compared to the low density foam, respectively. For the dynamic results, all foams do not show a distinct post-collapse hardening transition that is common in PVC foams [10], and polystyrene foams [7], but rather demonstrate a larger length of the plateau stress regime that is different from what is observed in quasistatic loading conditions. When the specimen is loaded beyond the collapse stress, it is expected that larger pores get collapsed initially because of susceptibility of buckling of longer structures (cell walls) [3], and as straining continues, there will be fewer of the large pores since they are being crushed out. As the strain increases, the average pore size decreases due to crushing out of the porosity and pore collapse of larger pores, which results in an increase in stress. At small pore sizes, post-collapse hardening occurs due to a combination of bending, axial deformation, and other forms of deformation like plastic deformation [9, 23]. In the tests in this paper, it is noted that the plateau stress and elongation of the plateau regime are found to be higher for dynamic strain rates. This indicates that pore collapse increases with increasing strain rate [46] and, hence, the energy absorption capabilities are improved at higher strain rates [8, 46]. In the following sub-sections, these phenomenon and the results presented in the previous section are discussed in further detail and compared to existing data in the literature.

4.4.1 Microstructure Characterization and Implications for Modelling

From the Figures 4.4 and 4.5, it is observed that the pore size decreases with increasing density, whereas there is no discernible change in wall thickness with a change in density. Knowledge of the microstructure pore size and wall thickness is important because these microstructure differences are related to the mechanical responses [10, 46, 129] and performance [7, 36] of foams. For example, it is known that smaller pore sizes are less prone to buckling which results in higher collapse stresses [12], which is observed in the present study in the HD foam which has the smallest pores and the highest collapse stress. In addition, it is also observed in literature that as pore size decreases, the cell walls become more susceptible to micro-inertia effects [7, 12, 16]. Finally, it is to be noted that micro-inertia effects are greater in the case of dynamic loadings, but also when the foam density increases [7]. This has implications for material design in impact applications such as for foams in the present study, where the HD foam is observed to have the highest elastic and collapse stress magnitudes and the smallest average pore size of all the three density foams, and the mechanical strengths are observed to increase with increasing strain rate. These observations in the present study are consistent with the literature [7, 12, 16, 36, 108].

Further, from the porosity measurements discussed in this paper, a linear relationship within 1% error was found to exist between the pore solid content $(1-\phi)$ and the density (ρ) of the foams give by:

$$1 - \phi = A * \rho \tag{4.3}$$

where the value of ϕ varies from 0 to 1, and when $\phi = 0$, $\rho = \rho_s$. From a curve fit, the value of A is found to be equal to $8 * 10^{-4}$ for the PORON foams and the density of solid polyurethane polymer at $\phi = 0$ was calculated to be $\rho_s \approx 1250 kg/m^3$. This value is close to existing data in literature for open-cell flexible polyurethane foams [23] where the elastic modulus of the solid polymer material at quasistatic strain rate is given as $E_s = 45MPa$ [23]. This value of E_s will be further used to develop other empirical relationships later in the Discussion section. Similar relationships are discussed by Brydon et al.[36] in their paper where they relate porosity, and volume of the bulk and parent polymer in an effort to determine the incompressible porosity of foam materials during compression.

Next, the modeling implications of probing the foam microstructure and discuss the necessity and advantages of including real microstructures in material models are explored. This is accomplished through comparing pore sizes of foams of different relative densities. Shown in Figure 4.7 are some existing trends [40, 101, 113] of pore sizes of varying density polyurethane foams with relative densities $(R = \rho/\rho_s)$ (ρ_s - base polymer density)

less than 0.25, plotted along with data in the present study. Shown in Figure 4.7 is a plot of average pore size vs. relative density, and both open- and closed-cell foams are considered for comparison. This data was obtained from published values in the literature [40, 101, 113], where average pore size and foam relative densities were reported. Additional data exists in the form of images in other studies [9, 18, 130] but often only one figure is presented, and it is therefore difficult to extrapolate average pore sizes from them. It is to be noted that the foams used in these studies might have different base chemical compositions or the presence of certain additive particles during foaming processes [25, 123], and this contributes to the observed variation in pore sizes in the foams. Generally from Figure 4.7, it is observed that overall pore size decreases with increasing relative density. It is also observed that at a similar relative density, closed-cell foams have relatively bigger pore sizes when compared to open-cell foams. For the foams in this study, it is observed that both the average pore sizes and pore size variability decreases with increasing relative density. In their study, Jarfelt et al. [101] measure pore sizes of different density foams to aid in thermal conductivity calculations of foam materials. In another study, Mills et al. [40] note the differences in microstructures with respect to closed-pore content, pore orientation and spacing, and pore size, and relate these parameters to foam manufacturing processes. Generally, one of the common implications of many of these studies in literature focused on characterization [40, 101, 131–133] is the necessity of including such measurements of real microstructures in micro-mechanical modeling approaches to improve existing models, and it is hoped that data in this paper contributes to those studies.

Finally, in the existing literature, numerical models [36–39] have been developed for polymeric foams to predict the behavior of open-cell foam materials under compressive loading. In some models in the literature, the loading directions are arbitrary to the foam rise direction [37, 39], and in that case, it is observed that models do not necessarily capture the effects of microstructure. It is also observed that micro-mechanical models based on idealized foam microstructures of either ordered [38, 134] or random network [8, 37, 38] of pores may not always reflect the experimental data accurately in one particular loading direction [37, 38]. Further, it is to be noted that the structural response of foams is also governed by the cell geometry (cell topology, foam density and anisotropy ratio) and by properties of the base polymer material [40]. Existing research on open-cell foams have also considered a wide range of pore microstructures, including polyhedrons, truncated octahedrons and rhombic dodecahedrons [37]. Many studies [36, 38, 40, 128] note a necessity of including these length scales in the constitutive models to better predict material response. This can be achieved by generating unit cells based on statistics of real microstructural parameters [131] of foams such as closed-pore content, pore size and wall thickness, and the pore orientation and spacing. One of the

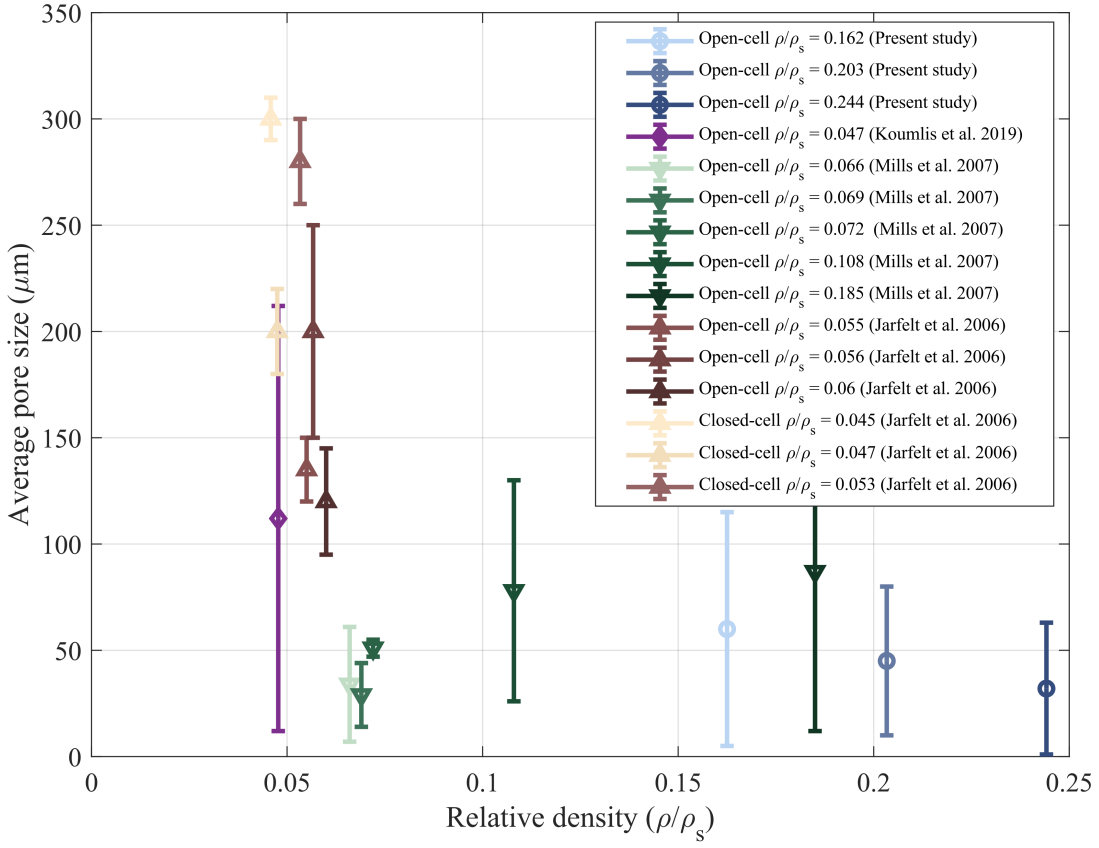

FIGURE 4.7: Trends of average pore sizes of varying density open-cell and closed-cell polyurethane foams with different chemical compositions/additives for foams with relative density less than 0.25. Data in the legend is ordered based on relative density for a given study.

identified contributions of the present study is that the characterization techniques provided in the present study can be employed directly, or improved upon, to identify such statistics of foam microstructures to enable better micro-mechanical modeling.

4.4.2 Effect of Density on Compressive Response

As seen from Figure 4.6, the collapse stress, peak stress and plateau stress increase with increasing material density. It is also observed from the figure that the span of the plateau stress regime decreases with increase in foam density. From measurements, it was observed that the initial stiffness increases with increase in foam density. To relate the mechanical properties and relative density of the polymeric foams, power-law relationships are commonly defined in the literature (e.g., closed-cell polymeric foams [10] and open-cell foams [23]):

$$\sigma_{pl}/E_s = B(\rho/\rho_s)^m \tag{4.4}$$

where $\sigma_{pl}(MPa)$ is the collapse stress of the foam, $E_s(MPa)$ and $\rho_s(kg/m^3)$ are the elastic modulus and density of the solid base polymer material, respectively, and B and m are empirical fitting parameters. Gibson and Ashby [23] had initially developed a very similar expression based on micro-mechanical formulations for various low density foams and found that $\sigma_{pl}/E_s \approx (\rho/\rho_s)^{1.5}$ for open-cell foams and $\sigma_{pl}/E_s \approx (\rho/\rho_s)^2$ for closed-cell foams. In a more recent study, Saha et al.[10] found that the power law constants change with loading conditions and found m to vary between 1.4-1.69 for a strain rate range of 0.001 to $1600s^{-1}$. From both existing published data and the data in this study (Table 4.5), the power law coefficients appear to be rate-dependent, and different for foams made of different base materials, with m being increasingly more rate-dependent for higher strain rates. The value of the pre-multiplying term B is hypothesized to depend on parameters like: open or closed cells, porosity, microstructure length scales (wall thickness and pore size), and the constituent material [23]. Overall, it is noted due to the differences in base material, pore structure, strain rate, and loading conditions, that power-law fits to describe density effects are not suitable for a wide range of strain rates. Next, some ideas on stress scaling to predict collapse stress as a function of strain rate in these materials are explored.

4.4.3 Effect of Strain Rate on Compressive Response

In this subsection, mechanical property data from various open-cell [113] and closed-cell [10, 49, 133] foams are compiled, and compared those with our own. This data is used to make appropriate comparisons wherever possible, but is mainly shown to denote magnitude differences between materials. To assess the effect of the strain rate and density on mechanical response, parameters of elastic modulus and collapse stress are identified from the experimental results in this paper. The collapse stress and elastic modulus values were plotted as a function of strain rate for a range of foam densities, along with data from existing literature, in Figures 4.8 and 4.9. Shown in Figure 4.8 is the comparison of elastic modulus of polyurethane foams of varying densities with varying strain rate. From Figure 4.8, for open-cell foams in the literature [113], and in this study, it is observed that elastic modulus increases with foam density and this relationship is even more pronounced at higher strain rates. For the closed-cell foams in the literature [10, 49, 133], the elastic modulus is observed to increase with increasing foam density and strain rate.

Next, shown in Figure 4.9 is the comparison of collapse stress of polymeric foams of different densities [10, 49, 113] with varying strain rate. From the figure, the collapse stress is observed to increase with increasing foam density and strain rate, with higher strain rate dependency for open-cell foams when compared to closed-cell foams. In this

paper, it is found that a power-law fit best describes the relationships between elastic modulus and, collapse stress, and strain rate:

$$P(\dot{\epsilon}) = C\dot{\epsilon}^{\alpha} \tag{4.5}$$

where $P(\dot{\epsilon})$ is the measured parameter (elastic modulus or collapse stress), C is the scaling coefficient, $\dot{\epsilon}$ is the strain rate and α is the power-law exponent. The coefficients for all the 3 different densities and other foams in the literature are tabulated in Table 4.5, and determined using a least squares fit. It is to be noted that these coefficients were calculated based on measurements taken for 6 different strain rates along with 3 repeated measurements for each sample at each rate (total 18 tests per density). Generally, from Table 4.5 it is found that the elastic modulus and collapse stress have a scaling exponent of ~ 0.3. This is believed to be associated with the dominant deformation mechanism across these rates, which is believed to be cell wall buckling [135]. In other published literature [46, 106, 113], various models using logarithmic relationships were proposed:

$$P(\dot{\epsilon}) = P(\dot{\epsilon_0})(1 + klog_{10}(\epsilon/\dot{\epsilon_0})) \tag{4.6}$$

where $P(\dot{\epsilon})$ describes the effect of strain rate on various parameters like elastic modulus, collapse stress and energy absorption, k is a constant, and $\dot{\epsilon_0}$ is the reference strain rate. Such relationships have been used to describe both open-cell, and closed-cell foams [46, 106, 113] in the literature but this form did not fit our experimental data and so the power law form was pursued.

Next, to further generalize the pore collapse strength results, a scaling, or normalizing function motivated by previously chosen forms [136] is proposed:

$$\frac{\sigma_{pl}}{E_0} = D\left(\frac{\dot{\epsilon}}{\dot{\epsilon_0}}\right)^{\beta} \tag{4.7}$$

TABLE 4.5: Power-law coefficients for elastic modulus and collapse stress for polymeric foams.

Material	Density (kg/m^3)	Elastic modulus		Collapse stress		Reference
		C	α	C	α	
Poron LD	195	1.06	0.32	0.06	0.29	Current study
Poron MD	244	1.81	0.30	0.11	0.29	Current study
Poron HD	404	4.69	0.34	0.36	0.29	Current study
EPS	61	14.84	0.01	0.90	0.024	Ouellet et al. 2006
EPS	120	22.10	0.08	2.49	0.06	Ouellet et al. 2006
HDPE	80	2.71	0.03	0.64	0.038	Ouellet et al. 2006
HDPE	110	5.08	0.02	1.05	0.03	Ouellet et al. 2006
PU	57	0.91	0.24	1.40	0.11	Koumlis et al. 2019
PU	320	87.68	0.07	5.22	0.09	Tang et al. 2017

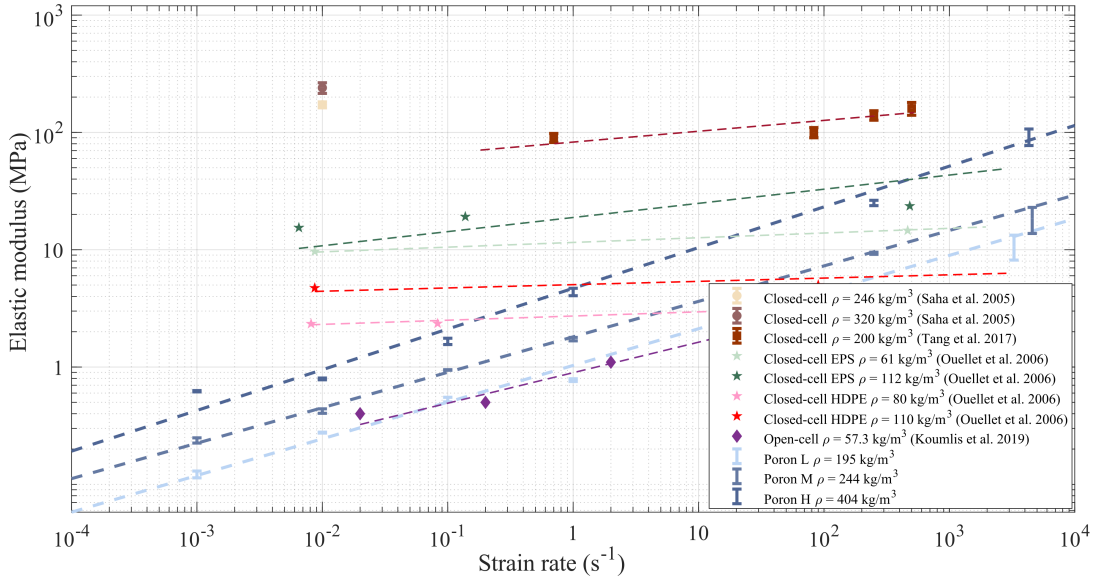

FIGURE 4.8: Trends of elastic modulus of different density foams with varying strain rates under compression loading. Data is ordered based on increasing density for a given study for open-cell foams, followed by closed cell foams. The y axis denotes the elastic modulus (MPa), and the x axis represents strain rate (s^{-1}), and both the axes are represented in a logarithmic scale.

where σ_{pl} (MPa) is the pore collapse stress and D is a scaling coefficient. E_0(MPa) is a characteristic modulus of the foam that is dependent on the dominant deformation mechanism in the material (e.g., buckling [135]). In this case, we take E_0 as the Elastic modulus of the foam at the lowest strain rate in this study, viewed as the characteristic stiffness of the foam. Attempts were made to utilize existing analytical solutions for the Young's modulus of unit cells [40, 131, 137], but sufficient scaling was not achieved, likely a consequence of the oversimplification of a unit cell approach in our foam with spatially distributed pore sizes in both open- and closed-cell configurations. A computational modelling approach with unit cells is likely needed to unravel the solution for E_0.

Next, $\dot{\epsilon_0}(s^{-1})$ is a characteristic strain rate in equation (4.7). This rate is a function of the dominant mechanism over the rates that are being normalized, geometry, and material properties of the foam. The term explicitly accounts for an inherent time scale in the deformation problem. To define this parameter, existing studies in literature have considered timescales associated with damage and deformation mechanisms across varying strain rates. In one study, Deschanel et al. [138] used the timescale associated with rupture during creep tests performed on polyurethane foams. In other studies considering high rate loading conditions such as shock and impact [6, 139, 140], the authors discuss that the critical length and time scales associated with the respective deformation mechanisms depend on both the intrinsic material properties (dependent on sub-scale microstructure) and the inherent flaw distribution [141]. For our foam

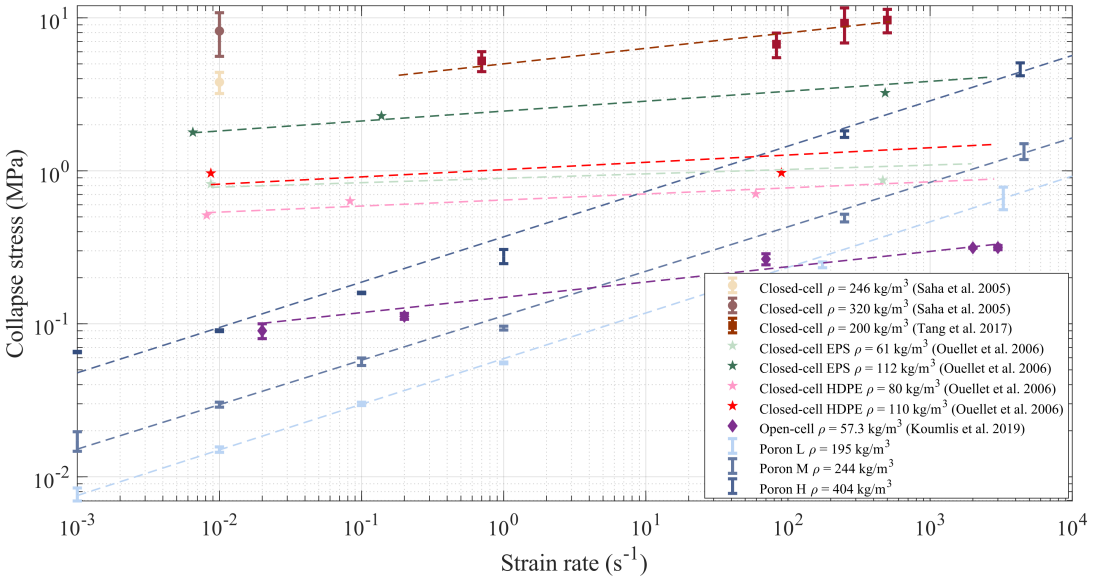

FIGURE 4.9: Figure showing trends of collapse strength of different density foams with varying strain rates under compression loading. Data is ordered based on increasing density for a given study for open-cell foams, followed by closed cell foams. The y axis denotes the collapse stress (MPa) and the x axis represents strain rate (s^{-1}), and both the axes are represented in a logarithmic scale.

materials, to identify a characteristic strain rate, more experiments at even higher strain rate conditions could be performed to guide when transitions between structural buckling (which is believed to dominate across our rates) and material yielding (which is believed to dominate at higher rates [130]). This could be coupled with numerical solutions that take into account geometry,damage, failure, and rate-effects in the base polymer. An analytical solution might be pursued, although these are believed to be to simplistic.

Next, β in equation (4.7) is the power-law coefficient, and this is dependent on the dominant mechanism, geometry, and material properties of the foam. In this study this value is derived from a curve fit ($\beta \sim 0.3$). From Figures 4.8 and 4.9, it is observed that this coefficient is not the same across all materials, and so a first principles solution to this value is likely challenging to generalize.

Finally, shown in Figure 4.10 is the resulting normalized σ_{pl}/E_0 for the three density foams from the present study. Note that the x axis is plotted in strain rate because no sufficient normalizing terms for $\dot{\epsilon_0}$ could be determined. From the figure, it is observed that the normalizing form provides sufficient collapse for the σ_{pl}. These concepts should be extended in the future to other foams to better generalize the approach and determine the coefficients.

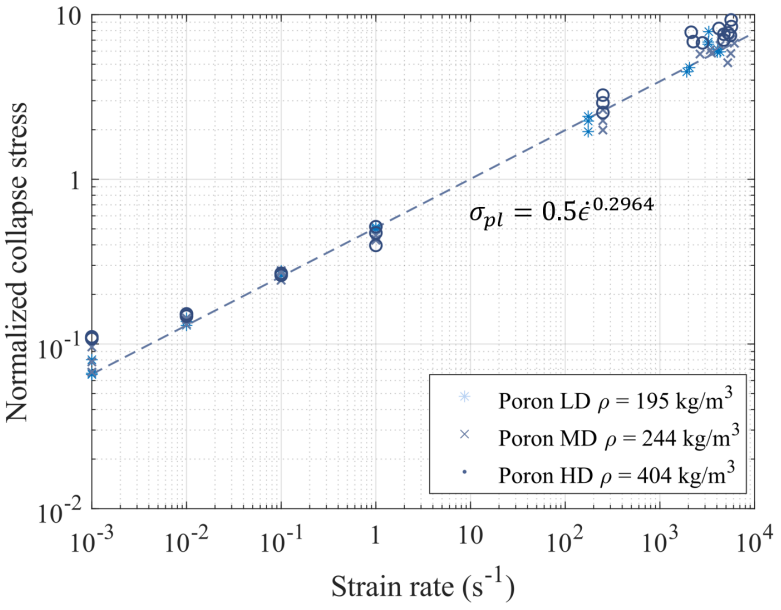

FIGURE 4.10: Figure showing normalized collapse stress of different density foams with varying strain rates under compression loading.

4.5 Conclusion

The effect of density, microstructure and strain-rate on compressive response was explored for an open-cell polyurethane foam with varying densities of $195kg/m^3$, $244kg/m^3$, and $405kg/m^3$. Important microstructural parameters like pores sizes ($5\mu m$ to $145\mu m$) and wall thicknesses ($2\mu m$ to $23\mu m$) have been identified using Micro XCT and image processing techniques. Scaling laws to predict the effects of density and strain rate on collapse stress (σ_{pl}) have been developed. The variation of the foam's characteristic properties (i.e., elastic modulus (E), collapse stress(σ_{pl}), with respect to strain rate are expressed in terms of the characteristic property value at the reference strain rate. These properties are found to behave in a power-law fashion with respect to strain rate. The observations and inferences are supported by stress-strain curves, XCT images of pristine microstructures, and eCDFs of pore sizes and wall thicknesses. The authors believe that the data and curve fits to analytical equations developed in this study will serve as a good starting point for impactful modeling of such materials [17, 40] that predict the effect of microstructure, density, and strain rate on the mechanical response of polymeric foams.

Chapter 5

Density, strain rate and strain effects on mechanical property evolution in polymeric foams

Submitted as **Kapil Bharadwaj B**; Meredith, C; Satapathy, S; Ouellet, S; Romanyk, D; and Hogan, JD. *Phenomenological modelling of rate dependant compressive response of polyurethane foams*, International Journal of Impact Engineering (2021)

Author	**Contribution**
Kapil Bharadwaj B	Conceived the ideas and experimental design of the study; Performed experiments/data collection; Data analysis and interpretation; Primary author (drafted the manuscript)
Meredith, C	Performed experiments/data collection; Methods section - secondary author; Provided revisions to scientific content of manuscript
Satapathy, S	Provided revisions to scientific content of manuscript
Ouellet, S	Provided revisions to scientific content of manuscript
Romanyk, DL	Provided revisions to scientific content of manuscript; Provided access to crucial research equipment
Hogan, JD	Provided revisions to scientific content of manuscript; Provided stylistic/grammatical revisions to manuscript; Principal investigator

5.1 Abstract

A comprehensive experimental study of the evolution of Poisson's ratio and tangent modulus of polymeric foams during rate dependant uniaxial compression is presented.

In this study, polyurethane foams with densities of 195 kg/m^3, 244 kg/m^3, and 405 kg/m^3 obtained from PORON (XRD series) were examined under uniaxial compression loading at strain rates ranging from 0.001 s^{-1} to 5000 s^{-1}. All compression experiments were coupled with a high-speed camera to enable Digital Image Correlation to measure and visualize deformation strains. These measurements enable us to study mechanical property evolution during compression and provide qualitative description of deformation and failure in these materials. A non-linear evolution of Poisson's ratio is observed in-situ in these materials. The compressive stress-strain response is predicted through least square fitting using the Avalle model [20], and model coefficients are found to follow a power-law to scale across strain rates. The stress-strain curves, mechanical property evolution, and scaling coefficients are compared with microstructural parameters of interest such as pore size and wall thickness to inform on deformation mechanisms in the material.

5.2 Introduction

To better exploit the energy absorbing capabilities of foams and design next-generation materials, it is important to understand the effect of stress states and strain rates on their mechanical response through experimental and modelling approaches. In the literature, numerical models [36–39] and finite element models [38, 75, 142, 143] have been developed to predict the mechanical response of cellular polymers. The development of constitutive models [11, 16, 21, 72, 74] enable determination of parameters such as elastic moduli [11, 16], collapse stresses [11], and failure strengths and strains[16], which allow the industry to design better foam materials. In some literature, studies have focused on modelling the yield behavior for polymeric foam materials. For example, Ayyagari et al.[72] define the entire yield surface of a material based on two yield strengths parameters derived from uniaxial compression and uniaxial tension. In a separate study, Deshpande et al.[144] define a multi-axial yield surface to predict plastic yield and elastic buckling behaviour of PVC foams. However, in extreme applications where polymeric foams are used (e.g, helmet liners, armor padding), they are subjected to large strains and high strain rates, where these models cannot be used as they do not predict behavior beyond yield.

In micro-mechanical modeling, elementary physics-based constitutive relations are established for the microstructural behavior. One of the most widely used micromechanical models to predict response of polymeric foams is the Gibson and Ashby model [5] where the porous microstructure is defined in terms of struts and faces. In their study, Gibson and Ashby [5] discuss deformation mechanisms for open-cell foams,

where the elastic limit of the cell is reached when one or more sets of struts yields plastically, buckles, or fractures. Although the Gibson and Ashby model [5] has been widely modified in many other studies [9, 10, 145, 146], three limitations are noted. First, the mechanism-dependant micromechanical model does not consider the effect of strain rate, which has been noted to affect the activated failure mechanisms in polymeric foams [1, 6, 10, 46, 104]. Second, the model assumes idealized and repeated microstructures, which are less common in foams used in most engineering applications [8, 36–40, 128, 131]. Third, the micromechanical model of Gibson and Ashby [5], as well as other micromechanical [5, 23, 28] and phenomenological models [74, 130, 144, 147, 148], assume either no affect of Poisson's ratio (assume $\nu = 0$) or a constant value. In this study, these limitations are addressed through experimental observations utilizing the state-of-the-art in-situ visualization and strain rate dependent phenomenological modelling.

In this paper, the compressive response of porous polymers for a range of densities and strain rates is explored, focusing on the evolution of mechanical properties during deformation (e.g., tangent modulus and Poisson's ratio). The motivation is to better understand fundamental relationships between densities and strain rates on the stress-strain responses, which informs phenomenological modelling of these behaviors. This work builds on previous phenomenological models in the literature [11, 20, 108], including those that consider strain rate effects [46, 106, 113, 149]. Through this work, a better understanding on the combined effects of density, microstructure, and strain rate on the mechanical response of polymeric foams is provided, including notable discoveries on Poisson's ratio evolution and mechanical response. Altogether, phenomenological models and insights developed in this paper can inform the design of new materials [38, 131] and reduce time for desiging these materials when compared with computationally-expensive finite element modelling [20, 38, 128, 150].

5.3 Experimental Methods

5.3.1 Material and Characterization

The materials investigated in this work are open-cell polyurethane foams manufactured by PORON that are used in protection applications such as helmet liners, and armor padding. Three different densities of PORON XRD foams are investigated: a low density foam (LD) of 195 kg/m^3, a medium density foam (MD) of 244 kg/m^3, and a high density foam (HD) of 405 kg/m^3. In this study, polymeric foams are examined under uniaxial compression loading at quasistatic, intermediate, and dynamic strain rates. To ensure

consistency across different strain rates in compression testing, and for microstructure characterization, a single nominal sample diameter of 8 mm was used for all experiments. The sample thickness was restricted by the as-received sheet thickness of 4.2 mm, 3.0 mm, and 3.0 mm for the LD, MD, and HD foams, respectively. The sensitivity of mechanical response to specimen geometry, testing methods, and specimen-size effects are widely discussed in literature [16, 22, 151], and it is expected that some of them manifest in our materials.

For microstructure characterization, synchrotron radiation based microcomputed X−ray tomography (XCT) was performed on the polymeric foam samples at the Biomedical Imaging and Therapy (BMIT) facility − Canadian Light Source (CLS) [95] 05ID−2−SOE−1 hutch, Saskatoon, Canada. Shown in Figure 5.1 are XCT scans of pristine microstructures of the three different density foams. Visually comparing the LD foam on the extreme left to the HD foam on the extreme right in Figure 5.1, distinct differences in microstructural properties (e.g., pore size and wall thickness), and the number of pores are noted. To inform on microstructural metrics, a MATLAB-based program was developed to perform segmentation on the tomograms to calculate pore sizes and wall thicknesses. The detailed algorithm and reconstruction methods used to resolve the microstructural features are discussed by Bhagavathula et al.[152]. Some of the physical and mechanical properties provided by the manufacturer, as well as average pore metrics calculated from reconstruction of the tomograms are listed in Table 5.1.

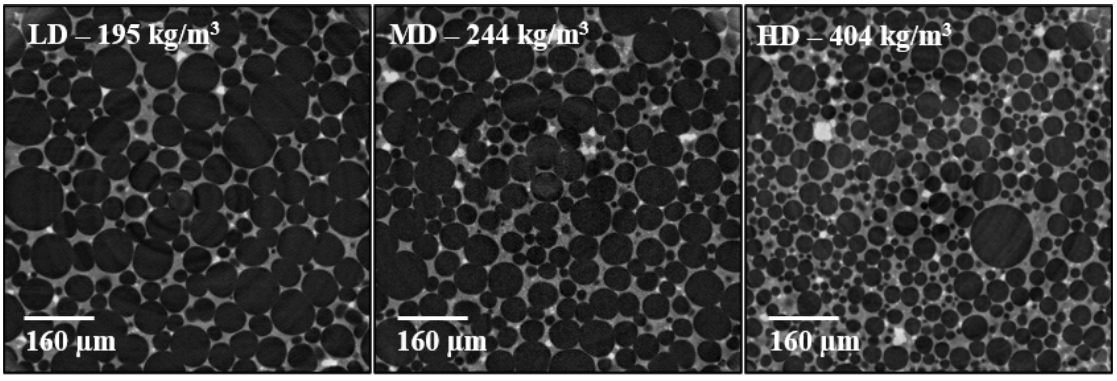

FIGURE 5.1: Pristine microstructures of open-cell polyurethane foams with different densities of 195 kg/m^3 (LD), 244 kg/m^3 (MD), and 405 kg/m^3 (HD) obtained from X-ray tomography scans. The foam material is represented in grey color, and the pore voids are represented by the dark regions.

TABLE 5.1: Physical, microstructure and mechanical properties of PORON foams

2*Property	2*Test method	Material		
		LD	MD	HD
Density (specific gravity)	ASTM D 3574-95 Test A[114]	0.14	0.19	0.4
Compressive strength (kPa)	$0.08s^{-1}$@ 25% deflection	8-23	10-38	69-138
Tear Strength min. (kN/m)	ASTM D 624 Die C[153]	0.8	0.8	2.5
Min. Tensile Elongation (%)	ASTM D 3574 Test E[114]	>145	>145	>145
Tensile Strength, min. (kPa)	ASTM D 3574 Test E[114]	207	310	483
Average pore size (μm)	MATLAB Reconstruction[152]	60 ±55	45 ±35	32 ±30
Average wall thickness (μm)	MATLAB Reconstruction[152]	10 ±9	11 ±10	11 ±10
Average porosity (ϕ)	MATLAB Reconstruction[152]	0.87 ±0.06	0.83 ±0.06	0.76 ±0.05

5.3.2 Mechanical Testing

5.3.3 Quasistatic Compression Experiments

The specimens are tested in uniaxial quasistatic compression at strain rates from 0.001 to 0.1 s^{-1} using an E3000 Instron material testing system. A 3 kN load cell with a background noise corresponding to approximately ±0.01 N recorded the time histories of the forces, and the strains were computed with Digital Image Correlation (discussed later). All quasistatic tests were coupled with a PROMON U750 camera recording at a full resolution of 1280x1024 pixels to visualize deformation features and to perform strain measurements. Both the camera and Instron were set to operate at a sampling rate of 1 frames per second (FPS) for 0.001 s^{-1}, 10 FPS for 0.01 s^{-1}, and 100 FPS for 0.1 s^{-1}. The engineering stresses are calculated by dividing the applied load by the original specimen cross-sectional surface area. Three trials are performed for each density and strain rate to verify repeatability of the material response.

5.3.4 Intermediate Rate Compression Experiments

Intermediate strain rate compression experiments were performed at two strain rates using different loading techniques. The first strain rate, $1s^{-1}$, was performed on an 8871 Instron load frame operating a 1 kN load cell with a background noise corresponding to approximately ±0.01 N. The Instron setup was coupled with a FLIR Grasshopper 3 camera which recorded at 164 FPS. The sample surface was illuminated with a Halogen fiber optic illuminator that ensured good brightness even at high strains. The second intermediate rate was approximately 175 to 250 s^{-1} and utilized a drop tower to reach the necessary strain rates. A PCB 200B04 force sensor with a capacity of 4.45 kN and an upper frequency limit of 75 kHz was attached to a steel base plate, and the sensor had a flat metal loading cap screwed into it that transmitted the force to the quartz sensing

element inside the sensor. The foam sample is placed on the loading cap and a metal tup is positioned above the sample at a height of 25 mm, and dropped to load the sample. The tup is a relatively heavy metal rod ($\sim$4.5 kg) compared to the foams, ensuring that the velocity is nominally constant over the loading time. The drop tower setup was coupled with an iX716 high speed camera recording at 20,000 FPS to measure and visualize deformation. The samples were illuminated with multiple halogen fiber optic illuminators to ensure optimum brightness and contrast throughout the experiment. For the intermediate compression tests, the engineering stresses were calculated by dividing the applied load by the original sample area. At least three tests with the similar loading conditions were performed to verify the repeatability of the material response.

5.3.5 Dynamic Compression Experiments

A modified version of a split-Hopkinson pressure bar (SHPB) apparatus (Kolsky bar) as shown in Figure 5.2 was used to characterize the dynamic compressive response. The Kolsky bar apparatus had a common diameter of 25.4 mm and was made of 6061 aluminum with lengths of 1.2 m and 1 m for the incident and transmission bars, respectively. 160 GSM paper pulse shapers were used to achieve stress/force equilibrium in the specimens. The use of a paper pulse shaper did not change the rise time or shape of input pulse, but helped minimize high frequency noise in the input wave, and helped achieve acceptable force equilibrium [25]. Two strain-gauges are mounted on diametrically opposite sides of the incident and transmission bars via a bridge configuration to record the strain histories during dynamic compression. The strain gages used in the current setup are $350\Omega \pm 0.3\%$ with a gage factor of $2.130 \pm 0.5\%$ (Micro Measurements CEA-13-250UN-350). The transmitted strain histories are amplified and fed to a GEN3i high-speed data recorder with 16-bit resolution recording at $25MHz$ for data capture and visualization, and trigger control. Under stress equilibrium, the transmitted strain history from the transmission bar, $\epsilon_t(t)$, was used to calculate the engineering stress history $\sigma(t)$ in the samples:

$$\sigma(t) = \frac{A_0}{A_s} E_0 \epsilon_t(t) \tag{5.1}$$

where $A_0(m^2)$ and $A_s(m^2)$ are the cross-sectional areas of the bar and sample, respectively, and $E_0(N/m^2)$ is the elastic modulus of the bar material.

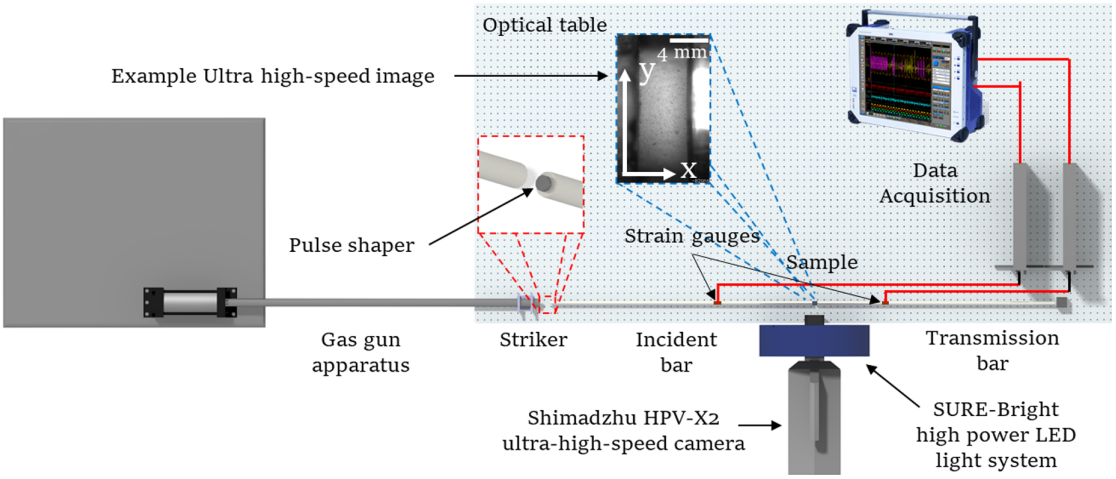

FIGURE 5.2: Modified version of split-Hopkinson Pressure bar apparatus. The arrangement of the ultra-high-speed camera with lens, high power LED light system, and load frame is shown.

In the present study, the dynamic compression experiments were coupled with an ultra-high-speed camera Shimadzu HPV-X2 to visualize deformation features, as well as to perform strain measurements. The camera is able to capture 256 images and is triggered by a split signal from the incident strain-gauge. In these experiments, the camera operated at a frame-rate of 1 million FPS at a resolution of 400x250 pixels. To capture images at such high frame-rates, a SURE-Bright high power LED light system was used to focus an array of light through specialty total internal reflection lenses onto a fixed focal point looking at the specimen. The high intensity continuous light source ensures consistent image quality during acquisition. The camera was triggered from the incident strain-gauge and camera output pulses were used to correlate times between the images and the strain-gauge measurements. The challenges of developing Kolsky bar systems to accurately measure the dynamic response of cellular polymers are well documented in the literature [7, 10, 13, 14, 123], and the testing methods that are pursued in the present study are consistent with recommendations from those in previous studies [10, 25, 113].

5.3.6 Digital Image Correlation (DIC)

In this study, digital image correlation (DIC) was used to measure the strain during experiments. To prepare specimens for DIC analysis, the cylindrical face (orthogonal to the testing axis) is speckle-painted for each specimen. To speckle the specimens, black acrylic ink (Vallejo) is airbrushed (Harder and Steenbeck Infinity airbrush) on the surface to form a speckle pattern for accurate correlation purposes. The VIC-2D 6 software [124] is used for performing DIC analysis on the captured camera images. In DIC analysis, a region of interest (ROI) is manually defined on the speckled surface, and displacements

of all the subsets defined within the ROI are tracked as the specimen deforms during loading. Incremental correlation is used for the large deformations experienced during compression. In each time-step, the subsets in the deformed images are "matched" with the pattern in the previous image using the differences in grey scale intensity levels, at each interpolation point. In each subset, a correlation peak is defined by the interpolation of greyscale levels at or between pixels, and the position of the peak provides a local displacement [125]. The test setup was adjusted for every specimen such that images with good sharpness and exposure were obtained providing an optimal subset size in the VIC-2D 6 software. The DIC parameters are tabulated in Table 5.2.

TABLE 5.2: DIC parameters

Technique	**Quasistatic 2D**	**Intermediate 2D**	**Dynamic 2D**
Pre-filtering	Gaussian	Gaussian	Gaussian
Subset	7	5	1
Step	72	65	31
Correlation criterion	ZNSSD	ZNSSD	ZNSSD
Shape function	Affine	Affine	Affine
Interpolation function	Bicubic Spline	Bicubic Spline	Bicubic Spline
Number of images	∼3000	∼250	128
Pixel to mm conversion	98 px/mm	85 px/mm	48 px/mm
Strain smoothing method	Savitzky-Golay	Savitzky-Golay	Savitzky-Golay

5.4 Experimental Results and Discussion

In this section, the rate-dependent stress-strain response of the three densities of PORON foams is explored. Stress-strain curve-fits based on constitutive equations derived in the literature for polymeric foams [20] are presented, and then detail how these coefficients change as a function of strain rate and density. Then, particular attention is given to tracking the evolution of the mechanical properties during deformation (e.g., tangent modulus and Poisson's ratio).

5.4.1 Uniaxial Compressive Response

Shown in Figure 5.3 is a semi-log plot of the strain rate dependent stress-strain curves for each of the three density foams that were tested. Three trials are performed for each condition, but only one representative curve is shown for clarity (only show a representative curve, but data is used in Figures 5.5, 5.6, 5.7, and 5.8). The maximum strain that is measured during these compression experiments is related to when correlation is lost in the DIC computation. Generally, the curves follow similar elastic, plateau, and densification behaviors as has been noted by others [5, 10, 23, 49]. The elastic modulus and

collapse stress increase with increasing strain rate and foam density, and this is consistent with the literature [7, 10, 113, 128]. Tabulated measurements of the elastic modulus and collapse stress are found in a previous paper by the authors [154] that explores scaling predictions of these values as a function of strain rate and foam density. In this study, more attention is given to fitting stress-strain curves to existing models (next section) and to explore the evolution of their elastic properties, especially Poisson's ratio where there have been limited studies. The comprehensive range of strain rates and densities used in this paper augments previous studies in the literature [1, 2, 7, 10, 22, 46, 49, 113, 129].

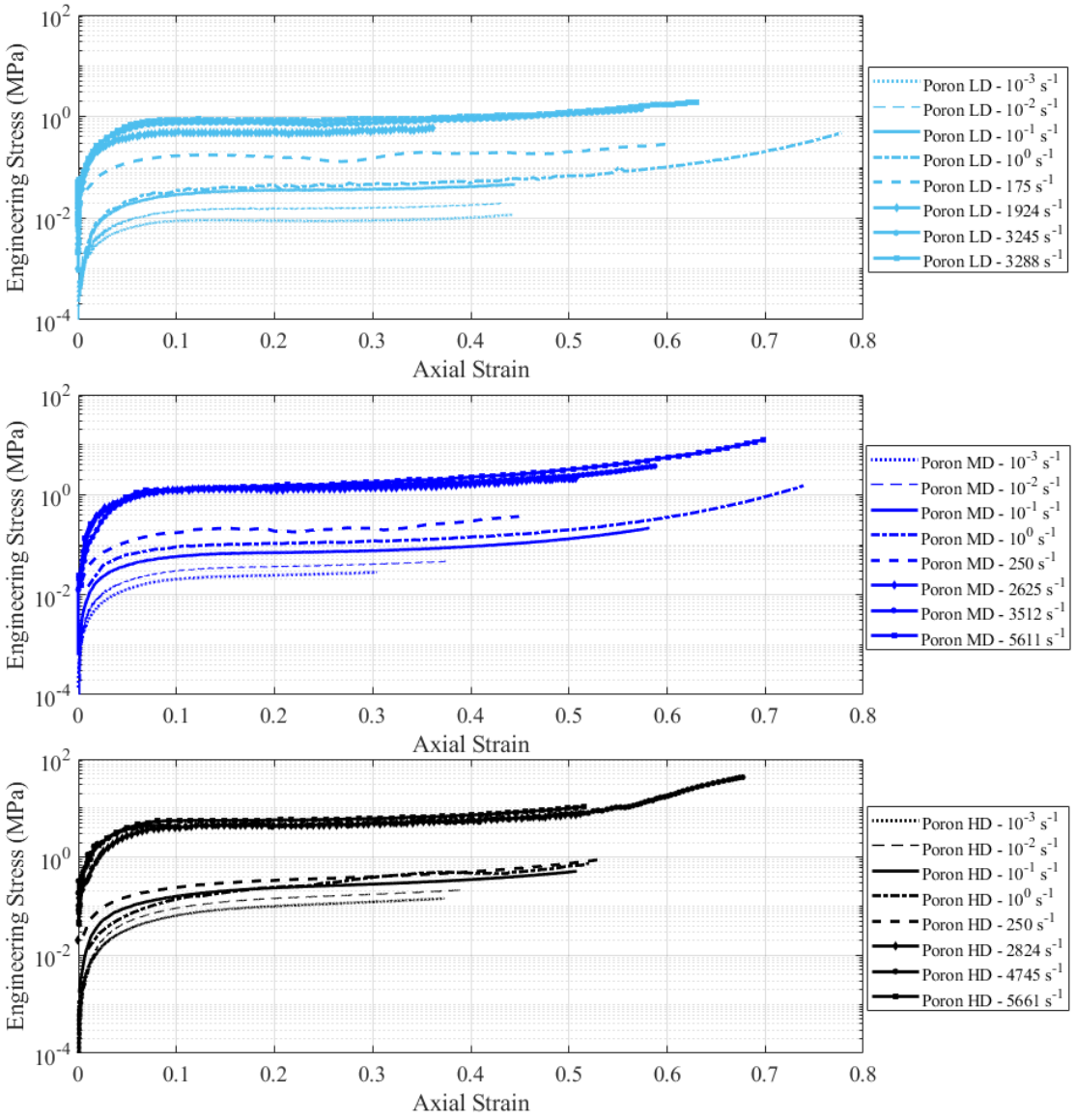

FIGURE 5.3: Experimental results (one representative curve each) for compression tests showing rate effects in PORON foams - (Top) PORON LD foam, (Middle) PORON MD foam, and (Bottom) PORON HD foam. In each sub-figure, the y-axis represents stress in megapascals on a logarithmic scale and the x-axis represents engineering strain.

5.4.2 Parameterization of Constitutive Equation

In this sub-section, least-square fit curve fits are applied on existing phenomenological models [20, 46, 106, 108, 113] to better understand how parameters evolve as a function of strain rate and density, and to discuss the applicability of these models to our data. These models are generally expressed as scalar multiples of a shape function and a modulus function [46, 106, 113, 149]. The shape function, which is usually a function of strain only, represents the stress-strain relationship at a reference strain rate. The modulus function is a function of both strain and strain rate. The modulus function works as a scale factor for the stress-strain curve between the reference strain rate and another strain rate. First, the phenomenological model of Liu and Subhash [108] that was suggested to predict the stress-strain response of polymeric foams. The model has six parameters and is given by:

$$\sigma(\epsilon) = S\frac{e^{s\epsilon} - 1}{Q + e^{q\epsilon}} + e^{R}(e^{r\epsilon} - 1) \tag{5.2}$$

where S, Q, R, s, q and r are empirically fit coefficients from the experimental data. The second model that is explored accounts for strain rate dependency [46, 106, 113], where various models using logarithmic relationships were proposed:

$$P(\dot{\epsilon}) = P(\dot{\epsilon_0})(1 + klog_{10}(\dot{\epsilon}/\dot{\epsilon_0})) \tag{5.3}$$

where $P(\dot{\epsilon})$ describes the effect of strain rate on various parameters like elastic modulus, collapse stress and energy absorption, k is a constant, and $\dot{\epsilon_0}$ is the reference strain rate. Such relationships have been used to describe both open-cell, and closed-cell foams [46, 106, 113] in the literature. It was found that models described in equations 5.2 and 5.3, and similar variations [46, 106, 108, 113] did not fit our data well in terms of under-predicting yield region at high strain rates, and over-predicting densification at lower strain rates. In another study, Avalle et al. [20] proposed a five parameter model which was found to fit our data in all regimes for all strain rates studied in this paper:

$$\sigma(\epsilon) = A(1 - e^{(E/A)\epsilon(1-\epsilon)^m}) + B\left(\frac{\epsilon}{1-\epsilon}\right)^n \tag{5.4}$$

where the parameters A, E, B, m, and n are empirical parameters. An example of a typical curve fit applied to a medium density foam at a strain rate of 100 s^{-1} and a high density foam at a strain rate of 2255 s^{-1} is shown in Figure 5.4; it is noted that the model fits the data well for these and all other density and rate combinations studied in this paper. Here, parameter A controls the magnitude of the plateau stress and can

TABLE 5.3: Model coefficients for three density PORON foams for scaling across strain rates

	PORON LD		PORON MD		PORON HD	
	C	α	C	α	C	α
A	0.06	0.28	0.12	0.26	0.48	0.22
E	0.89	0.31	2.05	0.3	4.58	0.31
B	0.04	0.23	0.12	0.21	0.41	0.18
n	2.98	-0.074	2.83	-0.027	2.81	-0.006
	M_1	M_2	M_1	M_2	M_1	M_2
m	-0.26	-2.24	-0.17	-1.98	-0.15	-1.13

only have a positive value. Parameter E controls the slope of the elastic region and can only be a positive value. Parameter m controls the curvature at yield and can be both positive and negative. Parameter B controls the magnitude of the densification stress and can only be a positive value. Parameter n controls the slope of the densification region and can only be a positive value. Figure 5.5 shows the variation of these empirical parameters as a function of strain rate for a given density foam material. It is found that parameters A, E, B, and n are density dependent and appear to scale across strain rate using a power-law relationship as follows:

$$P(\dot{\epsilon}) = C\dot{\epsilon}^{\alpha} \tag{5.5}$$

where $P(\dot{\epsilon})$ is the measured parameter (A, E, B, and n), C is the scaling coefficient, $\dot{\epsilon}$ is the strain rate and α is the power-law exponent. The coefficient m is found to scale via a logarithmic relationship:

$$m = M_1 log(\dot{\epsilon}) + M_2 \tag{5.6}$$

where M_1 and M_2 are empirical parameters. The coefficients for all the three different densities are tabulated in Table 5.3, and are determined using a least squares fit. From Table 5.3, it is observed for A and B that the power-law exponent decreases for increasing density, which tells us that lower density materials are prone to higher strain rate effects for the plateau and densification stress magnitudes [138]. For coefficient E, it is observed that the power-law exponent remains consistent throughout the densities suggesting that a single mechanism dominates the elastic response in these materials. This result is in a good agreement with experimental data [140, 155]. Finally, for coefficient n, it is observed that the power-law exponent increases for increasing densities, suggesting that rate of densification is dependant on material density [2, 106].

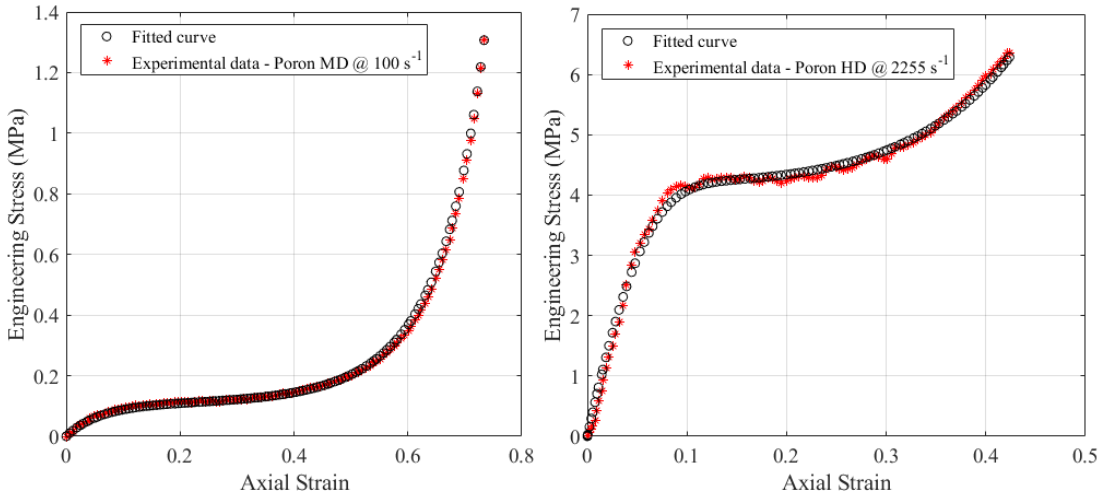

FIGURE 5.4: An example of a typical curve fit: (Left) Medium density PORON at a strain rate of 100 s^{-1}, (Right) High density PORON at a strain rate of 2255 s^{-1}.

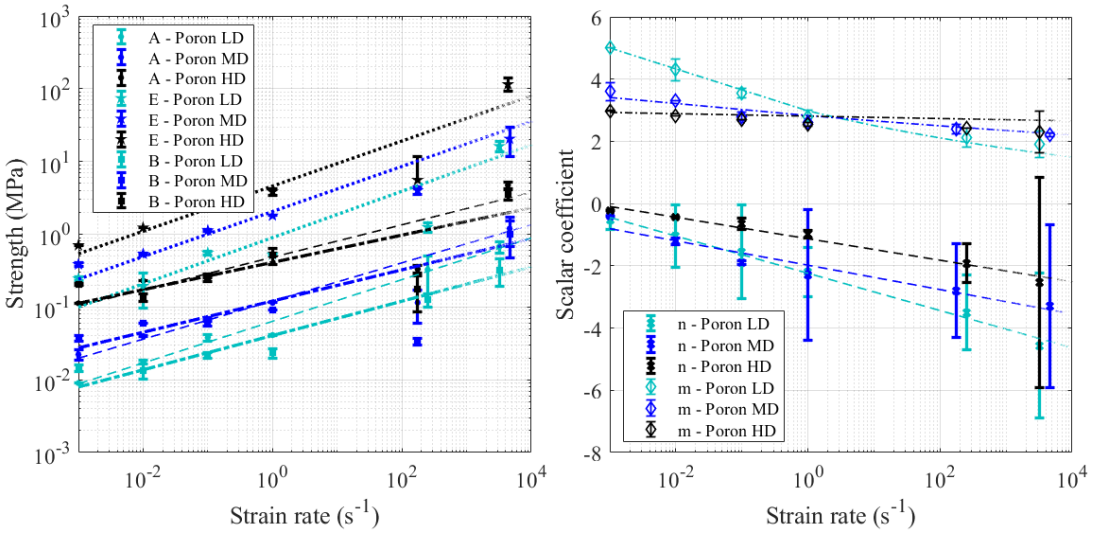

FIGURE 5.5: Trends of model coefficients across varying strain rate for PORON foams (Left) Variation of coefficients A, E and B, (Right) Variation of coefficients n and m

5.4.3 Evolution of Tangent Modulus

Next, the evolution of the tangent modulus as a function of strain for the different strain rates and densities is investigated (Figure 5.6). The evolution of the tangent modulus to probe and compare transitional behaviors across the different densities and strain rates is studied. Through these comparisons, a better understanding of deformation mechanisms in the structure and base material during these experiments. In Figure 5.6, the tangent modulus is computed by using a moving average window filter applied to the stress-strain curves. For the quasi-static experiments, the tangent modulus was averaged over windows of 0.005 to 0.08 strain in size, depending on the number of points and resulting smoothness. For the intermediate strain rate experiments, the tangent modulus was

averaged over windows of 0.005 to 0.06 strain. For dynamic strain rates, the tangent modulus was averaged over windows of 0.005 to 0.04 strain. As the strain rate was increased, there were fewer data points to average over, and our choice for the window was influenced by the number of points, range of elastic strain for different strain rates, smoothness of resultant curve, and desire to capture the proper trends and magnitudes. Note that the initial tangent modulus computed through strain-averaged windowing is not necessarily the same value of E that was determined in Figure 5.5.

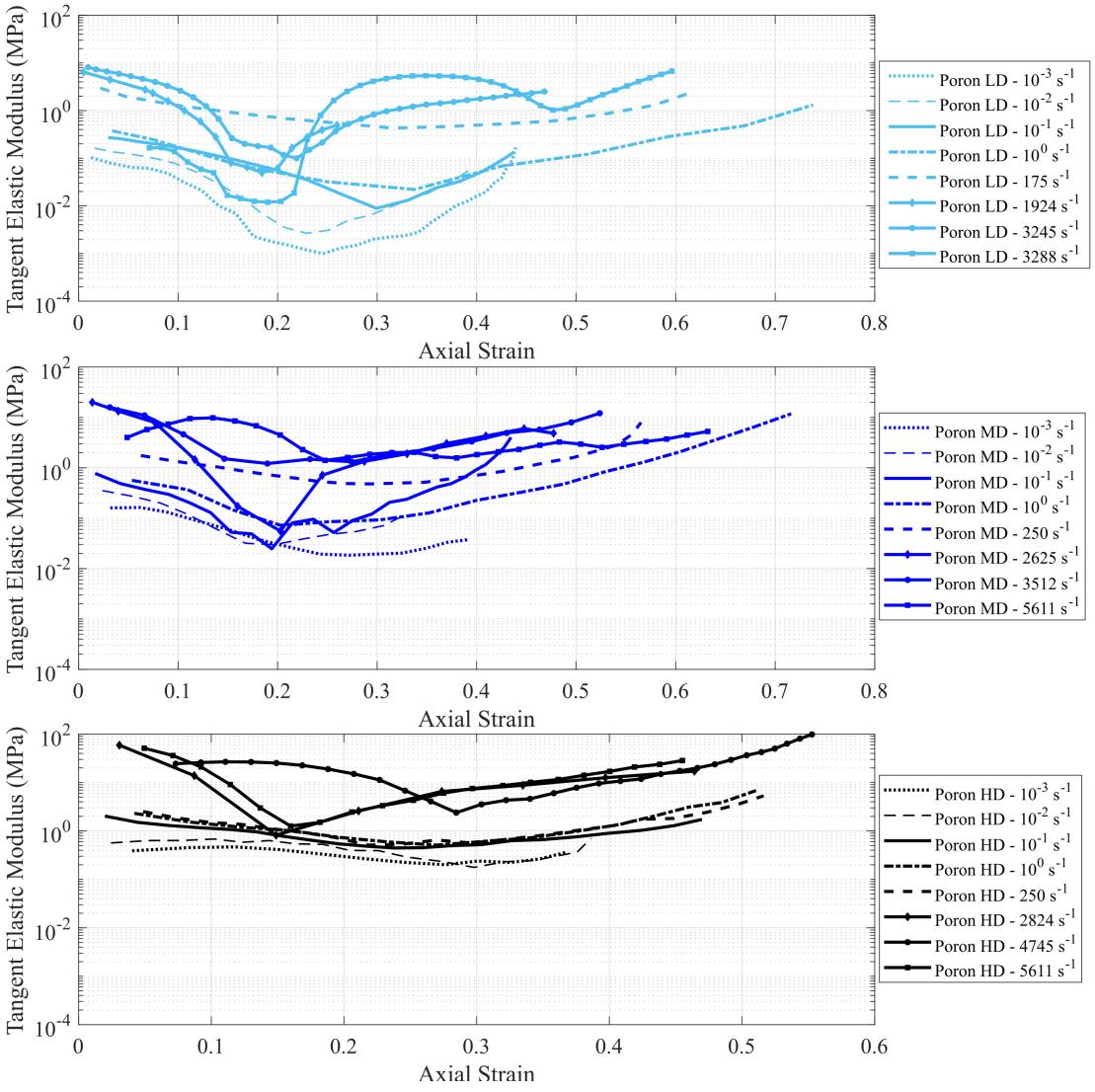

FIGURE 5.6: Evolution of tangent modulus as a function of strain for varying strain rates - (Top) PORON LD foam, (Middle) PORON MD foam, and (Bottom) PORON HD foam.

From Figure 5.6, it is observed that the initial tangent modulus in the elastic regime increase as a function of strain rate and density. In general, the tangent modulus magnitude decreases for increasing strain, with greater sensitivities for higher rates and densities. For all tests, the tangent modulus decreases from its initial value 0 until between 0.2 to

0.3 strain, after which strain it begins to increase. The decrease is likely associated with pore collapse [46, 156, 157], while the increase is likely associated with the onset of cell locking [138, 157]. The relationships between the rate of densification and the density and strain rate were explored previously in evaluating n in Figure 5.5. This transition behavior is more pronounced at higher rates. The lowest point on the curve shifts to the left for increasing strain rate, suggesting the onset of cell locking occurs earlier under higher strain rates, with no obvious density effects noted for the materials studied here. This rate-dependent behavior of transitions happening at lower strains (to the right) is likely related to the cell edges having less time to "rearrange" and avoid locking [10, 158], and these trends are consistent with those predicted by previous studies in the literature [157, 159]. Overall from the tangent modulus curves, it is observed that there is no strain range over which the modulus is constant. It is therefore recommended that the tangent modulus should be determined by averaging the measurements from post-zero strain to strains larger than the pore collapse initiation strain, and use this value to represent the elastic modulus of a cellular foam material.

5.4.4 Evolution of Poisson's Ratio

Finally, the evolution of the Poisson's ratio as a function of strain for the different densities and strain rates is explored (Figure 5.7). Previous studies have assumed a value of zero [5, 23, 28, 144] or have assumed a constant value for Poisson's ratio in their models [74, 130, 147, 148] , whereas utilization of DIC in this paper enables in-situ evolutions to be tracked. In Figure 5.7, it is shown that Poisson's ratio evolves in a non-monotonic and non-linear manner. For Poisson's ratio, the values generally *increase* in the elastic regime until yield. For increasing density, there is no obvious trend in how fast the Poisson's ratio increases. The density- and rate-dependent trends in Poisson's ratio are summarized for the elastic regime in Figure 5.8, which shows that the Poisson's ratio in the elastic regime decreases as a function of strain rate for this current study, with no correlations observed as a function of density. Discussion is, thus, turned back to Figure 5.7.

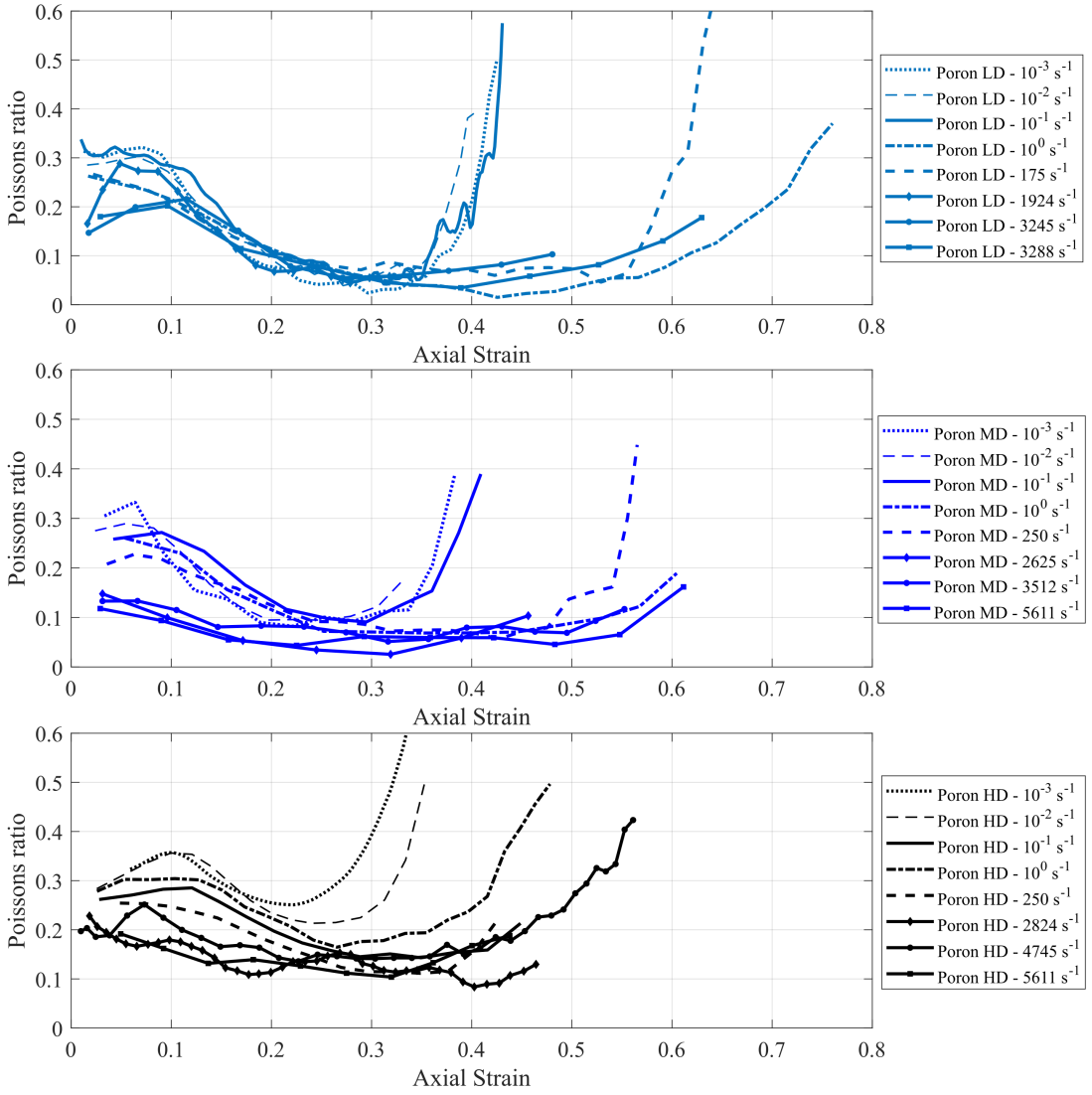

FIGURE 5.7: Evolution of Poisson's ratio as a function of strain for varying strain rates - (Top) PORON LD foam, (Middle) PORON MD foam, and (Bottom) PORON HD foam.

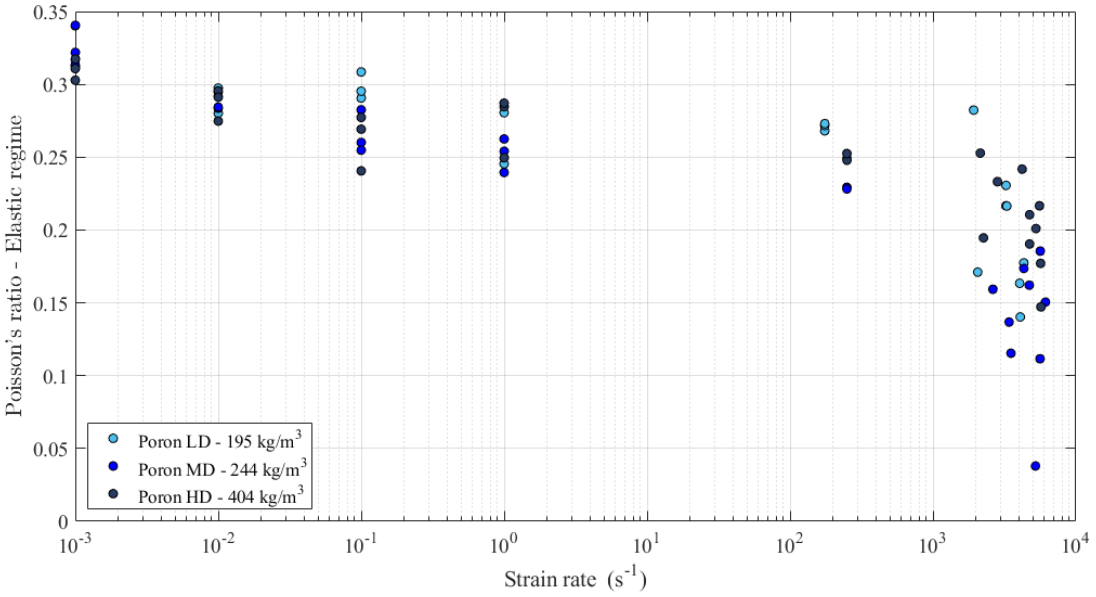

FIGURE 5.8: Variation of the measured Poisson's ratio in the elastic regime under uniaxial compressive loading across varying strain rates for PORON foams of noted densities.

In the elastic regime, it is observed from Figure 5.7 that Poisson's ratio increases until yield for all materials. The yield limit is observed to shift towards right as density increases up to strains of 0.1 to 0.15. Post-yield and until strains between 0.2 and 0.3, the Poisson's ratio decrease for increasing strain. This is likely related to pore collapse in the material. There is no correlation between density and the value of Poisson's ratio at the lowest points in the Poisson's ratio-strain curves. For increasing strain rate, the rate of decreases in the Poisson's ratio appears to be faster. After decreasing until strains of 0.2 to 0.3, the Poisson's ratio then begins to increase, indicating the onset of pore locking [36, 128]. The strain value at which pore locking occurs shifts to the right for increasing strain rate, indicating that densification may happen later for increasing strain rate. This trend is converse to what was observed in the evolution of the tangent modulus as a function of strain (Figure 5.6). This highlights the strain rate dependent competition between continued pore collapse that serves to softens the material (captured by Poisson's ratio in Figure 5.7) and stiffening brought on by cell locking (captured by the tangent modulus in Figure 5.6). Finally during densification, the rate of increase and magnitude in the Poisson's ratio is greater for higher density foams.

Overall from curves in Figures 5.6 and 5.7, it is observed that the minima of tangent modulus happens before minima in Poisson's ratio curves as the stress (manifested in tangent modulus curves) is a precursor to structural deformation (manifested in Poisson's ratio curves). Stated more directly, the stress change always happens before the structure deforms [128]. Minima in tangent modulus curves happens at earlier strains and higher

values for increasing strain rate, which corresponds to the structure becoming stiffer for higher rates [7, 46]. Minima in the Poisson's ratio curves happens at higher strains, meaning there is a delay in the onset of structural deformation as rate increases. At high strain rates, tangent modulus and Poisson's ratio evolution is observed to be complex as a consequence of sensitivity of mechanical response to specimen geometry, testing methods, and specimen-size effects as widely discussed in literature [3, 148, 151]. In one study, Sun et al. [157] discuss that the elastic modulus is expected to reduce prior to cell collapse as the cell walls bend and buckle, and this phenomenon is observed in-situ in the present study. This strain rate-dependent response is likely related to an inter-play between structural stiffening, pore sizes that are interrogated, and mechanical properties. This inter-play also manifests as differences in increasing/decreasing trends observed in Figures 5.6 and 5.7 as a function of strain, strain rate, and density [16, 22, 151]. This highlights the physical implications for the role of microstructure and density on the evolution of mechanical properties for polymeric foams. These concepts can be extended in the future to other foams to better generalize the approach and determine the model coefficients. In the future, the data presented in this paper can be modeled via first principle approaches [143, 156, 160] to fully develop a strain rate-dependant constitutive model, but it is not done here because it is more impactful when multiple stress-state experiments are performed.

5.5 Conclusion

In this study, polyurethane foams of three different densities (195 kg/m^3, 244 kg/m^3, 405 kg/m^3) obtained from PORON were examined under uniaxial compression loading at varying strain rates from 0.001 s^1 to 5000 s^1. All compression experiments were coupled with a high-speed camera to measure and visualize deformation. Digital image correlation was performed to obtain deformation and mechanical property evolution characteristics (e.g., tangent modulus and Poisson's ratio). The rate dependent compressive response was fit to the Avalle model [20] and model coefficients were found to follow a power-law. Evolution of deformation is studied in terms of in-situ measurements of tangent modulus and Poisson's ratio. Overall, this study addresses some of the limitations that are noted in literature such as lack of consideration for the effect of strain rate, and the effect of Poisson's ratio during loading. In this study, this gap is addressed by investigating mechanical properties and failure behavior for a wide range of strain rates alongside comparing with microstructure properties. These kind of in-situ measurements are shown for the first time and these measurements are motivated by looking at the evolution of these properties to learn about transitional behaviours. This study also provides a comprehensive set of data to better populate experimental data across varying

densities and strain rates, provide data to models, recognize many modeling methods and resources to parameterize the models.

Chapter 6

Comparison between D3O and PORON polyurethane foams as prospective helmet liner materials

In this final chapter, results and observations are linked across each of the polymeric foam materials studied in this thesis. We focus on comparing pore structures (e.g., size, wall thickness), chemical characterizations, strain-rate dependent stress-strain responses, deformation behaviors, and some key scalar mechanical properties (e.g., modulus and collapse stress). These enable us to gain insights into the effects of microstructural features (e.g., pore size and wall thickness), foam density, and strain rate on the mechanical response of polymeric foams. Altogether, results in this thesis demonstrate that not all polymeric foam materials follow ordered trends and can be described by the same model forms, and these are consequence of their pore morphologies, densities, base mechanical properties, and strain rate-dependencies of these characteristics; this is not surprising but should still be noted.

6.1 Microstructure Characterization

For microstructure characterization, synchrotron radiation based X−ray microtomography was performed on the polymeric foam samples at the Biomedical Imaging and Therapy (BMIT) facility − Canadian Light Source (CLS)[95] 05ID−2 − SOE−1 hutch, Saskatoon. Shown in Figure 6.1 are XCT scans of pristine microstructures of the three different density PORON foams (open-cell) and two variants of shear thickening foams from D3O (partially open/closed-cell); materials and densities are identified in the subfigures and captions and it should be noted that the "D3O Liner" is being shown for

the first time. For the PORON foams, visually comparing the LD foam on the extreme Left to the HD foam on the extreme Right, distinct differences in microstructural features (e.g., pore size and wall thickness), and the number of pores are noted. When compared to the D3O LITE D material, the D3O Liner material appears to have different microstructures along with different pore sizes and wall thicknesses, and the cell morphology and topology also appear to be different. However, it is observed that D3O Liner material has a similar pore morphology to that of the PORON foams with spherical pores.

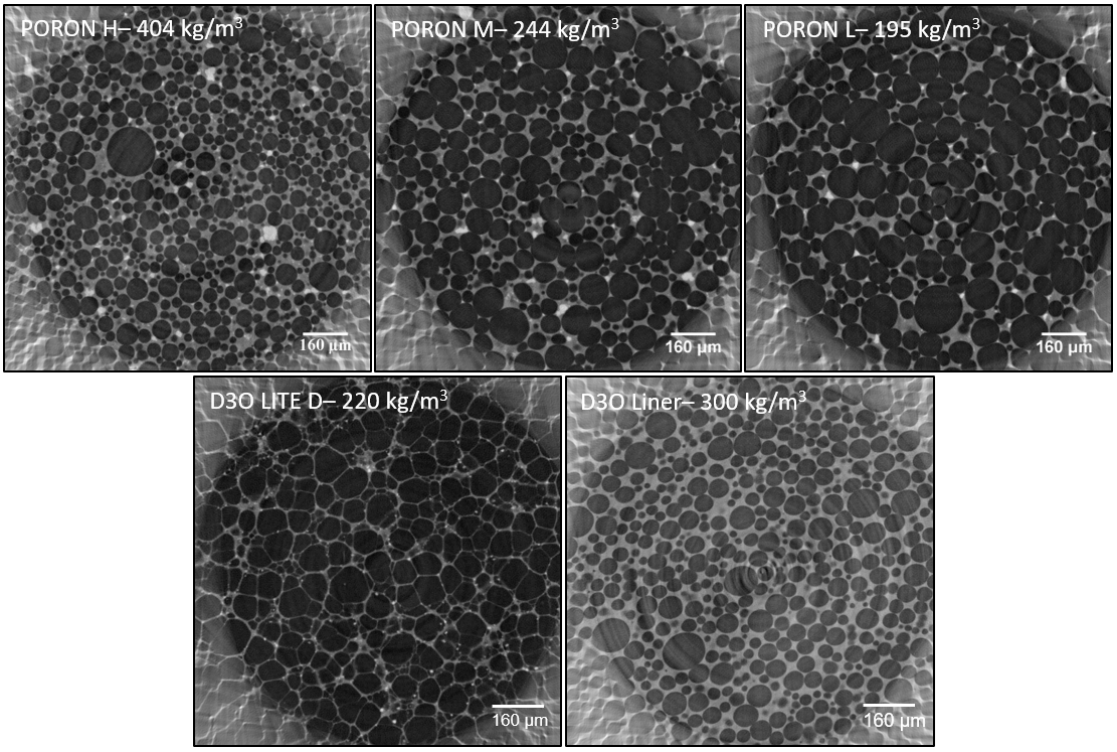

FIGURE 6.1: (Top) Left to Right - XCT scans of pristine microstructures of PORON H, PORON M, PORON L. (Bottom) Left to Right - XCT images showing pores and additive particles (bRight features) in the pristine microstructures of D3O LITE D (Left) and D3O Liner (Right) foam materials with scale bars shown on the bottom-Right of the image.

To inform on microstructural metrics, a MATLAB-based program published in Chapter 3 [152] is developed to perform segmentation on the tomograms to calculate pore sizes and wall thicknesses in the x and y planes of the scans. The z-plane is not included because it was similar to those measurements in the x-plane. Pores with sizes less than $250\mu m$ and wall thickness sizes less than $50\mu m$ were considered for measurements based on visual confirmation from the XCT scans (Figure 6.1). It is to be noted that the variability in measurements is determined by the threshold limits from the reconstruction. Results are shown in Figure 6.2 for the pore diameter (Left) and wall thickness (Right) for all

foam materials. Shown in Figure 6.2 (Left) are the ECDFs which are used to identify the likely range of the pore sizes and trends. From Figure 6.2 (Left), it is observed that the D3O Lite D has smaller pore sizes, with median pore sizes of $20\mu m$ for the D3O Lite D foam and $25\mu m$ for the D3O Liner. By looking at the values between the 10^{th} and 90^{th} percentiles, this range is projected to be between $12\mu m$ and $50\,um$ in both x and y directions for the D3O LITE D, and between $13\mu m$ and $62\mu m$ in both x and y directions for the D3O Liner material. For the low density PORON foam, the limits lie between $5-114\mu m$ for the x, and $6-142\mu m$ for the y directions. For the medium density PORON foam, the limits lie between $6-100\mu m$, and $8-110\mu m$ for the x and y directions, respectively. For the high density PORON foam, the pore sizes are found to be near spherical in nature with limits ranging from $5-75\mu m$ for both x and y directions. Generally for both the PORON and D3O foams, the pore size ECDF shifts to the Right as the density decreases indicating that pore sizes are larger in the lower density foams. The ECDFs also reveal that for a given PORON foam, the pore size for D_x is slightly greater than D_y; and for a given D3O foam, the pore size for D_y is slightly greater than D_x and this is likely a consequence of the foaming direction during the manufacturing process.

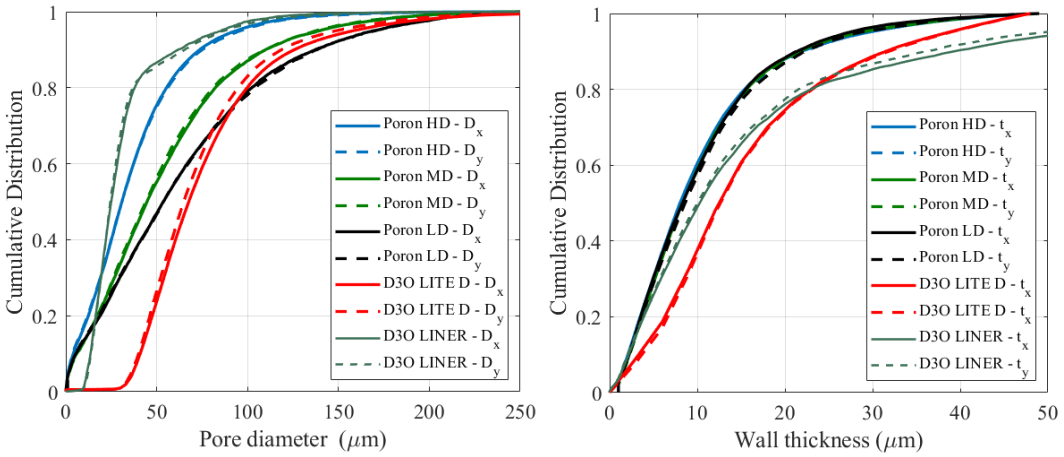

FIGURE 6.2: (Left) Pore size ECDFs of PORON and D3O foams, D_x and D_y represent the pore diameters in x and y directions, respectively. (Right) Wall thickness ECDFs of PORON foams, T_x and T_y represent the wall thicknesses in x and y directions, respectively.

Shown in figure on the right (Figure 6.2) are the ECDFs of the wall thicknesses. In the figure, T_x and T_y represent the wall thicknesses in x and y directions respectively. For the PORON foams, the wall thickness range is measured to be between $2\mu m$ and $23\mu m$ in both x and y directions for the pristine specimens, and it is is observed that profiles of T_x and T_y are similar for all the different density foams. For the D3O foams, the wall thicknesses in the D3O LITE D are greater than the D3O liner, with median values of

$10\mu m$ for the D3O Lite D foam and $6\mu m$ for the D3O Liner. For both materials, the pore sizes and wall thickness appear to be independent of orientation. Overall from the wall thickness ECDFs, it is observed that profiles of T_x and T_y are similar for all the foams, therefore the influence of pore morphology on mechanical response stems from differences in pore sizes.

To summarize the microstructural feature results, shown in Table 6.1 are the pore metrics calculated from characterization of all the foam materials studied in this thesis. The first column shows the type of foam, followed by density, and the as-received sheet thicknesses. The table also shows the average pore size, average wall thickness, and average porosity (ϕ) for all foams.

TABLE 6.1: Microstucture characterization pore metrics of D3O and PORON foams

Type	Density (kg/m^3)	Foam thickness (mm)	Average pore size (μm)	Average wall thickness (μm)	Average porosity (ϕ)
PORON LD	195	4.2	60 ± 55	10 ± 9	0.87 ± 0.06
PORON MD	244	3	45 ± 35	11 ± 10	0.83 ± 0.06
PORON HD	404	3	32 ± 30	11 ± 10	0.76 ± 0.05
D3O LITE D	220	4.2	31 ± 30	10 ± 4	0.83 ± 0.05
D3O Liner	300	3	38 ± 32	6 ± 3	0.79 ± 0.06

6.2 Chemical Characterization

FTIR spectroscopy was used to inform about the chemical constituents and to obtain some basic information regarding the configuration of the macromolecules present in the polymeric foam materials. Shown on the top in Figure 6.3 is the Infrared spectra obtained for the D3O LITE D foam. The IR spectroscopy frequency ranges and absorptions for functional groups are identified from the Sigma-Aldrich IR spectrum table [161]. Based on the characteristic IR absorption bands of functional groups, the evaluations of each peak are carried out. The D3O LITE D material has two large peaks present around $2800cm^{-1}$ that resemble a polyethylene signature, as well as a small peak around $750cm^{-1}$ and a peak around $1500cm^{-1}$, all corresponding to a polyethylene-based monomer. Shown in the middle in Figure 6.3 is the Infrared (IR) spectra obtained for the D3O Liner foam. For the D3O Liner material, the small sharper peak just before $3000cm^{-1}$ corresponds to a PDMS type structure and the peak around the $3300cm^{-1}$ corresponds to a N-H stretch in a polyurethane-based monomer. Based on the evaluations of the peaks, the possibilities of functional groups for D3O LITE D are -CH2, -CH3, -C-O or =C-O-C, and the possibilities for D3O LINER are -CH2, -CH3, -C=O, O=C-O-C, -NH. Finally, shown on the bottom in Figure 6.3 is the Infrared (IR) spectra obtained for the PORON HD foam. For the PORON foam, the absorption band at

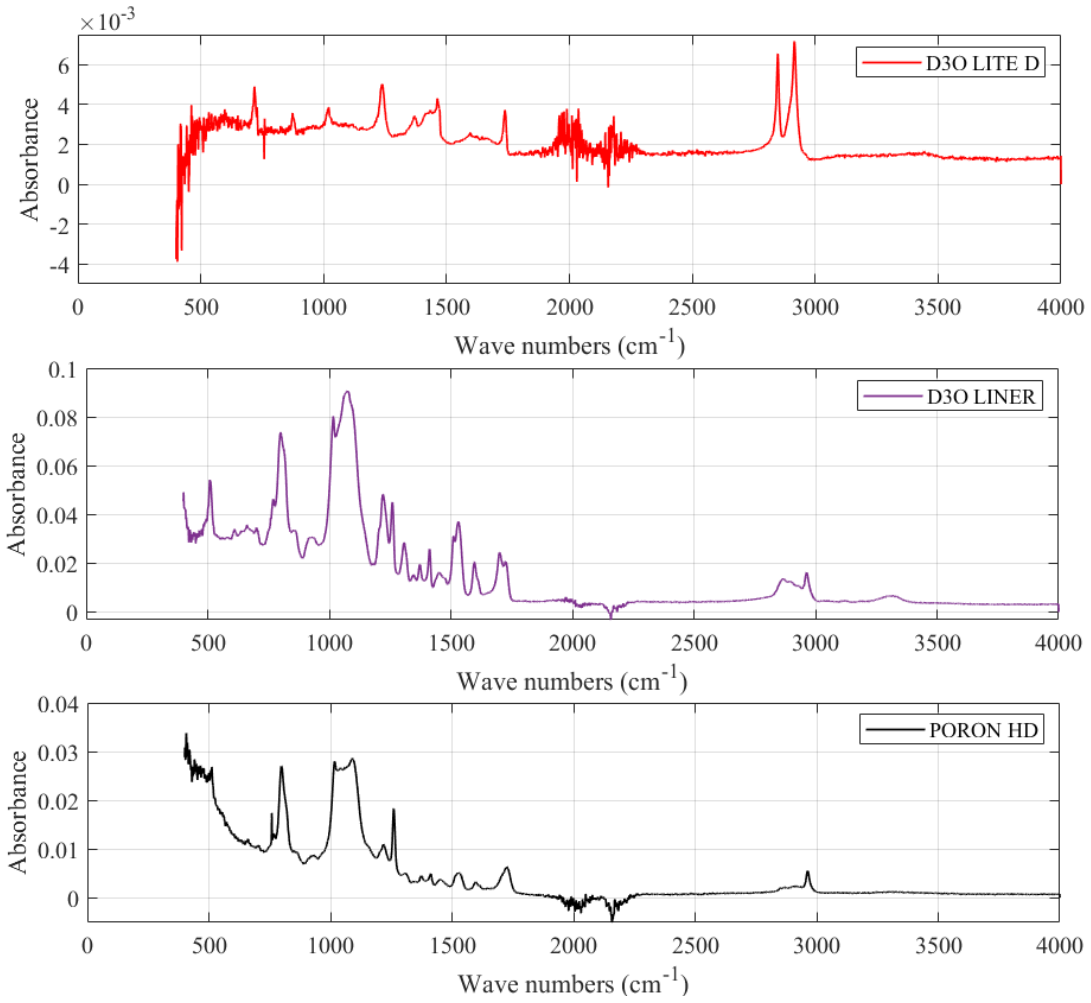

FIGURE 6.3: (Top) Infrared spectra obtained for the D3O LITE D foam. (Middle) Infrared spectra obtained for the D3O Liner foam. (Bottom) Infrared spectra obtained for the PORON HD foam.

$1730cm^{-1}$ is associated with a C=O group in polyurethane. The group of NH vibrations is identified by the bands at $1540cm^{-1}$. It is found that all PORON foam have a similar chemical composition and thus, are not shown for brevity.

6.3 Compressive Response

Typical stress-strain curves for open-cell polymeric foams in the literature [7, 10–12, 16, 23, 106] show three stages of deformation: *elastic behavior* up to collapse stress, *plateau*, and *densification*. For cellular materials, elastic behavior up to pore collapse is controlled by the elastic bending of the cell walls, followed by plastic bending [106]. After cell-walls bend plastically, collapsing of the cell occurs and this usually manifests as the *plateau* stress. The linear plateau regime is associated with a combination of cell wall bending and cell wall collapse [10, 11, 23]. After most of the cells have collapsed and opposite

cell-walls in a given pore begin to touch each other, further compressive strain results in a rapid rise in the stress, and this is known as *densification*. During densification, the porosity of the foam is crushed out and the foam material tends to behave as a solid polymer.

6.3.1 PORON Foams

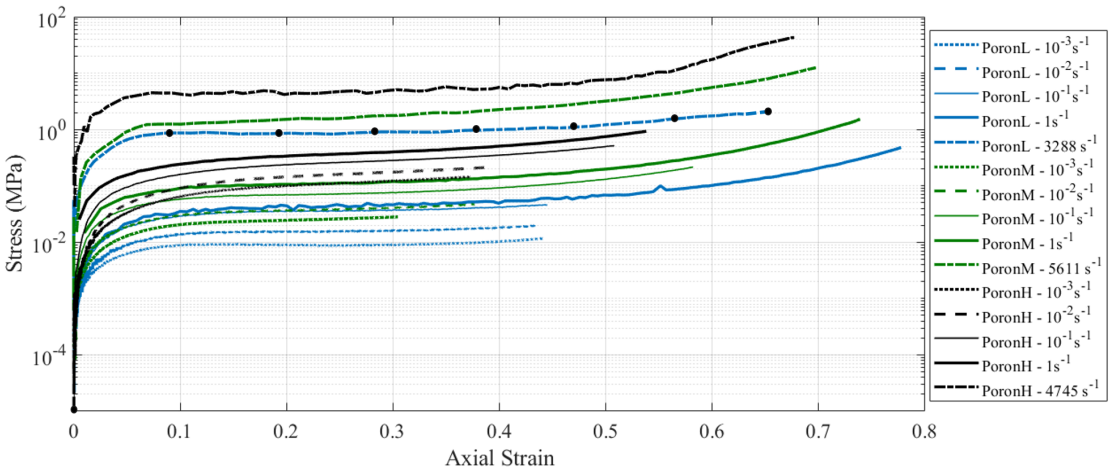

FIGURE 6.4: Stress-strain curves of PORON foams under uniaxial compression from strain-rates ranging from 0.001 to $\sim 5700s^{-1}$. Black points on the PORON LD dynamic curve are represented by ultra-high-speed camera images shown later in Figure 6.5.

From Figure 6.4, it is observed that the compressive response of the PORON foams in all the strain rate regimes exhibit a typical elastomeric foam behavior with some minor differences. Namely, typical foam responses have a sudden change in slope when the stress reaches the elastic stress limit and its value is easily identifiable [16, 22, 46]. For all the different densities, it was found that there was a gradual transition from the elastic regime to the plateau regime beginning at a strain of ~ 0.02 and plateauing at approximately 0.08 strain, which marks the range of yield strain for this material. Polymeric foams have a pore collapse stress (σ_{pl}, stress at 0.25 strain in these materials) which represent the stress when foams start to deform post elastic limit when loaded beyond the linear-elastic regime. The collapse of the pore structures gives a long, approximately horizontal plateau to the stress-strain response, where the strain is partially recoverable and some permanent deformation is observed to the foam microstructure post-experiment.

Shown in Figure 6.5 are the time-evolved dynamic compression failure images of the PORON LD foam. From the images, uniform compression is observed with no large scale deformation features in the ultra-high-speed images.

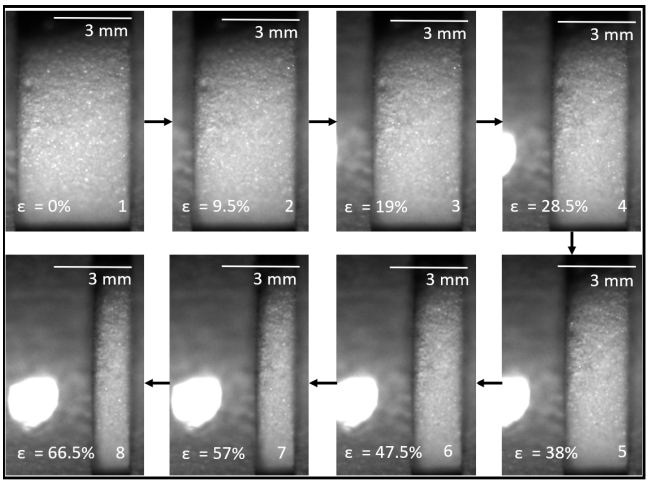

FIGURE 6.5: Time-evolved dynamic compression failure of the PORON LD foam at 4560 s^{-1} using a split-Hopkinson Pressure Bar apparatus. Inter-frame strains are denoted at the bottom-Left corner of each image and specimen length scales are denoted on the top-Right corner of each image.

6.3.2 D3O - Shear Thickening Foams

Shown in Figure 6.6 are the stress-strain curves for both D3O materials (Liner and Lite D), and one representative curve is shown for each experimental condition. It is to be noted that multiple tests were conducted under similar loading conditions for repeatability. Looking at the stress-strain curves, it is observed that with increasing strain rate, an apparent increase in stiffness and plastic collapse strength is observed for the LITE D foam, whereas no clear trends are observed for the Liner material. More notably for both D3O foams, two distinct densification regimes are observed under dynamic uniaxial compression.

Figure 6.7 shows the time-evolved dynamic compression failure images of the D3O LITE D shear thickening foam. As seen in the images, large band like deformation features start to appear at around $5-15\%$ strain, and these grow and span the entire length of the sample at higher strains. Similar phenomenon is observed for the Liner material as well. It is noted that this kind of phenomenon is not observed for any other polymeric foam material, regardless of the strain rates and is thought to be unique to shear thickening foam materials. Therefore, a new macroscopic deformation mechanism is discovered in this shear thickening foam material which is found to be activated under dynamic loading conditions.

To investigate the cause of band formation in the D3O foam materials, further chemical characterization was performed using Energy-dispersive X-ray spectroscopy. Shown on the Left in Figure 6.8 are the set of images corresponding to the D3O LITE D material, and the Right ones correspond to the D3O Liner material. For the D3O LITE D foam,

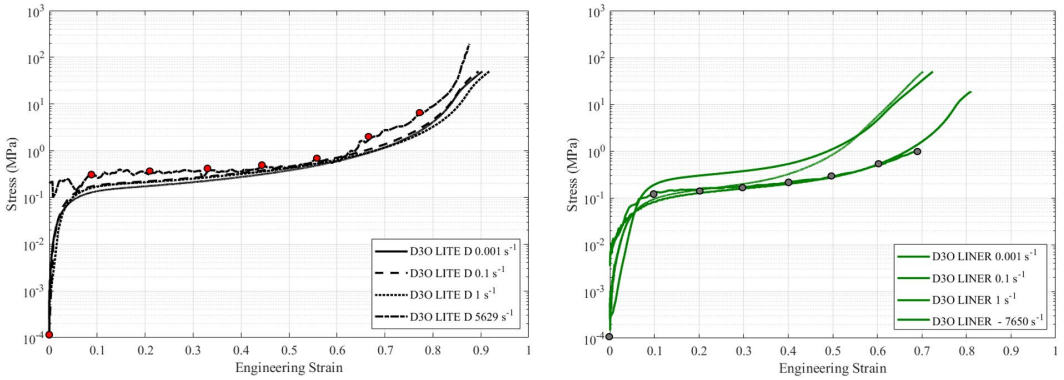

FIGURE 6.6: (Left) Stress-strain curves of D3O LITE D under uniaxial compression from strain-rates ranging from 0.001 to $\sim 5600s^{-1}$. Red points on the dynamic curve are represented by ultra-high-speed camera images shown later in Figure 6.7 (Left). (Right) Stress-strain curves of D3O Liner under uniaxial compression from strain-rates ranging from 0.001 to $\sim 7600s^{-1}$. Grey points on the dynamic curve are represented by ultra-high-speed camera images shown later in Figure 6.7 (Right).

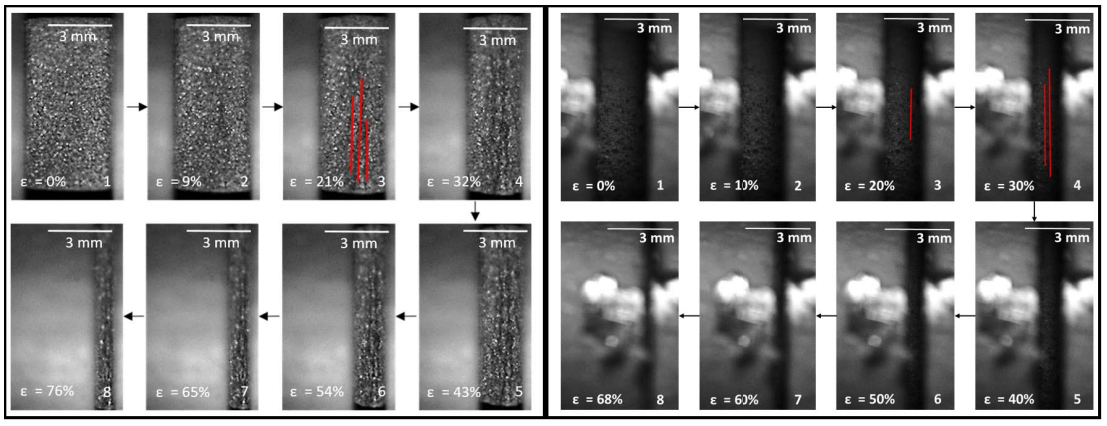

FIGURE 6.7: (Left) Time-evolved dynamic compression failure of the D3O LITE D at $5465s^{-1}$ using a split-Hopkinson Pressure Bar apparatus. Inter-frame strains are denoted at the bottom-Left corner of each image and specimen length scales are included in the top-Right corner. The red lines in image 3 emphasize larger-scale vertical localization bands that start to form in this material at approximately $\sim 10\%$ strain. (Right) Time-evolved dynamic compression failure of the D3O Liner at $7650s^{-1}$ using a split-Hopkinson Pressure Bar apparatus. Inter-frame strains are denoted at the bottom-Left corner of each image and specimen length scales are denoted on the top-Right corner of each image. The red lines in image 3 emphasize larger-scale vertical localization bands that start to form in this material at approximately $\sim 15\%$ strain.

image (a) depicts an SEM image showing pores and additive particle like structures. Images (b) and (c) show that carbon and oxygen appear together forming the base material of the foam. Image (d) shows calcium appearing at the particle-like features in the SEM image. Image (e) shows magnesium sometimes appearing together with calcium, and being spread across the material sparsely. Images (f) and (g) shows sodium and chlorine being sparsely distributed throughout the microstructure, rarely occurring together in small concentrated regions. Image (h) shows micron-sized particles of iron

occurring randomly within the microstructure. Image (i) shows a layered image which allows for distinguishing between elements and areas of occurrences. Trace elements of zinc were also found to be scattered.

For the D3O Liner material, image (a) depicts the SEM image showing pores and additive particle like structures. Images (b) and (c) show that carbon and oxygen appear together forming the base material of the foam. Image (d) shows silicon dispersed through the microstructure with small concentrated regions appearing randomly. Image (e) show potassium being dispersed with small concentrated regions of occurrence. Images (f), (g) and (h) show titanium, manganese and iron dispersed throughout the microstructure. Image (i) shows a layered image which allows for distinguishing between elements and areas of occurrences.

Overall, the formation of localizations (bands) during dynamic testing may be correlated with the presence of brittle additive particles - made of Calcium, Magnesium and Titanium. These particles are distributed at the pore edges in the microstructure. During dynamic loading, these particles are subjected to the high stresses which are transferred through the base material of the porous structure. Momentarily, these stresses exceed the fracture toughness of the additives causing catastrophic failure leading to sudden pore collapse. The pores then collapse in succession and lead to formation of macroscopic banding in the samples. These localizations are formed only as a consequence of the brittle particles and such features are not observed for foam materials without them. During quasistatic loading, the additive particles act as reinforcing agents to the microstructure, and are believed to contribute to their higher hardening rates during densification (Figure 6.6).

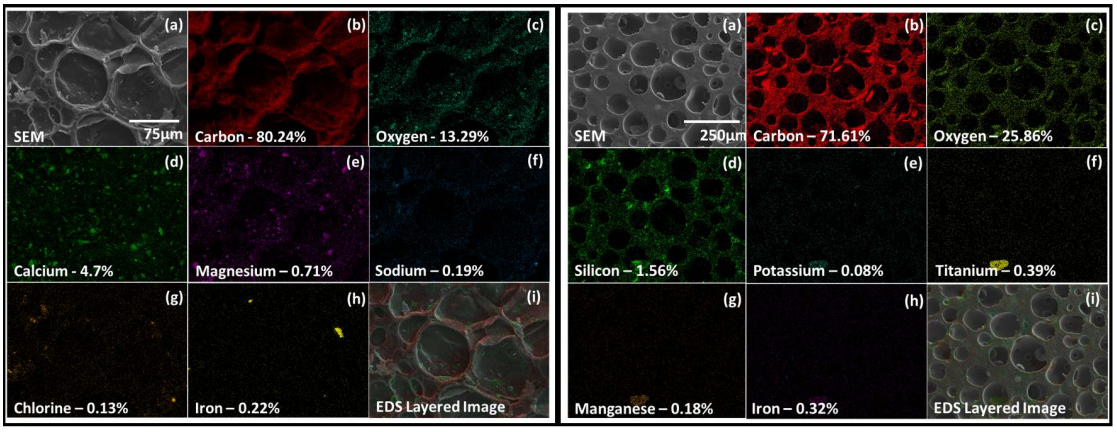

FIGURE 6.8: (Left) Composite image showing EDS elemental maps of D3O LITE D foam. (Right) Composite image showing EDS elemental maps of D3O Liner foam. Higher color intensity correspond to higher material concentration, and weight percentage distributions are noted in the images.

6.4 Scalar Mechanical Properties

In this section, the elastic modulus and plastic collapse as a function of strain rate for all foams studied in this thesis are compared, along with data from existing literature, and trends are visualized in the following figures. Figure 6.9 shows the trends of elastic modulus of PORON and D3O foams as a function of strainrate along with data in the published literature. From Figure 6.9, for open-cell foams in the literature [113], and the PORON foams studied in this thesis, it is observed that elastic modulus increases with foam density and scales according to a power-law w.r.t. strain rate. For the closed-cell foams in the literature [10, 49, 133], the elastic modulus is observed to increase with increasing foam density and strain rate. For the D3O Lite D foam, it is observed that the elastic modulus generally increases with increasing strain rate, and no obvious trends are observed for the D3O Liner material.

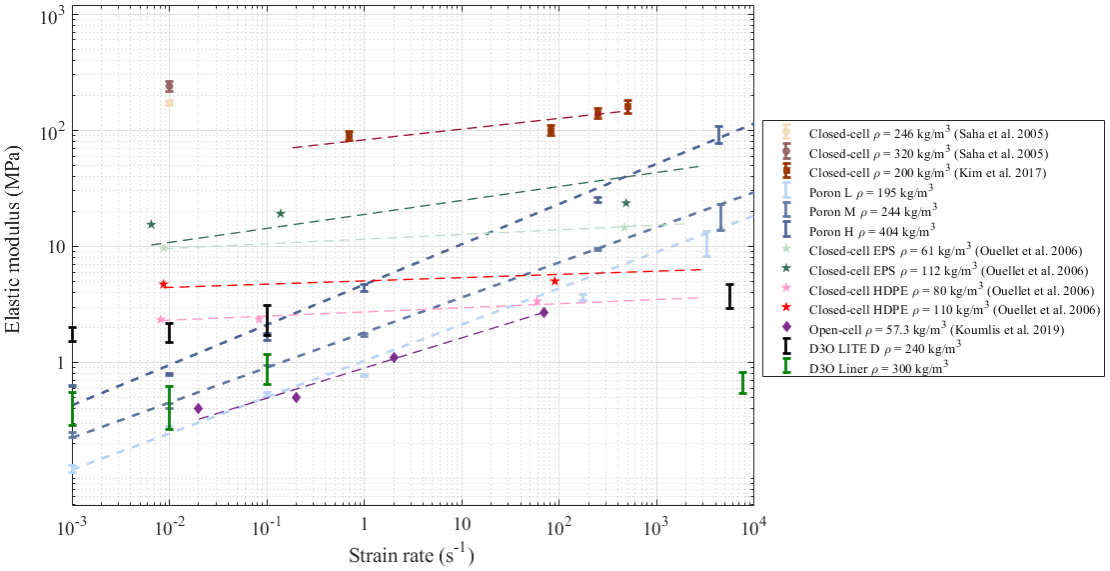

FIGURE 6.9: Trends of elastic modulus of different density foams with varying strain rates under compression loading. The y axis denotes the elastic modulus (MPa), and the x axis represents strain rate (s^{-1}), and both the axes are represented in a logarithmic scale.

Next, shown in Figure 6.10 is the comparison of collapse stress of polymeric foams of different densities [10, 49, 113] with varying strain rate. From the figure, the collapse stress is observed to increase with increasing foam density and strain rate, with higher strain rate dependency for open-cell foams when compared to closed-cell foams. For the D3O Lite D foam, it is observed that the collapse stress generally increases with increasing strain rate, and no obvious trends are observed for the D3O Liner material. In this thesis, it is found that for open-celled foam materials, a power-law fit best describes the relationships between elastic modulus and, collapse stress, and strain rate.

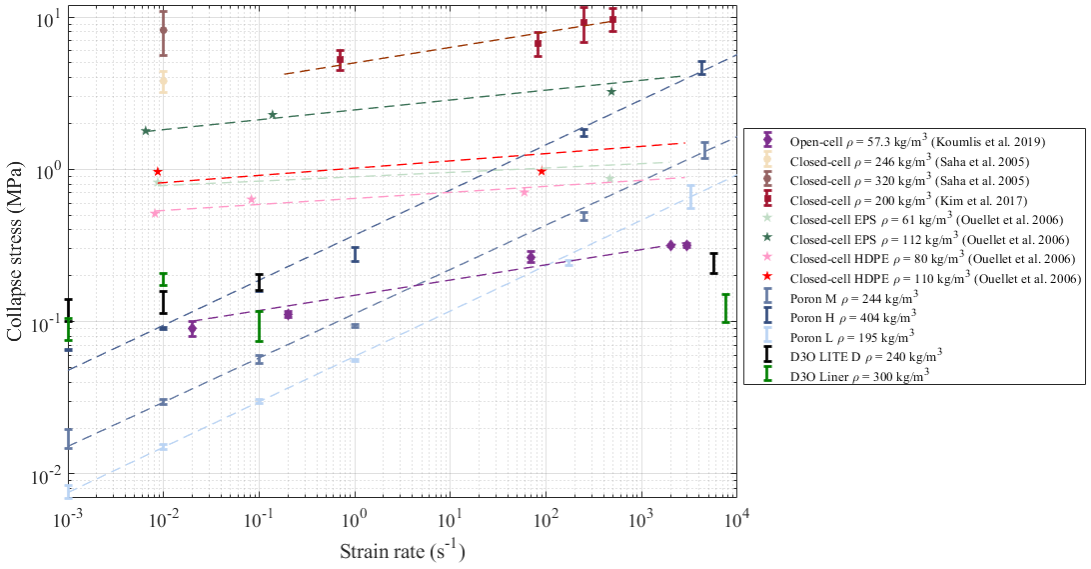

FIGURE 6.10: Figure showing trends of collapse strength of different density foams with varying strain rates under compression loading. The y axis denotes the collapse stress (MPa) and the x axis represents strain rate (s^{-1}), and both the axes are represented in a logarithmic scale.

6.5 Discussion

6.5.1 Comparison of Mechanical Behavior

Generally, all stress-strain curves for both PORON and D3O foams show three deformation regimes, namely, *elastic behavior* up to a yield or *collapse* stress (σ_{pl}), a *plateau* regime where the stress is near constant, and a *densification* regime where stress increases rapidly with increasing strain [7, 10, 113, 128], with some minor differences. The D3O - shear thickening foams notably show two distinct modes of densification under dynamic uniaxial compression which are linked to formation of unique deformation features called localizations. Comparing the magnitudes of elastic modulus and collapse stress between PORON and D3O foams, it is observed that PORON foams are highly sensitive to strain rate and increase according to a power-law. For the D3O foams, it is observed that mechanical properties are not sensitive to strain rate.

6.5.2 Prospect as Helmet Liner

The performance of the foam helmet liner is dependent on its mechanical properties, such as the strength and its energy absorbing capabilities [162]. Typical foam materials used as helmet liners include Expanded Polystyrene (EPS) [17, 22, 46], Expanded Polypropylene (EPP) [7, 22], and Thermoplastic Polyurethanes (TPU) [43, 47]. To characterize the liner

materials response, some groups have looked at energy absorption diagrams [18] while other studies have focused on better understanding the effect of microstructure [7, 10, 47], density [7, 10, 22] and strain-rate [7, 10, 46, 48, 49] in tension [50] and compression [17, 41, 49–54], as well as during impact experiments using gas-gun approaches [41].

In one study, Di Landro et al. [17] has looked at the effects of density and found that higher density foams are able to absorb more energy, which reduces the amount going through the brain, but transmit higher accelerations, leading to higher likelihood of traumatic brain injury (TBI). Additionally both Di Landro et al. [17] and Santa Maria et al. [52] suggest smaller cell sizes improve the strength of a material. Other experimental studies [7, 10] have compared different microstructures, finding that the smaller cell size generally had higher peak stresses, and absorbed more energy compared to larger cell sizes at higher strain rates.

Overall, from experimental observations in Table 6.1, Figures 6.9 and 6.10, and observations from the literature, it is noted that although there are other foam candidates including PORON foams that can potentially absorb more stress at higher rates, the D3O foams strike a good balance between the pore morphology and the energy absorbing capabilities for the application of helmet liner materials. It is also observed that not all foam materials follow ordered trends and can be described by the same models and these differences generally occur as a consequence of differences in microstructures and base materials.

Chapter 7

Concluding Remarks

7.1 Conclusion

The focus of this thesis has been to understand the effects of density, microstructure, and strain rate on the mechanical response of polymeric foam materials utilizing experimental mechanics approaches. This is achieved by studying various aspects of foams such as: 1. as-received microstructures; 2. rate-dependent mechanical properties under uniaxial compression and tension; 3. rate-dependent deformation and failure mechanisms; and 4. microstructure-dependent deformation and failure mechanisms. To assess the above information, advanced microscopy techniques, including high-resolution scanning electron microscopy, high-resolution X-ray tomography, energy-dispersive X-ray spectroscopy, and Fourier transform infrared spectroscopy were used to investigate the microstructural features and chemical compositions of the pristine materials. Mechanical testing, including quasi-static, intermediate and dynamic uniaxial compression tests, were carried out on a standard electro-dynamic Instron machine, advanced drop tower, and split-Hopkinson pressure bar apparatus, respectively; quasi-static tensile experiments were also performed. State-of-the-art ultra-high-speed imaging coupled with digital image correlation technique was used to visualize surface deformation, relate microscopic failure mechanisms influence on macroscopic behavior using lateral-axial strain information, and to establish stress-strain relationships.

This thesis achieves its objective of providing a better understanding of the effects of density, microstructure, and strain rate on the mechanical response of polymeric foam materials in the form of four peer-reviewed papers (Chapters 2, 3, 4 and 5). The key results from the works are summarized below for further emphasis:

1. Microstructure observations - Microstructural investigation of the materials reveal that the different PU foams from Poron have similar pore morphology with near-spherical shape but have different pore sizes and wall thicknesses. The shear thickening foam materials from D3O are observed to have different pore morphology and topologies compared to the Poron foams. The D3O LITE D foam is found to have irregularly shaped pores while the D3O Liner foam is found to have a spherical pore structure with varying wall thicknesses. Key microstructural parameters, like pores sizes and wall thicknesses, have been identified using image processing techniques on SEM and XCT images. The range of pore sizes in x and y directions for the different materials in this thesis are tabulated as: $5-114\ \mu m$ and $6-142\ \mu m$ for for Poron LD foam; $6-100\ \mu m$ and $8-110\ \mu m$ for the Poron MD foam; $5-75\ \mu m$ for both directions for Poron HD foam; $12-50\ \mu m$ for both x and y directions for D3O LITE D foam; and $13-62\ \mu m$ for the D3O Liner foam material. The range of wall thicknesses in both x and y direction for the different materials are identified as $2-19\ \mu m$ for the D3O LITE D material; $2-40\ \mu m$ for the D3O LITE D material; and $2\mu m$ and $23\mu m$ in both x and y directions for the PORON foams. Evolution of microstructure was studied for both compression and tension for the D3O LITE D foam. For the compressive stress state, no clear trends in pore size evolution were observed and permanent damage was found to occur only after complete pore collapse at strains $> 0.8 \pm 0.03$. For the tensile stress state, pore sizes were found to increase linearly with increasing strain, and it was observed that bigger pores ($D > 100\mu m$) are more susceptible to greater changes in size when strained when compared to smaller pores. The changes in wall thicknesses were comparatively negligible through the entire strain range (0 to 3.05 ± 0.05 in tension and $> 0.8 \pm 0.3$ in compression). Further observations from SEM and XCT of the shear thickening foam materials reveal the presence of additive particles dispersed in the microstructure (found at pore edges). EDS investigation on the STF reveal the presence of additive particles made of Calcium, Magnesium, Potassium, Titanium and trace elements of Sodium, Chlorine, Manganese and Iron. FTIR spectroscopy is used to inform about the chemical constituents and configuration of the macromolecules present in the polymeric foam materials finding that the D3O LITE D foam is made up of a polyethylene-based monomer, the D3O Liner material is made of a polydimethylsiloxane (PDMS) structure, and the Poron material is made up of a polyurethane structure.

2. Shear thickening behavior - The stress-strain behavior of the D3O LITE D and D3O Liner foams exhibits multiple strain hardening regimes in the densification regime, under uniaxial compression loading as compared to the typical behavioral regimes exhibited by the PORON foams. This behavior is found to be rate sensitive and hardening rate increases with increasing strain rate. In this thesis, it is found that

this type of behavior only appears for the shear thickening foam materials. This indicates a different failure process in the shear thickening foams at the different loading rates. The shear thickening foams from D3O exhibits macroscopic surface deformation in the form of localizations (bands) during dynamic testing, and this is correlated with the presence of brittle reinforcing additive particles - made of Calcium, Magnesium and Titanium. These particles are distributed at the pore edges in the microstructure. During dynamic loading, these particles are subjected to the high stresses which momentarily exceed the fracture toughness of the additives causing catastrophic failure leading to sudden pore collapse. The pores collapse in succession and lead to formation of macroscopic banding in the samples. Such features are not observed for foam materials without them. During quasistatic loading, the additive particles are believed to act as reinforcing agents to the microstructure, and contribute to higher hardening rates during densification.

3. Density and strain rate effects - Phenomenological relationships are developed to link density and microstructure properties, and for prediction of mechanical strength parameters such as elastic modulus E, and collapse stress (σ_{pl}). The variation of the foam's characteristic properties (i.e., elastic modulus, collapse stress, with respect to strain rate are expressed in terms of the characteristic property value at the reference strain rate. These properties are found to scale according to a power-law fashion with respect to strain rate. The rate dependent compressive response was fit to the Avalle model [20] and model coefficients were found to be density dependent and vary following a power-law.

4. Deformation evolution - In-situ deformation evolution in polymeric foam materials is studied for a wide range of strain rates under uniaxial compression. In this thesis, the utilization of DIC enables in-situ measurements of tangent modulus and Poisson's ratio. From the measurements, it is shown that Poisson's ratio evolves in a non-monotonic and non-linear manner during compressive loading. These captured trends are used to identify transitional behaviours in these materials. Overall, this thesis addresses some of the limitations that are noted in the literature such as lack of consideration for the effect of strain rate, and the effect of Poisson's ratio during loading. In this thesis, this gap is addressed by investigating mechanical properties and failure behavior for a wide range of strain rates alongside comparing with microstructure properties. These kind of in-situ measurements are shown for the first time and these measurements are motivated by looking at the evolution of these properties to learn about transitional behaviours.

7.2 Implications

In this thesis, a better understanding of the effects of density, microstructure and strain rate on the mechanical response of polymeric foam materials is provided, with detailed characterization and mechanical testing at different strain rates. All foams under consideration exhibited rate-dependency on mechanical properties and failure mechanisms under uniaxial compression at different loading rates. Exploring the material behaviors at different loading rates is nevertheless critical in assessing material performance in the energy absorbing structural applications [17, 22, 46]. The experimental and characterization data generated in this thesis will benefit shear thickening foam literature, as well as that of polymeric foam literature in general. Altogether, this work makes the following contributions:

1. Developing a comprehensive framework for studying failure and deformation of polymeric foam materials by incorporating DIC, high-speed-imaging, IR imaging, and advanced characterization techniques (e.g., XCT and Matlab). This work can be extended to the study of other soft porous materials, such as tissue and other bio-materials.

2. Characterizing the microstructure of the as-received shear thickening and PU foam materials, which serves as important inputs in constructing a unit cell material model that could be implemented into large-scale computational simulations [36–39].

3. The "shear thickening" behaviour in the STF materials is explained as a manifestation of multiple hardening regimes during densification under uniaxial compressive loading. This behaviour is caused as a consequence of the presence of small brittle additive particles dispersed throughout the edges of the foam microstructure. Rate-dependency on mechanical properties and failure mechanisms are comprehensively investigated, for which the data sets are valuable for both evaluating material performance in protection applications [43–45] and in implementing material features in micromechanical modeling [8, 37, 38].

4. Providing a comprehensive set of rate-dependent stress-strain curves, elastic modulus, collapse stresses and 2D failure strain data for a wide range of polymeric foams, which can be used as a reference for future studies of similar materials. This data is also valuable in material model validation [8, 36–39].

5. Delivering an inclusive comparison of the mechanical properties and failure mechanisms of the shear thickening foams and PU foams to other similar foam systems.

This data set may provide insights to the industries when the material is considered to be used in some of their applications (e.g., personnel protection [43–45], automotive [41], and packaging [7]).

6. Developing methods to study in-situ deformation evolution, and providing some of the first data on in-situ measurements of Poissons's ratio and Tangent modulus in polymeric foam materials. This data provides valuable insights into deformation mechanisms and transitional behaviours, and also serves as an input for accurate prediction of failure [3, 163], and for model validation [46, 110].

7. Developing an analytical framework to predict foam mechanical response that takes into account microstructure, density, failure, and rate-effects. This includes development of scaling laws to predict mechanical strength parameters such as elastic modulus and collapse strength.

7.3 Future Works and Recommendations

To the best of our knowledge, this work is some of the first reports on the experimental mechanics of shear thickening foam materials at the date of submission. The lack of experimental works might be because of the novelty of the material, the difficulties in studying porous polymeric foam materials experimentally, and the only recent developments in coupling high-speed imaging and DIC techniques. The data generated in this thesis informs material modeling and model validation. To build upon the current work, the following future directions and recommendations are suggested:

1. Tailor material microstructure via manufacturing through addition of additive particles, varying densities, using different base polymers. This will change the mechanical properties and failure mechanisms of polymeric foam materials.

2. Design experimental setup at synchrotron facilities for in-situ deformation where quantitative microstructural parameter analysis can be performed with the developed MATLAB techniques developed in this thesis. Studying the deformation behavior of foam materials is proven to be crucial in structural applications[39, 131, 132].

3. Conduct laboratory-scale temperature-dependant and confined compression experiments to assess material damage and behavior for different stress states, and study the effects of temperature and pressure on rate sensitivity of polymeric foams.

4. Modify the Kolsky bar system to access intermediate strain rates and to achieve additional stress-states, such as impact and confined dynamic compression, in order to study material behavior can be explored.

5. Develop new laboratory-scale (e.g., plate-impact [118, 164], dynamic tension [165, 166]) and full scale experiments (e.g., ballistic impact [87, 167], shock [6, 139]) experiments, for which data will be valuable in modeling (e.g., material damage and deformation [163], tensile behavior [11, 12]) and validation (e.g., damage pattern visualization [3, 163], collapse stress prediction [46, 110]).

6. Collaborate with facilities, such as nanoFAB and Canadian Light Source synchrotron, to perform in-situ testing (e.g., in-situ high/low-temperature SEM, and in-situ computed tomography with compression and tension at different loading rates, etc.) and obtain information on instantaneous response (e.g., damage accumulation, microstructure changes) of material.

7. Explore suitable analytical and phenomenological models that could be used in large-scale simulations (e.g., the Rusch model [132] for compression and fatigue) for polymeric foam materials, and obtain and validate a set of model parameters through the design of experiments (e.g., indentation [168], shear [12]).

8. In addition, one can modify the existing analytical [40, 131, 137] and phenomenological models [74, 130, 144, 147, 148] by adding terms (i.e., Poisson's ratio evolution; stiffness evolution) or changing the term representation functions base on experimental results.

7.4 Academic Contributions

Journal Publications:

The thesis and other experimental developments have resulted in the following journal publications:

1. **Kapil Bharadwaj B**; Azar, A; Dennison, CR; Satapathy, S; Ouellet, S and Hogan, JD. *High Rate Compressive Behaviour of a Dilatant Polymeric Foam*, Journal of dynamic behavior of materials. (2018)

2. **Kapil Bharadwaj B**; Parcon, JS; Azar, A; Dennison, CR; Satapathy, S; Ouellet, S and Hogan, JD. *Quasistatic response of a shear-thickening foam: Microstructure evolution and infrared thermography*, Journal of dynamic behavior of materials. (2020)

3. **Kapil Bharadwaj B**; Meredith, C; Satapathy, S; Ouellet, S; Romanyk, D; and Hogan, JD. *Density, microstructure and strain-rate effects on response of polyurethane foams.* (Accepted to be published in Experimental Mechanics - 2021)

4. **Kapil Bharadwaj B**; Meredith, C; Satapathy, S; Ouellet, S; Romanyk, D; and Hogan, JD. *Phenomenological modelling of rate dependant compressive response of polyurethane foams.* (Submitted to International Journal of Impact Engineering - 2021)

5. Shao C., Lo C., **Kapil Bharadwaj B** et al., *High Strength Particulate Aluminum Matrix Composite Design: Synergistic Strengthening Strategy*, Composites Communications (2021)

6. Adanty, K., Rabey, K.N., **Kapil Bharadwaj B** et al., *Cortical and trabecular morphometric properties of the human calvarium*, BONE (2020)

7. Azar, A., **Kapil Bharadwaj B** et al., *Protective Headgear Attenuates Forces on the Inner Table and Pressure in the Brain Parenchyma During Blast and Impact: An Experimental Study Using a Simulant-Based Surrogate Model of the Human Head*, . ASME. J Biomech Eng (2020)

8. Azar, A., **Kapil Bharadwaj B** et al., *An Optical Fiber Transducer for Measuring Kinetics of Skull-Brain Interaction in a Surrogate Model of the Human Head Subjected to Blast Overpressure*, IEEE Sensors Journal (2019)

Conferences:

The thesis and other experimental developments have also resulted in several conference presentations:

1. **Kapil Bharadwaj B**; Meredith, C; Satapathy, S; Ouellet, S; Romanyk, D; and Hogan, JD (2021) *Strain Rate Dependant Compressive Response and Damage Evolution in Polymeric Foams*, SEM 2021: Conference and Exposition on Experimental and Applied Mechanics, June 14-17, 2021, Virtual conference. **Conference presentation**

2. **Kapil Bharadwaj B**; Ouellet, S., Plaisted, T.A., Satapathy, S.S., Romanyk, D, and Hogan, JD (2021) *Characterization and Meso-Macrostructure Dependant Compressive and Failure Response of Human Cranial Bone And Surrogate*, SEM 2021: Conference and Exposition on Experimental and Applied Mechanics, June 14-17, 2021, Virtual conference. **Conference presentation**

3. **Kapil Bharadwaj B**; Dennison, CR; Satapathy, S; Ouellet, S and Hogan, JD (2020) *Effect of density, microstructure and strain rate on response of polymeric foams*, SEM 2020: Conference and Exposition on Experimental and Applied Mechanics, September 14-17, 2020, Virtual conference. **Conference presentation**

4. **Kapil Bharadwaj B**; Dennison, CR; Satapathy, S; Ouellet, S and Hogan, JD (2020) *Characterization and constitutive modeling of shear-thickening polymeric foams*, SEM 2020: Conference and Exposition on Experimental and Applied Mechanics, September 14-17, 2020, Virtual conference. **Conference presentation**

5. **Kapil Bharadwaj B**; Parcon, JS; Azar, A; Dennison, CR; Satapathy, S; Ouellet, S and Hogan, JD (2019) *Effect of Density, Microstructure and Temperature on response of polymeric foams*, SEM 2019: Conference and Exposition on Experimental and Applied Mechanics, June 4-6, 2019 Reno NV (USA). **Conference presentation**

6. **Kapil Bharadwaj B**; Parcon, JS; Dennison, CR; Satapathy, S; Ouellet, S and Hogan, JD (2018) *Microstructure characterization and compressive response of two dilatant polymeric foams*, 30th Canadian material Science Conference, June 19-22, 2018 Edmonton AB (Canada). **Poster presentation**

7. **Kapil Bharadwaj B**; Azar, A; Dennison, CR; Satapathy, S; Ouellet, S and Hogan, JD (2018) *Microstructure characterization and Thermo-Mechanical response of a dilatant polymeric foam*, The Hopkins Extreme Materials Institute 2018 MACH Conference, April 4-6, Annapolis MD (USA). **Poster presentation**

8. **Kapil Bharadwaj B**; Bell, KA; Motamedi, P; Dennison, CR; and Hogan, JD (2017) *Failure of Polymeric Foams under Quasi-Static and Dynamic Loads*, The Hopkins Extreme Materials Institute 2017 MACH Conference, April 5-7, Annapolis MD (USA). **Poster presentation**

Bibliography

[1] Ghatu Subhash, Qunli Liu, and Xin-Lin Gao. Quasistatic and high strain rate uniaxial compressive response of polymeric structural foams. *International Journal of Impact Engineering*, 32(7):1113–1126, 2006.

[2] W. Chen, F. Lu, and N. Winfree. High-strain-rate compressive behavior of a rigid polyurethane foam with various densities. *Experimental Mechanics*, 42(1):65–73, 2002. ISSN 00144851. doi: 10.1177/0018512002042001791.

[3] Brian M. Patterson, Nikolaus L. Cordes, Kevin Henderson, Jason J. Williams, Tyler Stannard, Sudhanshu S. Singh, Angel Rodriguez Ovejero, Xianghui Xiao, Mathew Robinson, and Nikhilesh Chawla. In situ X-ray synchrotron tomographic imaging during the compression of hyper-elastic polymeric materials. *Journal of Materials Science*, 51(1):171–187, 2015. ISSN 15734803. doi: 10.1007/s10853-015-9355-8.

[4] Arun Shukla, Yapa D.S. Rajapakse, and Mary Ellen Hynes. *Blast mitigation: Experimental and numerical studies*, volume 9781461472. Springer New York, New York, NY, 2013. ISBN 9781461472674. doi: 10.1007/978-1-4614-7267-4. URL `http://link.springer.com/10.1007/978-1-4614-7267-4`.

[5] M. F. Ashby. The properties of foams and lattices. *Philosophical Transactions of the Royal Society A: Mathematical, Physical and Engineering Sciences*, 364(1838): 15–30, 2006. ISSN 1364503X. doi: 10.1098/rsta.2005.1678.

[6] D.M. Dattelbaum, D.L. Robbins, R.L. Gustavsen, S.A. Sheffield, D.B. Stahl, and J.D. Coe. Shock compression of polyurethane foams. *EPJ Web of Conferences*, 26:02014, 2012. ISSN 2100-014X. doi: 10.1051/epjconf/20122602014. URL `http://dx.doi.org/10.1051/epjconf/20122602014`.

[7] Rémy Bouix, Philippe Viot, and Jean Luc Lataillade. Polypropylene foam behaviour under dynamic loadings: Strain rate, density and microstructure effects. *International Journal of Impact Engineering*, 36(2):329–342, feb 2009. ISSN 0734743X. doi: 10.1016/j.ijimpeng.2007.11.007. URL `http://linkinghub.elsevier.com/retrieve/pii/S0734743X08000791`.

[8] Stavros Gaitanaros and Stelios Kyriakides. On the effect of relative density on the crushing and energy absorption of open-cell foams under impact. *International Journal of Impact Engineering*, 82:3–13, 2015. ISSN 0734743X. doi: 10.1016/j.ijimpeng.2015.03.011. URL http://dx.doi.org/10.1016/j.ijimpeng.2015.03.011.

[9] N. J. Mills, R. Stämpfli, F. Marone, and P. A. Brühwiler. Finite element micromechanics model of impact compression of closed-cell polymer foams. *International Journal of Solids and Structures*, 46(3-4):677–697, 2009. ISSN 00207683. doi: 10.1016/j.ijsolstr.2008.09.012. URL http://dx.doi.org/10.1016/j.ijsolstr.2008.09.012.

[10] M. C. Saha, H. Mahfuz, U. K. Chakravarty, M. Uddin, Md E. Kabir, and S. Jeelani. Effect of density, microstructure, and strain rate on compression behavior of polymeric foams. *Materials Science and Engineering A*, 406(1-2):328–336, oct 2005. ISSN 09215093. doi: 10.1016/j.msea.2005.07.006. URL http://linkinghub.elsevier.com/retrieve/pii/S0921509305006830.

[11] Timothy R. Walter, Andrew W. Richards, and Ghatu Subhash. A Unified Phenomenological Model for Tensile and Compressive Response of Polymeric Foams. *Journal of Engineering Materials and Technology*, 131(1):011009, 2009. ISSN 00944289. doi: 10.1115/1.3026556. URL http://materialstechnology.asmedigitalcollection.asme.org/article.aspx?articleid=1428331.

[12] Dan Zenkert and Magnus Burman. Tension, compression and shear fatigue of a closed cell polymer foam. *Composites Science and Technology*, 69(6):785–792, 2009. ISSN 02663538. doi: 10.1016/j.compscitech.2008.04.017.

[13] Amin Ajdari, Hamid Nayeb-Hashemi, and Ashkan Vaziri. Dynamic crushing and energy absorption of regular, irregular and functionally graded cellular structures. *International Journal of Solids and Structures*, 48(3-4):506–516, 2011. ISSN 00207683. doi: 10.1016/j.ijsolstr.2010.10.018. URL http://dx.doi.org/10.1016/j.ijsolstr.2010.10.018.

[14] J. Lankford and K. A. Dannemann. Strain Rate Effects in Porous Materials. *MRS Proceedings*, 521:103–108, 1998. doi: 10.1557/proc-521-103.

[15] S Deschanel, L Vanel, G Godin, E Maire, G Vigier, S Ciliberto, S Deschanel, L Vanel, G Godin, E Maire, and G Vigier. Mechanical response and fracture dynamics of polymeric foams. *Journal of Physics D: Applied Physics*, 2009. doi: 10.1088/0022-3727/42/21/214001.

[16] Md E. Kabir, M. C. Saha, and S. Jeelani. Tensile and fracture behavior of polymer foams. *Materials Science and Engineering A*, 429(1-2):225–235, 2006. ISSN 09215093. doi: 10.1016/j.msea.2006.05.133.

[17] Luca Di Landro, Giuseppe Sala, and Daniela Olivieri. Deformation mechanisms and energy absorption of polystyrene foams for protective helmets. *Polymer Testing*, 21(2):217–228, 2002. ISSN 01429418. doi: 10.1016/S0142-9418(01)00073-3.

[18] M. Avalle, G. Belingardi, and R. Montanini. Characterization of polymeric structural foams under compressive impact loading by means of energy-absorption diagram. *International Journal of Impact Engineering*, 25(5):455–472, 2001. ISSN 0734743X. doi: 10.1016/S0734-743X(00)00060-9.

[19] Youming Chen, Raj Das, and Mark Battley. Effects of cell size and cell wall thickness variations on the stiffness of closed-cell foams. *International Journal of Solids and Structures*, 52(Supplement C):150–164, 2015. ISSN 00207683. doi: 10.1016/j.ijsolstr.2014.09.022.

[20] Massimiliano Avalle, Giovanni Belingardi, and Andrea Ibba. Mechanical models of cellular solids: Parameters identification from experimental tests. *International Journal of Impact Engineering*, 34(1):3–27, jan 2007. ISSN 0734743X. doi: 10.1016/j.ijimpeng.2006.06.012. URL `http://linkinghub.elsevier.com/retrieve/pii/S0734743X06001023`.

[21] Catherine M. Ford and Lorna J. Gibson. Uniaxial strength asymmetry in cellular materials: An analytical model. *International Journal of Mechanical Sciences*, 40 (6):521–531, 1998. ISSN 00207403. doi: 10.1016/S0020-7403(97)00064-7.

[22] D. S. Cronin and S. Ouellet. Low density polyethylene, expanded polystyrene and expanded polypropylene: Strain rate and size effects on mechanical properties. *Polymer Testing*, 53:40–50, aug 2016. ISSN 01429418. doi: 10.1016/j.polymertesting.2016.04.018.

[23] L. J. Gibson and M. F. Ashby. The Mechanics of Three-Dimensional Cellular Materials. *Proceedings of the Royal Society A: Mathematical, Physical and Engineering Sciences*, 382(1782):43–59, jul 1982. ISSN 1364-5021. doi: 10.1098/rspa.1982.0088. URL `http://rspa.royalsocietypublishing.org/cgi/doi/10.1098/rspa.1982.0088`.

[24] John Fitek and Erin Meyer. Design of a helmet liner for improved low velocity impact protection.

[25] Kapil Bharadwaj Bhagavathula, Austin Azar, Simon Ouellet, Sikhanda Satapathy, Christopher R. Dennison, and James David Hogan. High Rate Compressive

Behaviour of a Dilatant Polymeric Foam. *Journal of Dynamic Behavior of Materials*, 4(4):573–585, dec 2018. ISSN 2199-7446. doi: 10.1007/s40870-018-0176-0. URL http://dx.doi.org/10.1007/s40870-018-0176-0http://link.springer.com/10.1007/s40870-018-0176-0.

[26] Stefano Signetti, Marco Nicotra, Martino Colonna, and Nicola M. Pugno. Modeling and simulation of the impact behavior of soft polymeric-foam-based back protectors for winter sports. *Journal of Science and Medicine in Sport*, 0(0), nov 2018. ISSN 14402440. doi: 10.1016/j.jsams.2018.10.007. URL https://linkinghub.elsevier.com/retrieve/pii/S144024401831065X.

[27] Jie Ding, Phillip J Tracey, and Philip G Whitten. Review on shear thickening fluids and applications. 2:161–173, 2013.

[28] D. V. W. M. de Vries. *Characterization of polymeric foams*. PhD thesis, Eindhoven University of Technology, 2009.

[29] V Shastri and Molly Stevens. Polymer Foams. *Encyclopedia of Biomaterials and Biomedical Engineering, Second Edition - Four Volume Set*, pages 2270–2274, 2008. doi: 10.1201/b18990-217.

[30] Kun Sup Hyun and Myung-ho Kim. Foam Extrusion with Physical Blowing Agents—Practical Approach.

[31] Jeppe C Dyre. Colloquium: The glass transition and elastic models of glass-forming liquids. *Reviews of modern physics*, 78(3):953, 2006.

[32] Fan-Long Jin, Miao Zhao, Mira Park, and Soo-Jin Park. Recent trends of foaming in polymer processing: A review. *Polymers*, 11(6):953, 2019.

[33] Mihail. Ionescu. *Chemistry and Technology of Polyols for Polyurethane Volume 2*, volume 2. 2016. ISBN 978-1-84735-035-0.

[34] Energy absorbing material, . URL https://patents.google.com/patent/WO2003055339A2/en?oq=GB+0130834%2c+2001.

[35] PI Dolez and J Mlynarek. Smart materials for personal protective equipment: Tendencies and recent developments. In *Smart textiles and their applications*, pages 497–517. Elsevier, 2016.

[36] A. D. Brydon, S. G. Bardenhagen, E. A. Miller, and G. T. Seidler. Simulation of the densification of real open-celled foam microstructures. *Journal of the Mechanics and Physics of Solids*, 53(12):2638–2660, 2005. ISSN 00225096. doi: 10.1016/j.jmps.2005.07.007.

[37] Zhengwei Nie, Yuyi Lin, and Qingbin Tong. Modeling structures of open cell foams. *Computational Materials Science*, 131:160–169, 2017. ISSN 09270256. doi: 10.1016/j.commatsci.2017.01.029. URL `http://dx.doi.org/10.1016/j.commatsci.2017.01.029`.

[38] Wen Yea Jang, Andrew M. Kraynik, and Stelios Kyriakides. On the microstructure of open-cell foams and its effect on elastic properties. *International Journal of Solids and Structures*, 45(7-8):1845–1875, 2008. ISSN 00207683. doi: 10.1016/j.ijsolstr.2007.10.008.

[39] Jithender J. Timothy and Günther Meschke. A cascade continuum micromechanics model for the effective elastic properties of porous materials. *International Journal of Solids and Structures*, 83:1–12, apr 2016. ISSN 00207683. doi: 10.1016/j.ijsolstr.2015.12.010. URL `https://linkinghub.elsevier.com/retrieve/pii/S0020768315005028`.

[40] NJ Mills. Polyurethane foams: processing and microstructure. pages 19–37, 2007. doi: 10.1016/B978-075068069-1/50003-9. URL `https://linkinghub.elsevier.com/retrieve/pii/B9780750680691500039`.

[41] S Ouellet, DS Cronin, J Moulton, and OE Petel. High rate characterization of polymeric closed-cell foams: challenges related to size effects. pages 21–28, 2013.

[42] S Nemat-Nasser, WJ Kang, JD McGee, W-G Guo, and JB Isaacs. Experimental investigation of energy-absorption characteristics of components of sandwich structures. *International journal of impact engineering*, 34(6):1119–1146, 2007.

[43] David F Sounik, Peter Gansen, John L Clemons, and John W Liddle. Head-impact testing of polyurethane energy-abosrbing (ea) foams. *SAE transactions*, pages 211–220, 1997.

[44] Ibolja Cernak, Andrew C Merkle, Vassilis E Koliatsos, Justin M Bilik, Quang T Luong, Theresa M Mahota, Leyan Xu, Nicole Slack, David Windle, and Farid A Ahmed. The pathobiology of blast injuries and blast-induced neurotrauma as identified using a new experimental model of injury in mice. *Neurobiology of disease*, 41(2):538–551, 2011.

[45] S Kiernan, L Cui, and MD Gilchrist. Novel energy absorbing materials with applications in helmeted head. In *ISBS-Conference Proceedings, 27 International Conference on Biomechanics in Sports (2009)*, pages 186–189, 2009.

[46] Bo Song, Weinong W. Chen, Songbai Dou, Nancy A. Winfree, and Joseph H. Kang. Strain-rate effects on elastic and early cell-collapse responses of a polystyrene foam.

International Journal of Impact Engineering, 31(5):509–521, 2005. ISSN 0734743X. doi: 10.1016/j.ijimpeng.2004.02.003.

[47] K. Gao, J. A.W. van Dommelen, and M. G.D. Geers. Microstructure characterization and homogenization of acoustic polyurethane foams: Measurements and simulations. *International Journal of Solids and Structures*, 100-101:536–546, dec 2016. ISSN 00207683. doi: 10.1016/j.ijsolstr.2016.09.024.

[48] ST Marais, RB Tait, TJ Cloete, and GN Nurick. Material testing at high strain rate using the split hopkinson pressure bar. *Latin American Journal of Solids and Structures*, 1(3):219–339, 2004.

[49] Simon Ouellet, Duane Cronin, and Michael Worswick. Compressive response of polymeric foams under quasi-static, medium and high strain rate conditions. *Polymer Testing*, 25(6):731–743, sep 2006. ISSN 01429418. doi: 10.1016/j.polymertesting.2006.05.005. URL `http://linkinghub.elsevier.com/retrieve/pii/S0142941806000973`.

[50] W Chen, F Lu, and M Cheng. Tension and compression tests of two polymers under quasi-static and dynamic loading. *Polymer testing*, 21(2):113–121, 2002.

[51] Lili Wang, K Labibes, Z Azari, and G Pluvinage. Generalization of split hopkinson bar technique to use viscoelastic bars. *International journal of impact engineering*, 15(5):669–686, 1994.

[52] Joseph A Santa Maria, Benjamin F Schultz, JB Ferguson, Nikhil Gupta, and Pradeep K Rohatgi. Effect of hollow sphere size and size distribution on the quasi-static and high strain rate compressive properties of al-a380–al 2 o 3 syntactic foams. *Journal of materials science*, 49(3):1267–1278, 2014.

[53] W Chen and B Zhou. Constitutive behavior of epon 828/t-403 at various strain rates. *Mechanics of time-dependent materials*, 2(2):103–111, 1998.

[54] P Viot and F Beani. Comportement de mousses polymeres en compression dynamique. *Revue des Composites et des Matériaux Avancés*, 13(3):283–92, 2003.

[55] George T GRAY III. Classic split hopkinson pressure bar testing. *ASM handbook*, 8:462–476, 2000.

[56] GT Gray III and William R Blumenthal. Split-hopkinson pressure bar testing of soft materials. *ASM handbook*, 8:488–496, 2000.

[57] R. Clamroth. Determination of viscoelastic properties by dynamic testing. *Polymer Testing*, 2(4):263–286, oct 1981. ISSN 01429418. doi: 10.1016/

0142-9418(81)90012-X. URL https://linkinghub.elsevier.com/retrieve/pii/014294188190012X.

[58] JA Harris. Dynamic testing under nonsinusoidal conditions and the consequences of nonlinearity for service performance. *Rubber chemistry and technology*, 60(5): 870–887, 1987.

[59] Marc A Meyers. *Dynamic behavior of materials*. John wiley & sons, 1994.

[60] D3o formable foams, . URL https://www.d3o.com/wp-content/uploads/2016/08/D3O-Formable-Foams.pdf.

[61] James David Hogan, Lukasz Farbaniec, Nitin Daphalapurkar, and KT Ramesh. On compressive brittle fragmentation. *Journal of the American Ceramic Society*, 99(6):2159–2169, 2016.

[62] Herbert Kolsky. An investigation of the mechanical properties of materials at very high rates of loading. *Proceedings of the physical society. Section B*, 62(11):676, 1949.

[63] Jiagui Liu, Dominique Saletti, Stephane Pattofatto, and Han Zhao. Impact testing of polymeric foam using hopkinson bars and digital image analysis. *Polymer testing*, 36:101–109, 2014.

[64] Qunli Liu and Ghatu Subhash. Characterization of viscoelastic properties of polymer bar using iterative deconvolution in the time domain. *Mechanics of Materials*, 38(12):1105–1117, 2006.

[65] I Irausquín, JL Pérez-Castellanos, V Miranda, and F Teixeira-Dias. Evaluation of the effect of the strain rate on the compressive response of a closed-cell aluminium foam using the split hopkinson pressure bar test. *Materials & Design*, 47:698–705, 2013.

[66] Weinong W Chen and Bo Song. *Split Hopkinson (Kolsky) bar: design, testing and applications*. Springer Science & Business Media, 2010.

[67] Bo Song and Weinong Chen. Split hopkinson pressure bar techniques for characterizing soft materials. *Latin American Journal of Solids and Structures*, 2(2): 113–152, 2005.

[68] Brett Sanborn and Bo Song. Poisson's ratio of a hyperelastic foam under quasi-static and dynamic loading. *International Journal of Impact Engineering*, 123: 48–55, 2019.

[69] Morgan and d3o create world's most advanced helmet for defence sector. URL `http://www.morganadvancedmaterials.com/en-gb/graduate-hub/morgan-news/morgan-and-d3o-create-world-s-most-advanced-helmet-for-defence-sector/`.

[70] W Chen, F Lu, and N Winfree. High-strain-rate compressive behavior of a rigid polyurethane foam with various densities. *Experimental Mechanics*, 42(1):65–73, 2002.

[71] Brian M Patterson, Nikolaus L Cordes, Kevin Henderson, Jason J Williams, Tyler Stannard, Sudhanshu S Singh, Angel Rodriguez Ovejero, Xianghui Xiao, Mathew Robinson, and Nikhilesh Chawla. In situ x-ray synchrotron tomographic imaging during the compression of hyper-elastic polymeric materials. *Journal of materials science*, 51(1):171–187, 2016.

[72] Ravi Sastri Ayyagari and Murat Vural. Multiaxial yield surface of transversely isotropic foams: Part I—Modeling. *Journal of the Mechanics and Physics of Solids*, 74(2015):49–67, jan 2015. ISSN 00225096. doi: 10.1016/j.jmps.2014.10.005.

[73] Ruoxuan Huang, Peifeng Li, and Tong Liu. X-ray microtomography and finite element modelling of compressive failure mechanism in cenosphere epoxy syntactic foams. *Composite Structures*, 140:157–165, 2016.

[74] Muhammad Shafiq, Ravi Sastri Ayyagari, Mohammad Ehaab, and Murat Vural. Multiaxial yield surface of transversely isotropic foams: Part II - Experimental. *Journal of the Mechanics and Physics of Solids*, 76(2015):224–236, 2015. ISSN 00225096. doi: 10.1016/j.jmps.2014.10.009.

[75] S. Youssef, E. Maire, and R. Gaertner. Finite element modelling of the actual structure of cellular materials determined by X-ray tomography. *Acta Materialia*, 53(3):719–730, 2005. ISSN 13596454. doi: 10.1016/j.actamat.2004.10.024.

[76] Rajendra P. Chhabra. Non-Newtonian fluids: An introduction. *Rheology of Complex Fluids*, pages 3–34, 2010. ISSN 1061933X. doi: 10.1007/978-1-4419-6494-6_1.

[77] Ali Can Kaya, Paul Zaslansky, Anneke Nikolaus, and Claudia Fleck. Tensile failure observations in sintered steel foam struts revealed by sub-micron contrast-enhanced microtomography. *Materials and Design*, 105:190–200, 2016. ISSN 18734197. doi: 10.1016/j.matdes.2016.05.069. URL `http://dx.doi.org/10.1016/j.matdes.2016.05.069`.

[78] Abdelmajid Elmoutaouakkil, Luc Salvo, Eric Maire, and Gilles Peix. 2d and 3d characterization of metal foams using x-ray tomography. *Advanced Engineering Materials*, 4(10):803–807, 2002.

[79] S. Tammas-Williams, H. Zhao, F. Léonard, F. Derguti, I. Todd, and P. B. Prangnell. XCT analysis of the influence of melt strategies on defect population in Ti-6Al-4V components manufactured by Selective Electron Beam Melting. *Materials Characterization*, 102:47–61, 2015. ISSN 10445803. doi: 10.1016/j.matchar.2015.02.008. URL `http://dx.doi.org/10.1016/j.matchar.2015.02.008`.

[80] O. Jiroušek, T. Doktor, D. Kytýř, P. Zlámal, T. Fíla, P. Koudelka, I. Jandejsek, and D. Vavřík. X-ray and finite element analysis of deformation response of closed-cell metal foam subjected to compressive loading. *Journal of Instrumentation*, 8 (2), 2013. ISSN 17480221. doi: 10.1088/1748-0221/8/02/C02012.

[81] Nina Carolin Fahlbusch, Joachim L. Grenestedt, and Wilfried Becker. Effective failure behavior of an analytical and a numerical model for closed-cell foams. *International Journal of Solids and Structures*, 97_98:417–430, 2016. ISSN 00207683. doi: 10.1016/j.ijsolstr.2016.07.007.

[82] Brian M Patterson, Kimberly A DeFriend Obrey, Christopher E Hamilton, and George J Havrilla. Three-dimensional density measurements of ultra low density materials by x-ray scatter using confocal micro x-ray fluorescence spectroscopy. *X-Ray Spectrometry*, 41(4):253–258, 2012.

[83] A Elmoutaouakkil, G Fuchs, P Bergounhon, R Peres, and aF Peyrin. Three-dimensional quantitative analysis of polymer foams from synchrotron radiation x-ray microtomography. *Journal of physics D: applied physics*, 36(10A):A37, 2003.

[84] DVWM De Vries. Characterization of polymeric foams. *Eindhoven University of Technology*, 2009.

[85] S. Zhang, J. M. Dulieu-Barton, R. K. Fruehmann, and O. T. Thomsen. A Methodology for Obtaining Material Properties of Polymeric Foam at Elevated Temperatures. *Experimental Mechanics*, 52(1):3–15, 2012. ISSN 00144851. doi: 10.1007/s11340-011-9519-7.

[86] Deborah A Williams and Roberto A Lopez-Anido. Strain rate and temperature effects of polymer foam core material. *Journal of Sandwich Structures & Materials*, 16(1):66–87, 2014. ISSN 1099-6362. doi: 10.1177/1099636213505582. URL `http://journals.sagepub.com/doi/10.1177/1099636213505582`.

[87] S. Zhang, J. M. Dulieu-Barton, and O. T. Thomsen. The effect of temperature on the failure modes of polymer foam cored sandwich structures. *Composite Structures*, 121:104–113, 2015. ISSN 02638223. doi: 10.1016/j.compstruct.2014.10.032.

[88] André Chrysochoos. Infrared thermography applied to the analysis of material behavior: A brief overview. *Quantitative InfraRed Thermography Journal*, 9(2):

193–208, 2012. ISSN 21167176. doi: 10.1080/17686733.2012.746069. URL http://www.tandfonline.com/doi/abs/10.1080/17686733.2012.746069.

[89] Yoshifumi Ohbuchi, Hidetoshi Sakamoto, and Nobuaki Nagatomo. Thermal image analysis of plastic deformation and fracture behavior by a thermo-video measurement system. *Measurement Science and Technology*, 27(12), 2016. ISSN 13616501. doi: 10.1088/0957-0233/27/12/124015.

[90] Defence, . URL https://www.d3o.com/defence/.

[91] D. Morin, G. Haugou, F. Lauro, B. Bennani, and B. Bourel. Elasto-viscoplasticity behaviour of a structural adhesive under compression loadings at low, moderate and high strain rates. *Journal of Dynamic Behavior of Materials*, 1(2):124–135, Jun 2015. ISSN 2199-7454. doi: 10.1007/s40870-015-0010-x.

[92] ASTM ASTM D3575-14. Standard test methods for flexible cellular materials made from olefin polymers. Technical report, ASTM, 2014.

[93] Flir x6901sc mwir. URL https://www.flir.ca/support-center/Instruments/service/infrared-camera-calibration/.

[94] Waldemar Minkina and Sebastian Dudzik. *Infrared thermography: errors and uncertainties*. John Wiley & Sons, 2009.

[95] Tomasz W. Wysokinski, Dean Chapman, Gregg Adams, Michel Renier, Pekka Suortti, and William Thomlinson. Beamlines of the biomedical imaging and therapy facility at the Canadian light source - Part 3. *Nuclear Instruments and Methods in Physics Research, Section A: Accelerators, Spectrometers, Detectors and Associated Equipment*, 775:1–4, 2015. ISSN 01689002. doi: 10.1016/j.nima.2014.11.088.

[96] Tech info technology overview. URL hhttps://bmit.lightsource.ca/tech-info/technology-overview/.

[97] The lasa® ac914 ballistic helmet | morgan composites and defence systems. URL http://www.morgandefencesystems.com/en-gb/advanced-armour/lasa-soldier-protection/lasa-ballistic-helmets/lasa-ac914-ballistic-helmet/.

[98] Ivan Jandrlić, Stoja Rešković, Franc Vodopivec, and Pascal Lava. Dependence of thermoelastic effect on volume change by elastic deformation. *Metals and materials international*, 22(3):407–412, 2016.

[99] Marco Rossi, Marco Sasso, Nathanael Connesson, Raman Singh, Adrian DeWald, David Backman, and Paul Gloeckner. *Residual Stress, Thermomechanics & Infrared Imaging, Hybrid Techniques and Inverse Problems..., Volume 8*. Springer, 2016.

[100] Luca Andena, Francesco Caimmi, Lidia Leonardi, Michele Nacucchi, and Fabio De Pascalis. Compression of polystyrene and polypropylene foams for energy absorption applications: a combined mechanical and microstructural study. *Journal of Cellular Plastics*, 55(1):49–72, 2019.

[101] U Jarfelt and O Ramnäs. Thermal conductivity of polyurethane foam - best performance Thermal conductivity of polyurethane foam Best performance. *10th International Symposium on District Heating and Cooling*, (September):12, 2006.

[102] Matthew D Montminy, Allen R Tannenbaum, and Christopher W Macosko. The 3d structure of real polymer foams. *Journal of colloid and interface science*, 280 (1):202–211, 2004.

[103] Guangfa Gao, Minju Qi, and Yongchi Li. Random equilateral kelvin open-cell foam microstructures: Cross-section shapes, compressive behavior, and isotropic characteristics. *Journal of Cellular Plastics*, 54(1):53–72, 2018.

[104] Liang Cui, Stephen Kiernan, and Michael D. Gilchrist. Designing the energy absorption capacity of functionally graded foam materials. *Materials Science and Engineering A*, 507(1-2):215–225, 2009. ISSN 09215093. doi: 10.1016/j.msea.2008.12.011.

[105] T. a. Schaedler, a. J. Jacobsen, A. Torrents, a. E. Sorensen, J. Lian, J. R. Greer, L. Valdevit, and W. B. Carter. Supplementary-Ultralight Metallic Microlattices. *Science*, 334(6058):962–965, 2011. ISSN 0036-8075. doi: 10.1126/science.1211649.

[106] Isaac M. Daniel, Jeong Min Cho, and Brian T. Werner. Characterization and modeling of stain-rate-dependent behavior of polymeric foams. *Composites Part A: Applied Science and Manufacturing*, 45:70–78, 2013. ISSN 1359835X. doi: 10.1016/j.compositesa.2012.10.003. URL `http://dx.doi.org/10.1016/j.compositesa.2012.10.003`.

[107] J. Andersons, U. Cābulis, L. Stiebra, M. Kirpļuks, and E. Spārniņš. Modeling the mode I fracture toughness of anisotropic low-density rigid PUR and PIR foams. *International Journal of Fracture*, 205(1):111–118, 2017. ISSN 15732673. doi: 10.1007/s10704-017-0194-2.

[108] Qunli Liu and Ghatu Subhash. A phenomenological constitutive model for foams under large deformations. *Polymer Engineering and Science*, 44(3):463–473, 2004. ISSN 00323888. doi: 10.1002/pen.20041.

[109] E. Linul, L. Marsavina, T. Voiconi, and T. Sadowski. Study of factors influencing the mechanical properties of polyurethane foams under dynamic compression. *Journal of Physics: Conference Series*, 451(1), 2013. ISSN 17426596. doi: 10.1088/1742-6596/451/1/012002.

[110] Emanoil Linul, Dan Andrei Şerban, Liviu Marsavina, and Tomasz Sadowski. Assessment of collapse diagrams of rigid polyurethane foams under dynamic loading conditions. *Archives of Civil and Mechanical Engineering*, 17(3):457–466, 2017. ISSN 16449665. doi: 10.1016/j.acme.2016.12.009.

[111] Liviu Marsavina, Emanoil Linul, Tudor Voiconi, and Tomasz Sadowski. A comparison between dynamic and static fracture toughness of polyurethane foams. *Polymer Testing*, 32(4):673–680, jun 2013. ISSN 01429418. doi: 10.1016/j.polymertesting.2013.03.013. URL `http://dx.doi.org/10.1016/j.polymertesting.2013.03.013https://linkinghub.elsevier.com/retrieve/pii/S0142941813000536`.

[112] J. Andersons, M. Kirpluks, L. Stiebra, and U. Cabulis. Anisotropy of the stiffness and strength of rigid low-density closed-cell polyisocyanurate foams. *Materials and Design*, 92:836–845, 2016. ISSN 18734197. doi: 10.1016/j.matdes.2015.12.122.

[113] S. Koumlis and L. Lamberson. Strain Rate Dependent Compressive Response of Open Cell Polyurethane Foam. *Experimental Mechanics*, may 2019. ISSN 0014-4851. doi: 10.1007/s11340-019-00521-3. URL `http://link.springer.com/10.1007/s11340-019-00521-3`.

[114] Standard Test Methods. Standard Test Methods for Flexible Cellular Materials — Slab , Bonded , and Molded Urethane Foams. *Astm*, Designatio(January):1–29, 2012. doi: 10.1520/D3574-11.2.

[115] Poron XRD - extreme impact protection, 2009. URL `http://www.poroncomfort.com/documents/2826/XRD-Standard-Physical-Properties.aspx`.

[116] ASTM D 624-00. Standard Test Method for Tear Strength of Conventional Vulcanized Rubber and. *Annual Book of ASTM Standards*, 00(Reapproved):1–9, 2012. doi: 10.1520/D0624-00R20.2.

[117] Calvin Lo, Tomoko Sano, and James D. Hogan. Deformation mechanisms and evolution of mechanical properties in damaged advanced ceramics. *Journal of the European Ceramic Society*, 40(8):3129–3139,

jul 2020. ISSN 09552219. doi: 10.1016/j.jeurceramsoc.2020.02.058. URL https://doi.org/10.1016/j.jeurceramsoc.2020.02.058https://linkinghub.elsevier.com/retrieve/pii/S0955221920301667.

[118] James David Hogan, Lukasz Farbaniec, Debjoy Mallick, Vladislav Domnich, Kanak Kuwelkar, Tomoko Sano, James W. McCauley, and Kaliat T. Ramesh. Fragmentation of an advanced ceramic under ballistic impact: Mechanisms and microstructure. *International Journal of Impact Engineering*, 102:47–54, 2017. ISSN 0734743X. doi: 10.1016/j.ijimpeng.2016.12.008. URL http://dx.doi.org/10.1016/j.ijimpeng.2016.12.008.

[119] Tom Proulx. *Dynamic Behavior of Materials, Volume 1*. Conference Proceedings of the Society for Experimental Mechanics Series. Springer New York, New York, NY, 2011. ISBN 978-1-4419-8227-8. doi: 10.1007/978-1-4419-8228-5. URL http://link.springer.com/10.1007/978-1-4419-8228-5.

[120] X. J. Wu and D. A. Gorham. Stress Equilibrium in the Split Hopkinson Pressure Bar Test. *Le Journal de Physique IV*, 07(C3):C3–91–C3–96, 1997. ISSN 1155-4339. doi: 10.1051/jp4:1997318.

[121] Weinong W. Chen and Bo Song. *Split Hopkinson (Kolsky) Bar*.

[122] Bo Song, Brett Sanborn, and Wei Yang Lu. Radial inertia effect on dynamic compressive response of polymeric foam materials. *Conference Proceedings of the Society for Experimental Mechanics Series*, pages 85–87, 2019. ISSN 21915652. doi: 10.1007/978-3-319-95089-1_13.

[123] George T Rusty, Gray Iii, and William R Blumenthal. Split-Hopkinson Pressure Bar Testing of Soft Materials. *Mechanical Testing and Evaluation*, 8:488–496, 2018. doi: 10.31399/asm.hb.v08.a0003298.

[124] Vic-2d, correlated solutions inc, irmo, south carolina, vic-2d. URL https://www.correlatedsolutions.com/vic-2d/.

[125] Hubert Schreier Michael A. Sutton, Jean Jose Orteu. *Image Correlation for Shape, Motion and Deformation Measurements*. Springer US, New York, NY, 2009. doi: 10.1007/978-0-387-78747-3. URL https://www.springer.com/gp/book/9780387787466.

[126] M.A. Sutton, J.H. Yan, V. Tiwari, H.W. Schreier, and J.J. Orteu. The effect of out-of-plane motion on 2d and 3d digital image correlation measurements. *Optics and Lasers in Engineering*, 46(10):746 – 757, 2008. ISSN 0143-8166. doi: https://doi.org/10.1016/j.optlaseng.2008.05.005. URL http://www.sciencedirect.com/science/article/pii/S0143816608000985.

[127] Aad W Van der Vaart. *Asymptotic statistics*, volume 3. Cambridge university press, 2000.

[128] Yongle Sun and Q. M. Li. Dynamic compressive behaviour of cellular materials: A review of phenomenon, mechanism and modelling. *International Journal of Impact Engineering*, 112(October 2017):74–115, 2018. ISSN 0734743X. doi: 10.1016/j.ijimpeng.2017.10.006.

[129] Bo Song, Weinong Chen, and Danny J. Frew. Dynamic compressive response and failure behavior of an epoxy syntactic foam. *Journal of Composite Materials*, 38 (11):915–936, jun 2004. ISSN 00219983. doi: 10.1177/0021998304040552. URL `http://journals.sagepub.com/doi/10.1177/0021998304040552`.

[130] N. J. Mills and H. X. Zhu. The high strain compression of closed-cell polymer foams. *Journal of the Mechanics and Physics of Solids*, 47(3):669–695, 1999. ISSN 00225096. doi: 10.1016/S0022-5096(98)00007-6. URL `http://linkinghub.elsevier.com/retrieve/pii/S0022509698000076`.

[131] Mohammad S. Gholami, Olivier Doutres, and Noureddine Atalla. Effect of microstructure closed-pore content on the mechanical properties of flexible polyurethane foam. *International Journal of Solids and Structures*, 112:97–105, 2017. ISSN 00207683. doi: 10.1016/j.ijsolstr.2017.02.016. URL `http://dx.doi.org/10.1016/j.ijsolstr.2017.02.016`.

[132] K. C. Rusch. Load–compression behavior of flexible foams. *Journal of Applied Polymer Science*, 13(11):2297–2311, 1969. ISSN 10974628. doi: 10.1002/app.1969.070131106.

[133] Miao Tang, Gang Huang, Huanhuan Zhang, Yuling Liu, Haijian Chang, Hongzan Song, Donghua Xu, and Zhigang Wang. Dependences of Rheological and Compression Mechanical Properties on Cellular Structures for Impact-Protective Materials. *ACS Omega*, 2(5):2214–2223, 2017. ISSN 24701343. doi: 10.1021/acsomega.7b00242.

[134] Denis Weaire, Steven T. Tobin, Aaron J. Meagher, and Stefan Hutzler. Foam Morphology. *Foam Engineering: Fundamentals and Applications*, pages 5–26, 2012. doi: 10.1002/9781119954620.ch2.

[135] H. Niknam and A. H. Akbarzadeh. Thermo-mechanical bending of architected functionally graded cellular beams. *Composites Part B: Engineering*, 174(February): 107060, 2019. ISSN 13598368. doi: 10.1016/j.compositesb.2019.107060. URL `https://doi.org/10.1016/j.compositesb.2019.107060`.

[136] Alireza Bagher Shemirani, R. Naghdabadi, and M. J. Ashrafi. Experimental and numerical study on choosing proper pulse shapers for testing concrete specimens by split Hopkinson pressure bar apparatus. *Construction and Building Materials*, 125:326–336, 2016. ISSN 09500618. doi: 10.1016/j.conbuildmat.2016.08.045. URL `http://dx.doi.org/10.1016/j.conbuildmat.2016.08.045`.

[137] M. Eynbeygui, J. Arghavani, A. H. Akbarzadeh, and R. Naghdabadi. Anisotropic elastic-plastic behavior of architected pyramidal lattice materials. *Acta Materialia*, 183:118–136, 2020. ISSN 13596454. doi: 10.1016/j.actamat.2019.10.038. URL `https://doi.org/10.1016/j.actamat.2019.10.038`.

[138] S. Deschanel, L. Vanel, N. Godin, E. Maire, G. Vigier, and S. Ciliberto. Mechanical response and fracture dynamics of polymeric foams. *Journal of Physics D: Applied Physics*, 42(21), 2009. ISSN 00223727. doi: 10.1088/0022-3727/42/21/214001.

[139] O. E. Petel, S. Ouellet, A. J. Higgins, and D. L. Frost. The elastic-plastic behaviour of foam under shock loading. *Shock Waves*, 23(1):55–67, 2013. ISSN 09381287. doi: 10.1007/s00193-012-0414-7.

[140] Vitaly A. Kuzkin. Structural model for the dynamic buckling of a column under constant rate compression. pages 1–8, 2015. URL `http://arxiv.org/abs/1506.00427`.

[141] J. Kimberley, K. T. Ramesh, and N. P. Daphalapurkar. A scaling law for the dynamic strength of brittle solids. *Acta Materialia*, 61(9):3509–3521, 2013. ISSN 13596454. doi: 10.1016/j.actamat.2013.02.045. URL `http://dx.doi.org/10.1016/j.actamat.2013.02.045`.

[142] Ruoxuan Huang, Peifeng Li, and Tong Liu. X-ray microtomography and finite element modelling of compressive failure mechanism in cenosphere epoxy syntactic foams. *Composite Structures*, 140:157–165, 2016. ISSN 02638223. doi: 10.1016/j.compstruct.2015.12.040. URL `http://dx.doi.org/10.1016/j.compstruct.2015.12.040`.

[143] Jun Zhang, Noboru Kikuchi, Victor Li, Albert Yee, and Guy Nusholtz. Constitutive modeling of polymeric foam material subjected to dynamic crash loading. *International Journal of Impact Engineering*, 21(5):369–386, 1998. ISSN 0734743X. doi: 10.1016/S0734-743X(97)00087-0. URL `http://linkinghub.elsevier.com/retrieve/pii/S0734743X97000870`.

[144] V. S. Deshpande and N. A. Fleck. Multi-axial yield behaviour of polymer foams. *Acta Materialia*, 49(10):1859–1866, 2001. ISSN 13596454. doi: 10.1016/S1359-6454(01)00058-1.

[145] Jianxun Zhang, Qinghua Qin, Xiaohuan Han, and Weilong Ai. The initial plastic failure of fully clamped geometrical asymmetric metal foam core sandwich beams. *Composites Part B: Engineering*, 87:233–244, 2016. ISSN 13598368. doi: 10.1016/j.compositesb.2015.10.027. URL `http://dx.doi.org/10.1016/j.compositesb.2015.10.027`.

[146] Andrew M Kraynik, Michael K Neilsen, Douglas A. Reinelt, and William E Warren. Foam micromechanics, 1997.

[147] P Viot and A Mercier. Behaviour of Polymeric Multiscale Foam Under Dynamic Loading -Study of the Influence of the Density and the Walls of Beads. 7(April): 1–19, 2011.

[148] Brett Sanborn and Bo Song. Poisson's ratio of a hyperelastic foam under quasi-static and dynamic loading. *International Journal of Impact Engineering*, 123 (May 2018):48–55, 2019. ISSN 0734743X. doi: 10.1016/j.ijimpeng.2018.06.001. URL `https://doi.org/10.1016/j.ijimpeng.2018.06.001`.

[149] James A. Sherwood and Colin C. Frost. Constitutive modeling and simulation of energy absorbing polyurethane foam under impact loading. *Polymer Engineering & Science*, 32(16):1138–1146, 1992. ISSN 15482634. doi: 10.1002/pen.760321611.

[150] D. Niedziela, I. E. Ireka, and K. Steiner. Computational Analysis of Nonuniform Expansion in Polyurethane Foams. *Polymers*, 11(1):100, 2019. doi: 10.3390/polym11010100.

[151] I. Carranza, A. D. Crocombe, I. Mohagheghian, P. A. Smith, A. Sordon, G. Meeks, and C. Santoni. Characterising and modelling the mechanical behaviour of polymeric foams under complex loading. *Journal of Materials Science*, 54(16): 11328–11344, 2019. ISSN 15734803. doi: 10.1007/s10853-019-03673-8. URL `https://doi.org/10.1007/s10853-019-03673-8`.

[152] K.B. Bhagavathula, J.S. Parcon, A. Azar, S. Ouellet, S. Satapathy, C.R. Dennison, and J.D. Hogan. Quasistatic response of a shear-thickening foam: Microstructure evolution and infrared thermography. *Journal of Cellular Plastics*, 2020. ISSN 15307999. doi: 10.1177/0021955X20963989.

[153] ASTM D 624-00. Standard Test Method for Tear Strength of Conventional Vulcanized Rubber and. *Annual Book of ASTM Standards*, 00(Reapproved):1–9, 2012. doi: 10.1520/D0624-00R20.2.

[154] KB Bhagavathula, C Meredith, S Satapathy, S Ouellet, D Romanyk, , and JD Hogan. Density, microstructure and strain-rate effects on the compressive response of polyurethane foams. *Experimental Mechanics*, 2021.

[155] B Erickson, K Mimura, T Kikui, N Nishide, T Umeda, I Riku, and H Hashimoto. Buckling behavior of clamped and intermediately-supported long rods in the static–dynamic transition velocity region. *J. Soc. Mater. Sci.*, 61(11):881–887, 2012.

[156] Jeong-Ho Lee, Dong-Man Ryu, and Chi-Seung Lee. Constitutive-damage modeling and computational implementation for simulation of elasto-viscoplastic-damage behavior of polymeric foams over a wide range of strain rates and temperatures. *International Journal of Plasticity*, 130(February):102712, jul 2020. ISSN 07496419. doi: 10.1016/j.ijplas.2020.102712. URL `https://doi.org/10.1016/j.ijplas.2020.102712https://linkinghub.elsevier.com/retrieve/pii/S0749641919305418`.

[157] Yongle Sun, B. Amirrasouli, S. B. Razavi, Q. M. Li, T. Lowe, and P. J. Withers. The variation in elastic modulus throughout the compression of foam materials. *Acta Materialia*, 110:161–174, 2016. ISSN 13596454. doi: 10.1016/j.actamat.2016.03.003.

[158] Behrad Koohbor, Suraj Ravindran, and Addis Kidane. Effects of cell-wall instability and local failure on the response of closed-cell polymeric foams subjected to dynamic loading. *Mechanics of Materials*, 116:67–76, 2018. ISSN 01676636. doi: 10.1016/j.mechmat.2017.03.017.

[159] EA Flores-Johnson, QM Li, and RAW Mines. Degradation of elastic modulus of progressively crushable foams in uniaxial compression. *Journal of cellular plastics*, 44(5):415–434, 2008.

[160] Elhem Ghorbel. A viscoplastic constitutive model for polymeric materials. *International Journal of Plasticity*, 24(11):2032–2058, 2008. ISSN 07496419. doi: 10.1016/j.ijplas.2008.01.003.

[161] Ir spectrum table chart. URL `https://www.sigmaaldrich.com/CA/en/technical-documents/technical-article/analytical-chemistry/photometry-and-reflectometry/ir-spectrum-table`.

[162] Philip A Lockhart and Duane S Cronin. Helmet liner evaluation to mitigate head response from primary blast exposure. *Computer methods in biomechanics and biomedical engineering*, 18(6):635–645, 2015.

[163] Ge He, Yucheng Liu, Xingqiao Deng, and Lei Fan. Constitutive modeling of viscoelastic–viscoplastic behavior of short fiber reinforced polymers coupled with anisotropic damage and moisture effects. *Acta Mechanica Sinica/Lixue Xuebao*, (November), 2018. ISSN 16143116. doi: 10.1007/s10409-018-0810-z.

[164] S. Nemat-Nasser, W. J. Kang, J. D. McGee, W. G. Guo, and J. B. Isaacs. Experimental investigation of energy-absorption characteristics of components of sandwich structures. *International Journal of Impact Engineering*, 34(6):1119–1146, 2007. ISSN 0734743X. doi: 10.1016/j.ijimpeng.2006.05.007.

[165] M. Cheng W. Chen, F. Lu. Ension and Compression Tests of Two Polymers Under Quasi-Static and Dynamic Loading. *Polymer Testing*, 21:113–121, 2002.

[166] Bo Song, Kevin Nelson, Ronald Lipinski, John Bignell, G.B. Ulrich, and E.P. George. Dynamic high-temperature Kolsky tension bar techniques. *EPJ Web of Conferences*, 94:01066, 2015. ISSN 2100-014X. doi: 10.1051/epjconf/20159401066. URL `http://www.epj-conferences.org/10.1051/epjconf/20159401066`.

[167] I.G. Crouch and B. Eu. *Ballistic testing methodologies*. 2017. ISBN 9780081007044. doi: 10.1016/B978-0-08-100704-4.00011-6. URL `http://linkinghub.elsevier.com/retrieve/pii/B9780081007044000116`.

[168] Ronald E. Miller. Continuum plasticity model for the constitutive and indentation behaviour of foamed metals. *International Journal of Mechanical Sciences*, 42(4): 729–754, 2000. ISSN 00207403. doi: 10.1016/S0020-7403(99)00021-1.